Molecular Precursors for Graphene Formation Investigated by Scanning Tunneling Microscopy

A Dissertation

Submitted in Partial Fulfilment of the
Requirements for the Degree of Ph.D.

to the Department of Physics
of Freie Universität Berlin

by
Bo Chen

Berlin, 2017

Supervisor : Prof. Dr. Katharina J. Franke
Second examiner: Prof. Dr. Petra Tegeder

Date of defense: 06.11.2017

Kurzfassung

Kürzlich konnte gezeigt werden, dass Graphen und Graphen-Nanobänder (GNR) aus einer Vielzahl von molekularen Präkursoren unter Ultra-Hochvakuum-Bedingungen auf Metalloberflächen gewachsen werden können. Im Besonderen wurden aus 10,10'-Dibromo-9,9'-Bianthryl (DBBA)- und 1,1-Ferrocendicarboxyl-Säure (FcAd)-Molekülen GNR und dreieckige Graphen-Inseln durch genügend hohes Heizen auf Edelmetalloberflächen hergestellt. Das Ziel dieser Arbeit war es ein vollständiges Bild der Adsorptionseigenschaften von Präkursoren und Reaktionsprodukten zu erhalten. Wir benutzten Rastertunnelmikroskopie und –spektroskopie um die Strukturen und elektronischen Eigenschaften der Edukte und Produkte zu untersuchen.
Die Deposition von DBBA-Molekülen auf Au(111) bei Raumtemperatur resultiert in geordneten molekularen Inseln. Die Selbstassemblierung der Strukturen wird durch Wasserstoffbrückenbindungen und π-π Wechselwirkungen bestimmt. Weiterhin haben wir die Präkursor-Strukturen auf verschiedene Temperaturen von 100 °C bis 400 °C geheizt. Mit steigender Temperatur vollführen die DBBA-Moleküle eine strukturelle Neuanordnung auf der Oberfläche, bevor Dehalogenierung und anschließend Ullmann-Kopplung einsetzen. Schließlich formen sich GNR, die sich durch an den beiden Enden lokalisierten Tamm-Zuständen identifizieren lassen. Um temperaturinduzierte Reaktionen mit photoneninduzierten Prozessen zu vergleichen, haben wir die Probe mit Laserstrahlung beleuchtet. Dies führt zur Aufspaltung von C-C-Bindungen innerhalb der Anthracen-Einheiten und schließlich zu Tetradecan-Molekülen.
Wir haben außerdem die Struktur und elektronischen Eigenschaften von FcAd-Molekülen auf Ag(111) und Cu(111) untersucht. Auf Ag(111) konnten wir zwei Adsorptions-Konfigurationen, vertikal bzw. horizontal, der FcAd-Moleküle identifizieren. Die horizontalen FcAd-Moleküle führen zur Bindung zweier benachbarter FcAd-Dimere. Auf Cu(111) formen die FcAd-Moleküle auch molekulare Inseln, wobei aber nur die horizontale Adsorptionskonfiguration gefunden wurde. Die lokale Adsorptionskonfiguration innerhalb der Molekülinseln konnte durch Bias-Spannungspulse geändert werden. Das Heizen der FcAd/Cu(111) Probe führte zu dreieckigen Graphen-Inseln auf Cu(111). Durch die hohe Menge von thermisch induzierten, ungeordneten Nebenprodukten wurde das weitere Wachstum von Graphen-Inseln behindert. Wir schlagen vor, dass die Bildung von Graphen-Inseln den Prozess der Ringöffnung des 5-Kolenstoff-Rings und Neubinden zum 6. Kohlenstoffatom unter Verwendung des Kohlenstoffatoms aus der COOH-Gruppe derselben Cyclopentancarboxyl-Einheit beinhaltet. Ähnliche Experimente wurden auf Ag(111) mit Heizen der FcAd/Ag(111)-Probe durchgeführt. Allerdings wurden hier keine Graphen-Inseln beobachtet, was vermutlich an der geringeren katalytischen Aktivität gegenüber dem Cu(111)-Substrat liegt.
Während Ethylen durch Dekomposition auf reaktiven Oberflächen bekanntermaßen zu defektfreien Graphen-Lagen zusammenwächst, ist die auf Edelmetalloberflächen schwieriger. Wir haben einen Hochtemperatur-Ofen zum Heizen von Au(111)-Oberflächen mit der Möglichkeit gleichzeitigen sputterns der Oberfläche mit Ethylen-Gas in Betrieb genommen. Wir finden Kohlenstoff-Inseln auf der Au(111)-Oberfläche, wenn die Probe während des Ethylen-bombardements auf 790 °C gehalten wird.
Schließlich haben wir die Selbstassemblierung von 4-Carboxy Benzylidenanilin (CBA)-Molekülen auf Au(111) untersucht. Die CBA-Moleküle formen Dimer-Reihen, welche durch Wasserstoffbrückenbindungen stabilisiert werden. Co-deposition von CBA-Molekülen und Kobalt-Atomen auf der Goldoberfläche resultiert in neuen metallorganischen Strukturen mit verschiedenen Bindungsmotiven, bei denen die Kobalt-Atome mit den Carboxyl-Gruppen koordinieren.

Abstract

Recently, it has been shown that graphene and graphene nanoribbons can be grown under ultra-high vacuum conditions by heating a large variety of molecular precursors on metal surfaces. In particular, 10,10'-Dibromo-9,9'-Bianthryl (DBBA) and 1,1-Ferrocenedicarboxylic acid (FcAd) molecules have previously been shown to yield graphene nanoribbons and triangular graphene flakes when heated to sufficiently high temperatures on noble metal surfaces. The goal of this thesis was to obtain a complete picture of the adsorption properties of the precursors as well as of the reaction products. We used scanning tunneling microscopy and spectroscopy to study the structures and electronic properties of educts and products.

Deposition of DBBA molecules on Au(111) at room temperature results in ordered molecular island. The self-assembly of the structures is driven by hydrogen bonding and π-π interactions. Due to the weak intermolecular bonding, individual DBBA molecules can be dragged out from the islands by the STM tip. We then heated the precusor structures to five different temperatures from 100 °C up to 400 °C. With increasing temperature, DBBA molecules undergo a structural rearrangement on the surface before dehalogenation followed by Ullmann coupling sets in. Finally graphene nanoribbons are formed with the identifiable Tamm state localized at the two terminals of the ribbons. To compare temperature-induced reactions with photon-induced processes, we illuminated the sample with a laser. This led to C-C bond cleavage within the anthracene units, and, eventually to tetradecane molecules.

We have also investigated the structural and electronic properties of FcAd molecules on Ag(111) and Cu(111). On the Ag(111), we identify two adsorption configurations of FcAd molecules, vertically and horizontally. The horizontal FcAd molecules mediate the binding of two adjacent FcAd dimers. On the Cu(111), FcAd molecules also form molecular island. However, only the horizontal adsorption configuration has been found. Applying bias voltage pulses could change the local adsorption configuration of FcAd molecule within the molecular island. Annealing the FcAd/Cu(111) sample led to small triangular graphene patches on Cu(111). Due to the large number of unordered thermally induced by-products, the growth of graphene islands was hindered. We propose that the formation of graphene patches involves the process of 5-carbon ring opening and re-bonding to the 6th carbon atom provided by a COOH group of the same cyclopentanecarboxylic moiety. Similar experiments have been performed on Ag(111) by annealing the FcAd/Ag(111) sample. However, the we did not observe graphene patches, probably due to the lower catalytic activity compared to the Cu(111) substrate.

While it is well-known that ethylene decomposition on reactive surfaces leads to defect-free graphene sheets, their production on noble metal surfaces is more difficult. We set up a heating station for high-temperature annealing of Au(111) surfaces with the possibility of simultaneously sputtering the surface with ethylene gas. We observe carbon islands on the Au(111) surface when the sample was kept at around 790 °C during the ethylene bombardment.

Finally, we investigated the self-assembly of 4-Carboxy Benzylideneaniline (CBA) molecules on Au(111). CBA molecules form dimer rows, stabilized by hydrogen bonds. Co-deposition of CBA molecules and cobalt atoms on the gold surface results in new metal-organic structures of different bonding motives, where the carboxylic groups coordinate with Co atoms.

Contents

Introduction

With the rapid development of modern technologies, electronic equipment becomes much smaller and works more efficiently. This is due to the big progress of minimization of the electronic devices, making the average individual yield larger and larger. However, behind the flourishing scenes, huge consumption of resources, especially the non-renewable ones, urge people to explore more environment-friendly and sustainable substitutions. Therefore, organic molecules and their derivatives are regarded as the substitution materials for producing new generation electronics.

Nowadays, it is notable that more and more functions, such as the switching behaviour, the transistor effect and so on, have been experimentally realized with the organic molecules in the nanoscale [1–3]. At the same time deep insight into the intermolecular and intramolecular interaction mechanisms have been widely investigated, such as van der Waals forces [4], hydrogen bonds [5] and covalent bonds [6, 7].

Among the countless organic structures, graphene, as an organic material with its unique electrical and structural properties, has been increasingly debated in the past decades. It arises many interests in the academic field as well as in the application field mainly because of its high carrier mobility at the room temperature. However, the semi-metal property of graphene hinders its development in transistors which needs high on-off ratios [8, 9]. Nevertheless, by modifying the structure of graphene, a tunable band gap can be realized [10]. Hence, people are keen to utilize different methods to fabricate various sizes of graphene to fulfill the requirement from the application field. Among them, the tunability of the band gap of graphene nanoribbons has already been reported [11]. An edge state of graphene nanoribbon has also been published for two decades [12]. Obviously, graphene with a defined size and edge can meet the higher requirement from the academic and industrial area. Nevertheless, there is some limitation of traditional top-down fabrication methods such as the lack of treatment on the edge structure [13]. Therefore, we choose to use the bottom-up approach to fabricate the sample through annealing the precursor molecules and inducing on-surface reactions. Heating the molecular building blocks with the bottom-up method has been successfully performed to obtain precise size and shape of graphene [14, 15]. However, the transition from the building blocks to the final graphene products is finitely discussed. The investigation on the precursor molecules is capable of guiding the direction of choosing the right organic molecules to more efficiently and purposefully fabricate graphene. Therefore, self-assembly of different precursor molecules on Au(111), Ag(111) and Cu(111) experiments have been conducted. The 10,10'-dibromo-9,9'-bianthryl (DBBA) molecules exhibit similar but distinct adsorption geometries inside the molecular island and singly on the Au(111) surface, respectively. The 1,1-ferrocenedicarboxylic acid (FcAd) molecules show completely different self-assembly configurations on Ag(111) and Cu(111), respectively.

Furthermore, the analysis on the thermal products derived from heating the precursor samples under different annealing temperatures could help to clarify the reaction process and mechanism. For the DBBA/Au(111) sample, on-surface polymerization process can be divided into three parts: Firstly, the DBBA building blocks form molecular clusters through halogen bonds under low-annealing temperature. Secondly, the dehalogenation process starts and radicals covalently bond to each other under the moderate annealing temperature, leading to the polymer chains on the gold surface. Finally, graphene nanoribbons

can be obtained through cyclodehydrogenation process under high annealing temperature. For the FcAd/Ag(111) and FcAd/Cu(111) experiments, in the former one, FcAd molecules exhibit two configurations in the self-assembly molecular island while in the latter one, FcAd molecules only show single adsorption behaviours with two orientations. After annealing the respective samples, triangular graphene patches can only be obtained from the FcAd/Cu(111).

Besides, if we want to realize the molecular electronics in the application field, it is insufficient to obtain the proper molecular structures. The metal electrodes for contacting the molecular structures are also needed to be considered. Therefore, the studies on the interaction between the molecules and metal electrodes is necessary. Coupling between the metal electrodes and organic structures can disturb the free molecule properties. The energy level alignment of the molecular orbitals modified by coordinating metal atoms have already been published in ref. [16]. Along this way, we also experimentally investigate the interaction between the 4-carboxy benzylideneaniline (CBA) molecules and cobalt atoms on Au(111).

Therefore, to investigate the structural and electrical properties of the precursor molecules for fabricating graphene, in this thesis, we study their structural and electronic behaviours in the level of molecule-molecule interaction as well as the molecule-metal interaction by using STM and AFM. STM system is capable of providing the high resolution images and high energy resolution spectra. AFM measurements could explore the intramolecular structures. The thesis is described in the following way:

In **chapter 1**, we introduce the details of the STM setup and the molecules used in this thesis. We also review the methods of graphene growth.

In **chapter 2**, we investigate the organic self-assemblies of DBBA molecules on the Au(111) surface. Structural properties of DBBA molecular islands and single DBBA molecule have also been discussed. Then, electronic properties of the molecular islands and single DBBA molecule are measured with STS. The interaction between the DBBA island and the gold substrate has been analyzed. Heating treatment experiments under different temperatures have been conducted and the thermal products have been introduced. The DBBA molecules on Au(111) experience a process including the formation of two phases through the halogen bonds under low annealing temperature, the dehalogenation and Ullmann reactions under moderate annealing temperature, and the formation of GNR under high temperature. Furthermore, we investigated the impact of laser illumination of the DBBA/Au(111). This lead to the formation of tetradecane molecular islands.

In **chapter 3**, we examine the adsorption and assembly of FcAd molecules on two more reactive metal surfaces, Ag(111) and Cu(111) respectively. Therefore, FcAd molecules exhibit different structural and electronic features on two substrates. It is also notable that triangular graphene patches can be obtained through annealing FcAd molecules on Cu(111), however, it cannot be observed by heating the FcAd/Ag(111) sample.

In **chapter 4**, we utilize the sputter gun to bombard the ethylene molecules upon the Au(111) while keeping the substrate at high temperature. Some organic islands have been observed growing from the step edges of Au(111), which can be ascribed to carbon-related structures.

In **chapter 5**, we study the adsorption behaviour of CBA molecules on Au(111). The metal-organic coordination has also been investigated on the sample of Co atoms and CBA molecules. Annealing condition has also been performed and some new features have been observed.

In **chapter 6**, we summarize the results presented in this thesis.

1 Theoretical Background and Experimental Approaches

In 1966, Russel Young proposed to characterize the conductive surface by measuring the weak current between a metal tip and a sample. Soon after that, in 1971, Russel and coworkers published their result, showing their new instrument is capable of measuring the high resolution topographic map of the surface. This measurement setup was named "Topografiner" [17]. The working mechanism of the topografiner is based on the tunneling effect, which leads to a current depending on the distance between the tip and the sample. Therefore, the topografiner can be regarded as the precursor and the prototype of scanning tunneling microscope (STM) [18, 19].

In 1982, the scanning tunneling microscope was invented by G.Binnig and H.Rohrer at IBM institute [20]. They investigated a Si(111)-7×7 surface in real space with atomic resolution [20]. Because of the tunneling principle in quantum physics, STM, for the first time, could help researchers to directly observe the atomic structures on surfaces. Additionally, scanning tunneling spectroscopy (STS) provides information about the electronic configurations of the surfaces and possible adsorbates.

The invention of STM can also be used to investigate molecular structures, surface defects, and chemical reactions on the atomic scale. The main advantage of STM, in contrast to other measuring techniques such as low energy electron diffraction (LEED) exhibiting average information over large sample area in reciprocal space, is that it does not rely on the diffraction and periodic structures, but measures the current in real space. Due to the significant influence and promising applications in surface science, material science as well as bioscience, the Noble Prize in Physics was given to Binnig adn Rohrer [21, 22].

However, STM has some limitations, such as the samples need to be conductive since the tunneling current is used as the imaging signal. In addition, the topographies taken from STM measurement contain the electronic structure of the sample, which makes the interpretation of STM images not that straightforward. In fact, the topographies are a convolution of the tip-sample spacing and the electronic structure of the sample. Therefore, based on the development of STM, a series of scanning probe setups were invented such as atomic force microscopy (AFM) [23], magnetic force microscopy (MFM), which are also widely used in the fields of surface science. These techniques greatly improve the capability of perceiving the nano-world.

In this chapter, we will explain the physical basics of STM and STS. Preparation of samples and tip will be also reported. At the end of this chapter, the experimental setups, substrates and molecules will be introduced.

1.1 Scanning Tunneling Microscopy

1.1.1 STM Working Principles

STM is based on the quantum mechanical tunneling effect. According to the description of quantum mechanics, particles display a wave-like nature. The wave function of the quantum mechanical particles penetrates into the potential barrier. The wave function decays exponentially in the barrier. In our case, the thickness of the barrier can be associated with the distance between the STM tip and the sample. If the barrier is sufficiently small,

there is a finite amplitude of the wave function at the other side of the barrier. This leads to a finite probability of the particle crossing the barrier. This process is named tunneling effect. Although the particles do not have enough energy to overcome the potential barrier, they still have the possibility to appear on the other side of the potential barrier.

The working principle of STM is based on the quantum mechanical tunneling effect. It means the distance between a STM tip and a sample surface z is limited to a few Angstroms (Å), in most cases less than 10 Å (Figure 1.1 a)). The STM tip and sample are two conductive electrodes. In a simplified view, the system can be seen as metal-vacuum-metal tunneling junction. The tunneling current I_t is dramatically sensitive to the variation of tip-sample distance z. 1 Å change of z results in one order of magnitude change in the tunneling current due to the exponential decay of the tunneling amplitude. Therefore, I_t shows an exponential dependence on the tip-sample distance z,

$$I_{\mathrm{t}} \propto \exp(-\mathrm{A}\varphi^{1/2}z) \tag{1.1.1}$$

where A is a constant, and φ is the average of the work function of tip and sample, which is φ=(φ_t+φ_s)/2. φ_t and φ_s are the work functions of the tip and sample, respectively.

Piezoelectric elements are utilized to control the lateral and vertical movement of the scanning tip. By applying a voltage to the electrodes of the piezos, the motion of the STM tip can be realized in-plane and out-of-plane in atomic scale.

In the STM measurement system, there are three important factors that highly influence the measurement result, which are the tip-sample distance z, the bias voltage of the tip with respect to the sample V, and the tunneling current between tip and sample I_t. By tuning the parameters, two working modes can be used for acquiring images: the constant-current mode and constant-height mode, depicted in Figure 1.1 b) and c), respectively.

In the constant-height mode, the tip is kept at a fixed height. Variations obtained in the tunneling current represent the surface image. In this mode, it is necessary to have a flat surface, otherwise the tip could easily crash into large impurities on the surface.

In the constant-current mode, a feedback loop is used to maintain a constant tunneling current I_t. The tip height as a function of lateral position results in a map of the surface topography.

1.1.2 Theory of Scanning Tunneling Microscopy

In 1983, J.Tersoff and D.R. Hamann proposed a model based on first-order perturbation theory to explain the working principle of STM [24, 25]. They treated the tip and the surface as a locally spherical tip in proximity to a flat surface. In the limit of low bias voltage and temperature, the tunneling current I_t between tip and sample can be written as [24]:

$$I_{\mathrm{t}} = \frac{2\pi}{\hbar}\mathrm{e}^2 V \sum_{\mu,\nu} |M_{\mu\nu}|^2 \delta(E_\nu - E_{\mathrm{F}})\delta(E_\mu - E_{\mathrm{F}}). \tag{1.1.2}$$

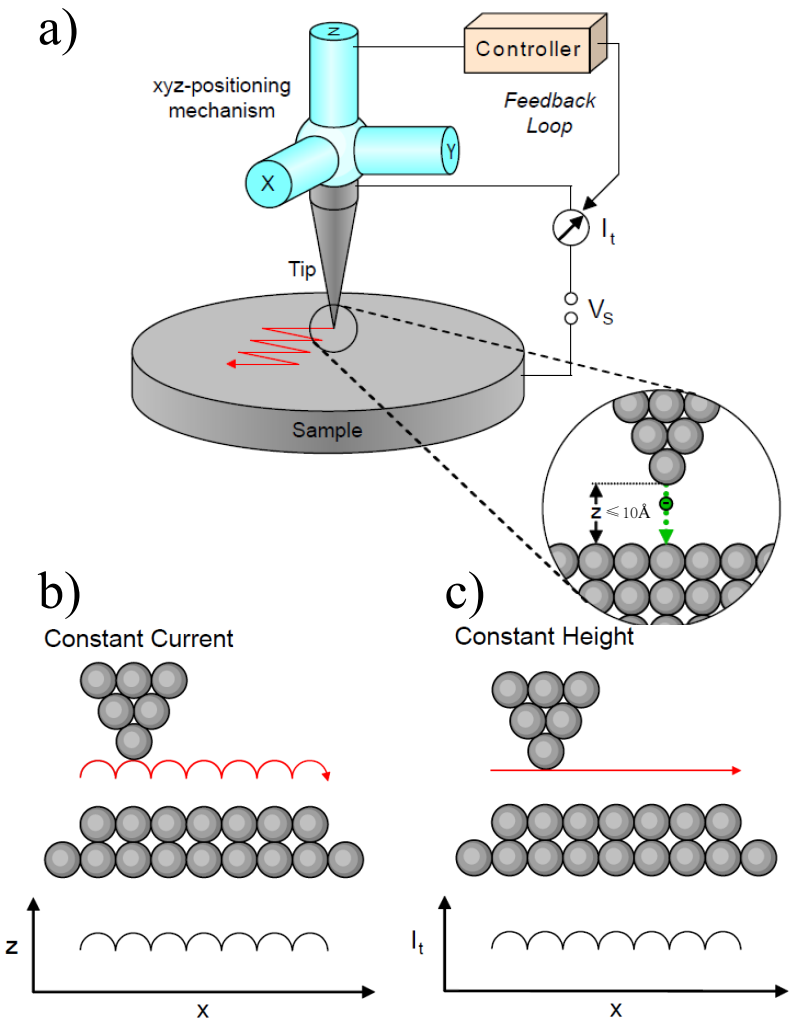

Figure 1.1: Different scanning modes of an STM. **a)** Scheme of the working principle of a STM. **b)** and **c)** Constant-current and constant-height scanning modes. The STM images are taken from the z or the I_t signal, respectively

here $\hbar$ is the reduced Planck constant (also named as Dirac constant), V is the applied bias voltage, E_ν is the energy of the electronic states in the sample ϕ_ν, E_μ is the energy of the tip states ϕ_μ and E_F the Fermi energy. According to Bardeen's transfer Hamiltonian approach [26], the tunneling matrix element between tip (ϕ_μ) and sample (ϕ_ν) states, $M_{\mu\nu}$, is given as:

$$M_{\mu\nu} = -\frac{\hbar^2}{2m}\int d\vec{S}(\phi_\mu^*\nabla\phi_\nu - \phi_\nu\nabla\phi_\mu^*). \tag{1.1.3}$$

with m as the effective electron mass. The integral is over any surface lying entirely within the vacuum barrier region separating the two sides.

Considering the assumption of a spherical STM tip with asymptotic s-wave functions, Equation 1.1.2 can be expressed as [25]:

$$I_{\mathrm{t}} = 32\pi^3\hbar^{-1}\mathrm{e}^2V\varphi^2\rho_{\mathrm{t}}(E_{\mathrm{F}})R^2k^{-4}e^{2kR}\sum_{\nu}|\phi_\nu(\vec{r_0})|^2\delta(E_\nu - E_{\mathrm{F}}). \tag{1.1.4}$$

Here, $\rho_{\mathrm{t}}(E_{\mathrm{F}})$ is the tip density of states per unit volume of the STM tip, $k = \hbar^{-1}(2m\varphi)^{1/2}$ is the minimum inverse decay length of the wave functions in vacuum, and $\sum_\nu |\phi_\nu(\vec{r_0})|^2\delta(E_\nu - E_{\mathrm{F}})$ represents the local density of states (LDOS) of the sample surface.

The discussion above is based on the assumption of low bias voltage. However, in the experiment, higher bias voltages are always applied to the molecules or atoms on the sample surface. Therefore, taking the finite sample bias voltage into consideration, we can generalize the expression of the tunneling current using the Wentzel-Kramers-Brillouin (WKB) approximation [27]. Then I_{t} refers to

$$I_{\mathrm{t}} = \frac{4\pi\mathrm{e}}{\hbar}\int_{E_{\mathrm{F}}}^{E_{\mathrm{F}}+\mathrm{e}V}\rho_{\mathrm{t}}(E_{\mathrm{F}} - \mathrm{e}V)\rho_{\mathrm{s}}(E)|M_{\mathrm{st}}(E,V,z)|^2dE. \tag{1.1.5}$$

Here, we can observe that the tunneling current I_{t} is represented by the convolution of the density of states (DOS) of tip and sample with the tunneling probability $T(E,V,z) = |M_{\mathrm{st}}(E,V,z)|^2$. The value of this tunneling probability depends on the tip-sample distance z, the energy E and the bias voltage V:

$$|M_{\mathrm{st}}(E,V,z)|^2 = T(E,V,z) = exp\left[-\frac{2z\sqrt{2m}}{\hbar}\sqrt{\frac{\varphi_{\mathrm{s}}+\varphi_{\mathrm{t}}}{2} + \frac{\mathrm{e}V}{2} - E}\right]. \tag{1.1.6}$$

From this formula we notice that the tunneling current depends on a combination of three factors: density of states of tip, density of states of sample, and the tunneling probability. In a first approximation, reasonable for small bias voltages, we can assume the value of φ_{t} and $T(E,V,z)$ to be constant. In this situation, the tunneling current I_{t} can be considered as proportional to the density of states of the surface, integrated in the $(E_{\mathrm{F}}, E_{\mathrm{F}} + \mathrm{eV})$ energy window.

1.1.3 STM Manipulation

An STM system is not only capable of imaging the sample surfaces, but also manipulating molecules or atoms in the nanoscale range. There are mainly two methods of manipulation. One is called lateral manipulation, which means, by utilizing the forces between STM tip and atoms/molecules adsorbed on the sample surface, the movement and the rotation of atoms/molecules can be realized. The other method is called vertical manipulation, which means the STM tip approach very close to the object, an atom for example, accompanied by the build of tip-atom attractive interactions. Then, the tip is slowly retracted. If the tip-atom interactions dominate over the surface-atom interactions, the atom can be vertically transferred to the tip. Similar experiments have been realized with Xe and Co [28, 29].

1.2 Scanning Tunneling Spectroscopy

STM owns another powerful function called scanning tunneling spectroscopy (STS). The spectroscopic information with high resolution from the sample electronic structure can be obtained by establishing the relations between I_t, V and the tip-sample distance z by fixing one of them and determining the dependence of the other two.

Using constant height STS measurements one can record I-V spectra, $\mathrm{d}I/\mathrm{d}V$ spectra and $\mathrm{d}^2I/\mathrm{d}V^2$ spectra. The I-V spectrum reflects the transport properties between STM tip and sample [30]. The conductivity, $\mathrm{d}I/\mathrm{d}V$, is used to detect the distribution of the density of states (DOS). According to Equation 1.1.5, the $\mathrm{d}I/\mathrm{d}V$ signal can be expressed as [27, 31–35]:

$$\begin{aligned}\frac{\mathrm{d}I}{\mathrm{d}V} \propto\ & \rho_{\mathrm{t}}(E_{\mathrm{F}})\rho_{\mathrm{s}}(E_{\mathrm{F}}+\mathrm{e}V)T(E_{\mathrm{F}}+\mathrm{e}V,\mathrm{e}V,z) \\ & + \int_{E_{\mathrm{F}}}^{E_{\mathrm{F}}+\mathrm{e}V} \rho_{\mathrm{t}}(E-\mathrm{e}V)\rho_{\mathrm{s}}(E)\frac{\mathrm{d}T(E,\mathrm{e}V,z)}{\mathrm{d}V}dE \\ & + \int_{E_{\mathrm{F}}}^{E_{\mathrm{F}}+\mathrm{e}V} \rho_{\mathrm{s}}(E)\frac{\mathrm{d}\rho_{\mathrm{t}}(E-\mathrm{e}V)}{\mathrm{d}V}T(E,\mathrm{e}V,z)dE. \end{aligned} \tag{1.2.1}$$

Assuming that the tunneling probability and the DOS of the tip are constant in the considered energy range, the last two terms of Equation 1.2.1 can be neglected. Hence, Equation 1.2.1 can be simplified to:

$$\frac{\mathrm{d}I}{\mathrm{d}V} \propto \rho_{\mathrm{t}}(E_{\mathrm{F}})\rho_{\mathrm{s}}(E_{\mathrm{F}}+\mathrm{e}V)T(E_{\mathrm{F}}+\mathrm{e}V,\mathrm{e}V,z). \tag{1.2.2}$$

This formula means that the tunneling conductance is proportional to the LDOS of the sample at the energy $E_{\mathrm{F}}+eV$. This is only valid under the assumption of low bias voltages. For high bias voltages, the voltage dependence of the tunneling probability has to be taken into account [36, 37].

In STS measurements, there are three working modes for taking spectroscopy: i) in I-z mode, dependence of the current on the tip-sample distance is recorded at a fixed voltage V. ii) in I-v mode, an I-v curve is recorded by sweeping the sample bias while z is unchanged. iii) in V-z mode, I_t is kept constant and the changes in z are recorded for different voltage values.

From the I-z curves, it allows determination of the sample local work function [21]. The I-v mode is the most widely used spectroscopic technique. The feedback loop is opened in order to take an I-v curve. The tip is positioned at a fixed height. The voltage is ramped keeping a constant tip-sample distance and the I_t is recorded over the desired range of voltages. Information about the density of states is contained in the derivative of the tunneling current with respect to the voltage. In the V-z mode, the I_t is kept constant by making the feedback loop closed. By changing the voltage, the tip-sample distance is adjusted to keep the I_t constant. This method can prevent the probed adsorbates from being decomposed by the high tunneling current. It can also enhance the local density of

states (LDOS) at low bias voltages. In comparison, The constant height (I-v) mode is more closely related to the sample states than the constant current (V-z) mode, if the change of the tunneling probability Tz with the barrier width z is taken into account [33, 38]. A general trend is that the LDOS peaks in dI/dV are slightly shifted to lower energy in the constant current mode [38].

Spatially Resolved dI/dV Mapping

The dI/dV mapping technique provides a approach for characterizing the spatial variation of the sample density of state under certain energies. Then, investigation of surface and single molecular electronic configuration such as surface state, local electronic state, interaction of surface and absorbers can be realized by this method, which can be performed in two different modes, constant current mode and constant height mode, respectively. During recording the slow constant current topography image, the dI/dV signal is simultaneously recorded in each point of the XY matrix at a certain bias voltage V. As a result, a map of a certain region at a defined energy eV is obtained and the LDOS signal extracted simultaneously. Since the feedback loop is enabled during the measurement, the frequency of the modulated signal needs to be higher than the cut-off frequency of the feedback loop response in order not to interfere with the z-piezo and change the tip-sample distance.

The constant height mode works at constant tip-surface distance z. In this case, the feedback loop is opened. This measurement mode is preferred to be used for the planar adsorbates on the surface while the constant current mode is utilized for mapping 3D objects.

1.3 Experimental Setup

The STM/STS experiments are carried out under ultra-high vacuum in a low-temperature STM. There are three main vacuum parts of the STM, seen in Figure 1.2 a): The STM chamber, the preparation chamber and the load lock chamber. Each chamber is connected to the others by gate valves. The preparation chamber is also installed with mass-spectrometer, sputter gun, ion-pump and turbo-pump.

Sample transfer is achieved with a movable manipulator. The head of manipulator is especially designed to realize the cooling by liquid helium and resistive heating, respectively. Therefore, the sample temperature can be varied from 80 K to 1000 K. Molecule evaporators are home-made Knudsen cell evaporators and attached to the load lock.

The preparation chamber is used to prepare the sample measurement. A Titanium sublimation pump (TSP) and an ion pump are also connected to the preparation chamber to keep the ultra low background pressure. Ovens for heating up the sample are based on the mechanism of electron bombardment. In most of the conditions, the pressure can be static around 1×10^{-9} mbar or even lower.

The STM chamber hosts two cylindrical dewars, which compose the cooling system of STM. The outer cryostat is filled with liquid nitrogen (LN_2) for screening the outside heat. And the inner cryostat is filled with liquid helium (LHe) to cool the sample. The STM chamber contains the STM scanning unit. It is isolated from mechanical vibrations by stainless steel springs and eddy current damping. The piezo elements are contacted with

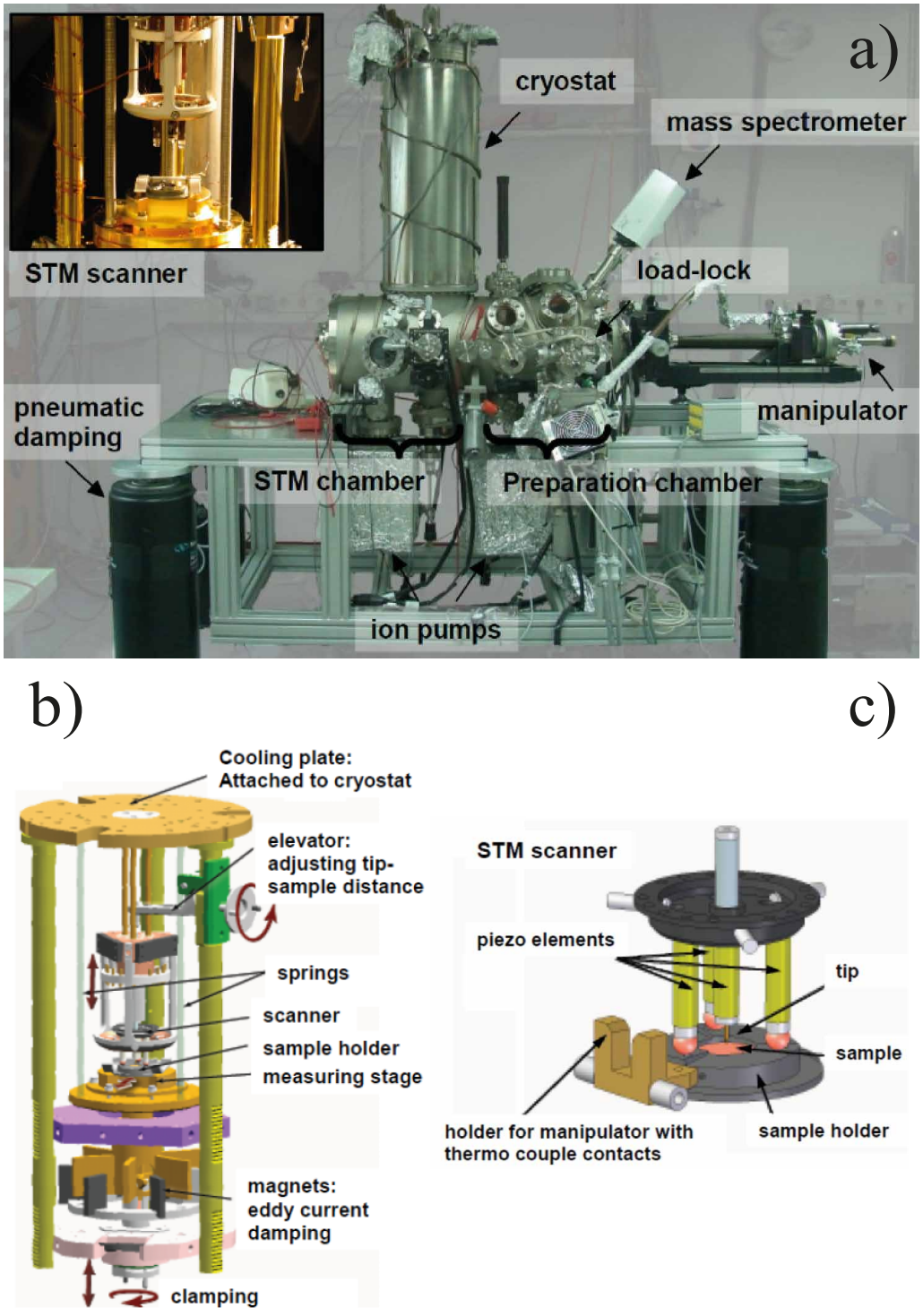

Figure 1.2: a) The image illustrates the UHV chamber with highlighted functional parts. The inset shows the STM scanning unit where the scanning beetle with the four piezo ceramics and the tip is hanging in the cage well above a sample holder with the ramp [39]. **b)** Schematic illustration of STM cooling, clamping and damping mechanisms of the measuring stage. **c)** Zoom of the scanner on the three fold circular ramp, which also used as a sample holder.

the ramp to sapphire balls, shown in Figure 1.2 b) and c). The STM head with tip is along the central axis of the round ramp.

Because of the high sensitivity of I_t, a damping system is necessary to maintain the stable working status of STM. Therefore, the STM is supported by four equal damping feet to filter the low frequency vibrations arising from mechanical movements. STS measurements are recorded with an external commercial Stanford Research SR830 lock-in amplifier. The STM data are analyzed with the WSxM software [40].

1.4 Preparation of Sample and STM Tip

1.4.1 Sample preparation

The single crystalline metal surfaces are cleaned by repeated cycles of Ne^+ sputtering at room temperature with 1.5 keV, typically for 30 minutes, and subsequent annealing to 650-800 K. After getting a clean sample surface, molecules and atoms can be evaporated from the evaporator. It has a quartz balance to measure the frequency change caused by the deposited layer. In order to avoid overheating the crucible of the evaporator, water cooling tubes are connected.

1.4.2 Tip Preparation

The condition of the STM tip is extremely important in the experiment. The shape and electronic configuration will influence the quality of the topography and spectra. In an ideal situation, the apex of STM tip is supposed to be very sharp with only a single atom to contribute the tunneling effect. In the measurement process, some molecules/atoms will sometimes adsorb on the STM tip, which falsifies the measurement results. In order to get a clean STM tip to acquire data properly, the following two ways are usually performed:

1. Applying high voltage to the tip, the emitted electrons lead to the detachment of tip material through electromigration.

2. Tip forming, by indenting the tip into the surface while applying a few volts to the tip. This could help to form a new clean tip, which can be checked by measuring the surface state position and relevant intensities in the STS measurements.

1.5 Substrates used in this thesis

Choosing the right substrates for STM measurements is extremely important, especially in self-assembly experiments. As after evaporating the molecules onto the substrate, the competition between molecule-molecule interaction and molecule-substrate interaction influences the molecular conformation and local chemical environment of the substrate. The structure and shape of the molecular islands can be determined by the choice of the substrate because the shape of molecular islands is highly depended on the molecule-substrate interaction.

In the following experiments, the molecules are investigated by evaporating them onto low-index coinage metal surfaces, Au(111), Cu(111) and Ag(111), respectively. All of these single crystals have a face centered cubic (fcc) structure with lattice constants, 2.88 Å,

2.56 Å and 2.89 Å, respectively. Due to the hexagonal stacking configuration, (111) plane exhibits as threefold symmetry in the first layer with considering the atoms underneath [41].

The electronic properties of these three surfaces share the common points that the surface states are partially filled, showing the surface state onset position at -490 mV of Au(111) [42], -440 mV of Cu(111) [43] and -70 mV of Ag(111) [44, 45].

1.5.1 Au(111)

Among the samples introduced above, the Au(111) surface is special, because it exhibits a herringbone reconstruction. There are stripes with alternating fcc and hexagonally closed packed (hcp) surface layers [46], which can be easily seen in STM images of Figure 1.3 a). The kink positions of the herringbone reconstruction have a lower potential than other surfaces areas, which makes this elbow points the preferential adsorptions sites for molecules and atoms [47, 48].

The formation of the herringbone reconstruction of Au(111) is due to 23 gold atoms in the top layer placed on top of 22 atoms in the second layer, shown in Figure 1.3 b). Therefore the surface layer is stressed and shows a corrugation along the surface $[1\bar{1}0]$ direction. A pattern of fcc and hcp areas appears with a periodicity of 63 Å. The fcc and hcp areas are separated by stacking faults and partial dislocations of the compressed topmost layer, which are called soliton-lines. The corrugation height between two areas is 0.20 ± 0.05 Å, which is largely independent of tunneling parameters and tip conditions [46]. The hcp regions are narrower than the fcc regions, which have a width of 25 Å and 38 Å, respectively [42]. The two-dimensional Shockley surface state band of Au(111) has a binding energy of 490 meV below the Fermi level [49, 50], shown in Figure 1.3 c). The intact of the surface state is important for the $\mathrm{d}I/\mathrm{d}V$ spectroscopy and can be used as a tool to identify the status of the STM tip, since the STM tip with a constant LDOS is the basic requirement for the STM measurement. The long periodicity of the herringbone structure creates a spatial and energetic rearrangement of the surface state causing a binding energy variations about 25 meV between fcc and hcp areas of the reconstruction, respectively [42]. The chemical reactivity with same index surface is different from Au to Cu and Ag. Au is rather inert compared to Ag and Cu. Additionally, the herringbone reconstruction exists neither on Ag(111) nor on Cu(111) surfaces.

1.5.2 Cu(111) and Ag(111)

Figure 1.4 a) and c) show the clean surfaces of Cu(111) and Ag(111), respectively. Neither of both exhibits surface reconstruction. The adsorption of CO molecules is observed as small depressions. Cu(111) has a step-like surface state 450 mV below the Fermi energy, as shown in Figure 1.4 b) [51]. $\mathrm{d}I/\mathrm{d}V$ spectrum in Figure 1.4 d) reveals that the surface state of Ag(111) is localized at -70 mV [44, 45].

1.6 Fabrication Approaches and Electronic Properties of Graphene and Graphene Nanoribbons

Graphene, a single plane of graphite, is well known as its unique honeycomb hexagonal structure consisting of carbon atoms in two-dimension(2D) space and zero band-gap

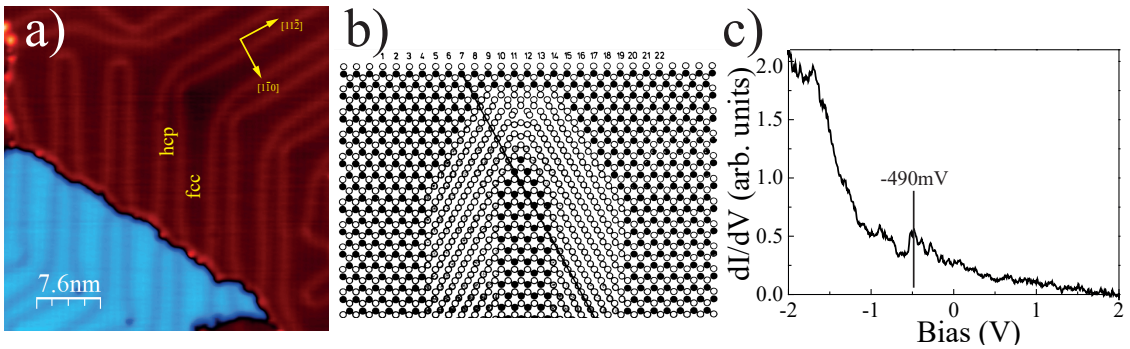

Figure 1.3: Au(111) surface. **a)** STM image of Au(111) with surface reconstruction. (V = 0.8 V, I = 28 pA). **b)** The Au(111) reconstruction model. Open circles represent atoms in the second layer while filled circles stand for atoms in the first layer. (Image is cited from Ref. [46].) **c)** dI/dV spectrum obtained at a clean Au(111) substrate surface with opened feedback. (set point: V = - 2.0 V, I = 0.1 nA).

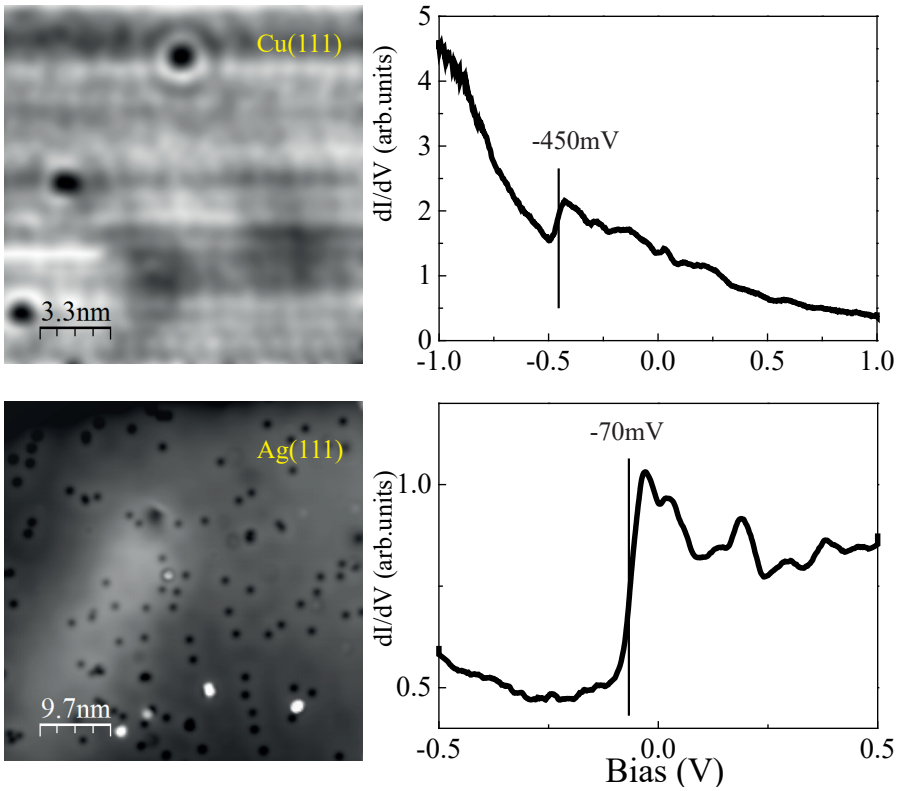

Figure 1.4: Clean surfaces of Cu(111) and Ag(111). **a)** STM image of Cu(111). (V = 1.0 V, I = 0.1 nA). **b)** Surface state of Cu(111) locates at position of -450 mV. **c)** STM image of Ag(111). (V = 0.2 V, I = 0.5nA). **d)** Surface state of Ag(111) locates at position of -70 mV.

electronic property. It arises more and more researchers' interest because of its great performances in conductivity [52, 53], high transparency [54] and thermal stability [55]. It rapidly becomes more and more important not only because the advanced properties mentioned beforehand, but also its controllable growth on the various metal surfaces, which has been widely studied in the past years [14, 15, 52–73].

In order to fully utilize the graphene into the industrial field, the key point is to make graphene from a zero band gap to own a tunable energy gap. The lack of a band gap in graphene limits its application in graphene-based transistors since the low ON/OFF ratio ≈ 10 [74]. Field-effect transistors (FET) require a band gap with about 0.4 eV or even larger values [75]. Therefore, opening the band gap of graphene and even tuning the band gap up to a sufficient value would be the most urgent need for its application.

It has been reported that narrow stripes of graphene also named as graphene nanoribbons (GNR) exhibit a band gap with the size depending on the ribbon width [11, 76]. The electronic properties of GNR are highly depended on the size, shape and edge orientation. For instance, armchair and zigzag shape of GNR are the most common edge structures. Calculation has predicted that zigzag GNRs are always metallic while armchair GNRs can be metallic or semiconducting depending on their width [77].

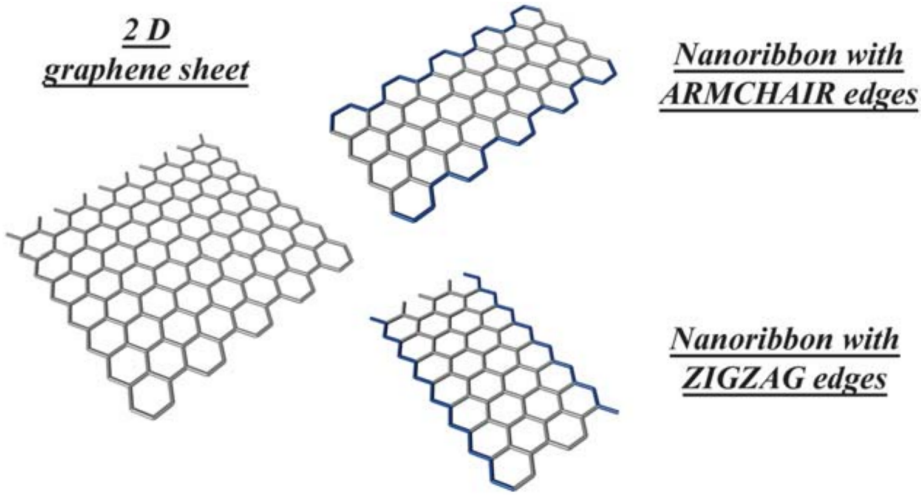

Figure 1.5: Two types of GNRs with armchair edge and zigzag edge. Image is adapted from Ref. [77].

The prediction of ab initio calculations have already shown that, in order to obtain a band gap of 0.3 eV, the width of GNR is supposed to be in the scale of 8 nm or even less [78]. However, considering the carbon-carbon bond length of 1.42 Å a GNR width below 8 nm corresponds to less than 60 carbon atoms across the GNR. The production is difficult for top-down techniques such as lithographic process. Therefore, it is necessary to explore a method to fabricate GNRs with atomic precision and limited defects.

1.6.1 Top-down Method

The well known top-down method of fabricating GNRs is called plasma etching [79]. In this process, graphene sheet grown on metals by chemical vapor deposition (CVD) or epitaxial

grpahene on SiC covered with a mask with desired pattern and then uses plasma to etch away the exposed area, shown in Figure 1.6. Ribbons with about 10 nm width have been realized [80, 81]. Figrue 1.6 shows the schematic process for the fabrication process and resulting GNRs. However, the limitation of top-down method is the poor quality of the graphene products. In the etching process, breaking the chemical bonds by the electron-bombardment is difficult to be controlled. The low controlling over the orientation requires other replaceable fabricating methods.

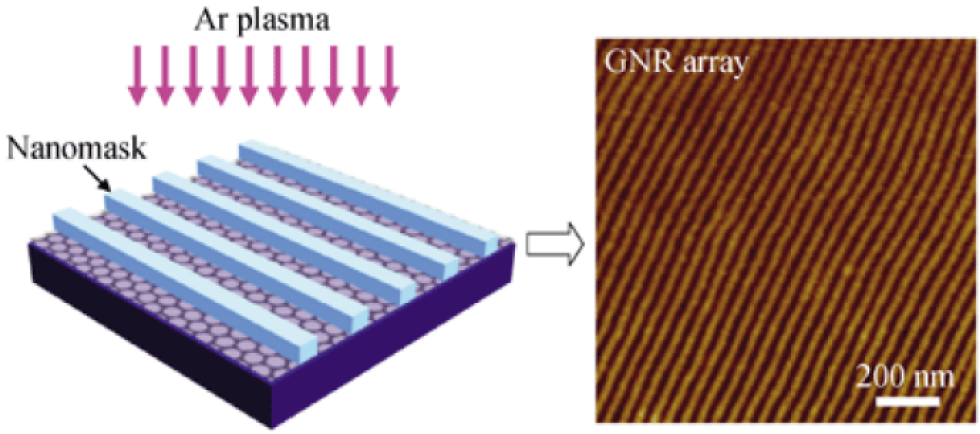

Figure 1.6: Graphene nanostructure made by plasma etching. The image is adapted from Ref. [79].

Chemical reactions provide another method to produce GNRs with large quantities and defined size. Graphite or carbon-based molecules can undergo chemical reactions in solutions and produce GNRs, seen in Figure 1.7 a). However, the obtained GNRs are found to be in a network, shown in Figure 1.7 b). Another method to obtain GNRs is to unzip the single-wall carbon nanotubes (SWCNTs) in solution. This process is schematically shown in Figure 1.7 d). Single GNR has been characterized by a STM on Au(111), shown in Figure 1.7 e). It is understandable that the diameter of GNRs is highly depended on the initial size of SWCNTs.

1.6.2 Bottom-up Method

Bottom-up approach is a substitute for top-down method for fabricating graphene. The advantage of the bottom-up method is to transfer the molecules/atoms onto the solid surface. This is needed in order to fulfill the application demand in the electronic field, large molecular structures and long molecular chains are always needed to form electric circuits. However, the traditional evaporation methods have their limitation due to the proportional ratio between the weight of molecules and the molecular evaporation temperature. Since the larger size of molecules basically requires higher evaporation temperature, it cannot be guaranteed to prepare a sample with low amount of defects under a high evaporation temperature. The large molecules tend to decompose inside the crucible before coming out of the evaporator. Therefore, the on-surface polymerization is a reliable way to avoid the problem mentioned above. Instead of depositing the large and complete GNR, smaller molecular building blocks can be evaporated in the first place. The characteristic feature of these molecular building blocks can be predetermined, in which the chemical bond is

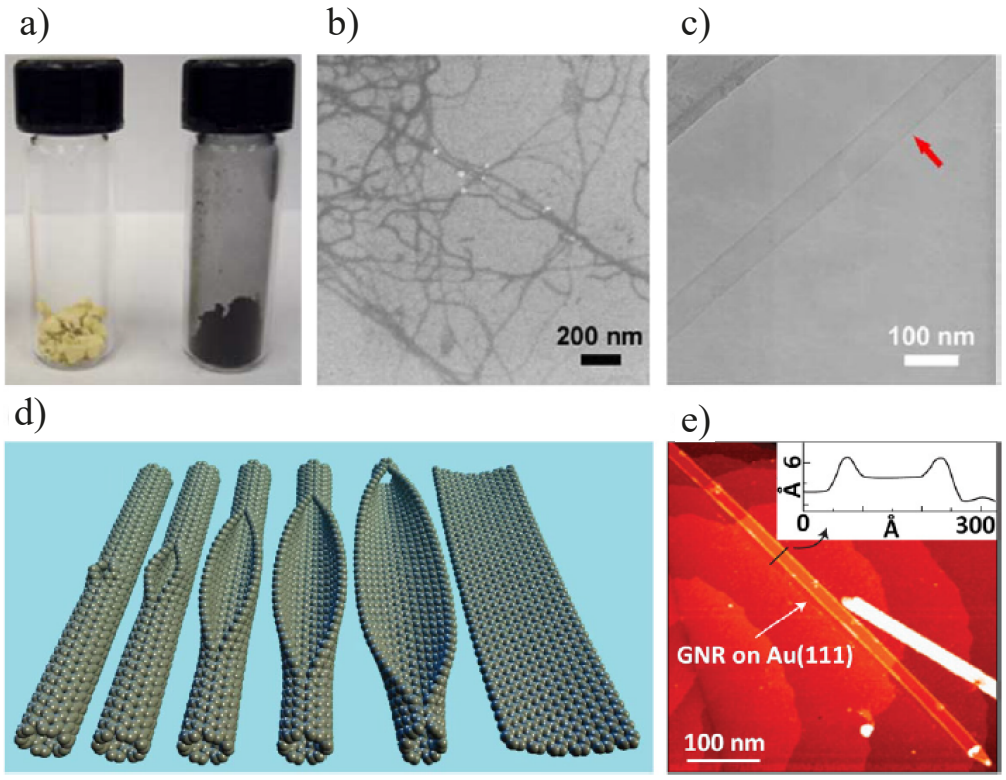

Figure 1.7: GNRs obtained by chemical methods. **a)** Precursor molecular powder and final black GNRs powder. The image is adapted in Ref. [82]. **b)** SEM image of GNRs in solution. **c)** TEM image of a single GNR. The arrow points to a 60 nm wide GNR. Images of **b)** and **c)** are adapted in Ref. [83]. **d)** Unzipping process of single wall carbon nanotubes (SWCNTs) into GNRs by chemical agents. The image is adapted in Ref. [84]. **e)** STM image of unzipped carbon nanotube deposited on Au(111). The inset shows the cross-section profile of the resulting ribbon. The image is adapted in Ref. [85].

designed to break at specific temperatures while the rest part of molecule stays intact [86, 87].

Coupling of the molecular building blocks with covalent bonds by thermally treating the sample has been successfully achieved on the fabrication of different graphene structures [6, 56, 88, 89]. Among them, a bottom-up fabrication method of GNRs, reaction-supported by gold metal surface, was reported in 2010 [14]. 10, 10'-dibromo-9, 9'-bianthryl (DBBA) were used as precursor molecules for fabricating 7-carbon graphene nanoribbons with armchair edges (7-AGNR) on Au(111). In detail, these graphene nanoribbons can be obtained through removing the bromine atoms by annealing the DBBA molecules up to 200 °C on Au(111). From the polymer phase, the GNR is obtained by further heating to 400 °C, which leads to a dehydrogenation and C-C coupling reaction.

According to the previous investigations, the chemical bond with a halogen atom is easier to break. The bond energy of the predetermined breaking point is lower than all other bond energies of the molecule. C-C and C=C bond have an average bond energy of 83 kcal/mol and 146 kcal/mol, respectively, whereas the C-Br and C-I bonds have energies of only 68 kcal/mol and 51 kcal/mol, respectively [90]. The C-H bond also has only a

bond energy of 99 kcal/mol. The basic idea of on-surface polymerization is to combine molecular self-assembly with the Ullmann reaction on a surface. In the previous study in the group of Rieder, the Ullmann reaction was executed with two iodobenzenes molecules adsorbed on the Cu(111) surface [91]. Applying voltage pulses with the STM tip activates both molecules the process of dehalogenation. At the former position of the iodine, a free dangling bond is left and a surface-stabilized radical is created. In the next step, lateral STM manipulation pushes both activated molecules together, and afterwards a final voltage pulse triggers a bond formation and couples them covalently. The two benzenes are covalently linked to a larger biphenyl molecule which has been successfully created on the surface. Therefore, it is necessary and feasible to utilize self-assembly fabrication method and thermal reaction process to narrow the gap between the research in the lab and the application in the application field. Many functionalized precursor molecules, regarded as small building blocks, with functional chemical groups have been widely investigated, and the results represent have a good chance to be used in the molecular devices [92–97, 7].

1.6.3 Photochemical Method

Although chemical methods can make narrow and precise GNRs, the number and amount of reactants as well as the production scaling in the bottom-up thermal reaction is difficult to be controlled. Photoinduced topochemical reactions in solids have overcome the difficulty to predetermine the reaction product by imposing a certain crystal structure and providing highly selective excitation processes. In this case, the original molecular orientation and functionalization of the reactants dictates the reaction product due to limited molecular motion [98–106]. Using this concept as reference to molecules adsorbed in well-defined structures on a metal surface may likely lead to a controlled photoinduced generation of covalently coupled molecular nanostructures.

Photochemical reactions at metal surfaces, such as dissociation and desorption of rather small molecules including diatomic compounds, alkyl halide, and aromatic systems (chloro and iodobenzene) have been studied in detail [107–111]. However, despite a coupling of phenyl radicals forming biphenyl, the report combining investigation on photochemical reactions and thermal reactions is limited [110, 111].

2 Structural and Electronic Properties of DBBA Molecules and Annealing Products on Au(111)

2.1 DFT Calculation of DBBA Molecules

Density functional theory (DFT) calculation of the gas phase of DBBA molecules has been carried out with the help of Gaussian 09 program package [112]. All the calculations including geometry optimizations and electronic excitation energies were carried out on isolated systems, without considering the metal surfaces, using the B3LYP exchange-correlation function. The 6-31G (or 6-311G) basis set was chosen for the DBBA gas phase calculation.

From the gas phase calculation results in Figure 2.1, we observe that the angle between the two anthracene units is close to 90°, which is in a good agreement with the value published in other works [113]. The distance between two Br atoms in DBBA model is 10.8 Å, and the length and width of anthrancene unit is 9.3 Å and 4.8 Å, respectively. In the highest occupied molecular orbital (HOMO), the molecular orbitals are distributed over the whole backbone of the DBBA molecule. On the contrary, the lowest unoccupied molecular orbital (LUMO) is mainly localized at the two anthracene units according to the DTF calculation result.

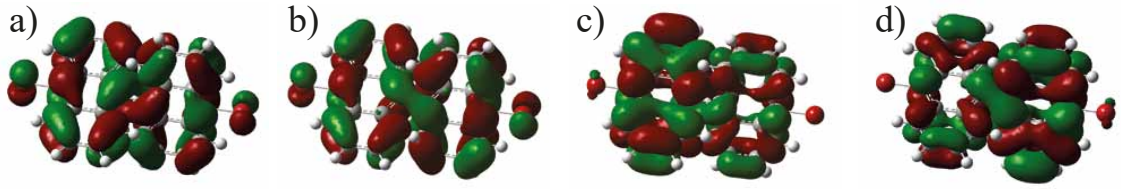

Figure 2.1: DFT calculation result of DBBA gas phase without considering the substrate. Green and red colours indicate the different signs of wavefunctions. **a)** HOMO-1 of DBBA. **b)** Highest occupied molecular orbital (HOMO) of DBBA. **c)** Lowest occupied molecular orbital (LUMO) of DBBA. **d)** LUMO+1 of DBBA.

2.2 Structural Properties of DBBA Molecules

The Au(111) surface has been cleaned in advance by repeated cycles of Ne+ sputtering at room temperature with 1.5 keV for, typically, 30 minutes, and subsequent annealing to 800 K for another 15 minutes. DBBA molecules were evaporated with 400 K evaporation temperature onto the gold surface at room temperature.

Figure 2.2 a) shows the STM image of self-assembled DBBA molecular island on the gold surface. The DBBA molecules exhibit an ordered island consisting of densely packed zigzag stripes of bright protrusions, which grow along the soliton lines of the herringbone reconstruction of Au(111). It can be observed that the molecular island consists of the rows parallel to each other with the same interval between the rows, which is approximately 15 ÅĖvery bright protrusion in the molecular island is known as the upper end of an anthracene unit pointing out-of-plane direction, leading to the bright and round blob feature in the STM images [14].

With STM/AFM combined measuring system, high resolution STM and AFM images were simultaneously recorded by my group colleagues Christian Lotze and Nils Krane, shown in

Figure 2.2 b) and c) [114]. In the STM topography of Figure 2.2 b), two bright protrusions represent the two out-of-plane apexes of the DBBA molecule. The frequency shift image shown in Figure 2.2 c) exhibits ring-lobe features which can be assigned to the highest phenyl ring. The lower part of anthrancene unit is not resolved, since it is adsorbing close to the gold surface. Additionally, dark contrast can be seen at the molecular rim in Figure 2.2 c), indicating attractive tip-sample interaction.

Figure 2.2 e) shows the STM images taken at -1.5V. It reveals that the faint protrusions at the Br moieties. Due to the existence of the Br atoms between the DBBA molecular rows, they tend to interact with each other, leading to the halogen bonding. The distance between the faint protrusions is 3.5 Å, which agrees very well with the halogen bonding distance reported in Ref. [115]. The strength of a halogen bond has been reported comparable with that of a hydrogen bond [116–119]. Therefore, the driving force to make DBBA molecular rows into the DBBA molecular island is the halogen bonding.

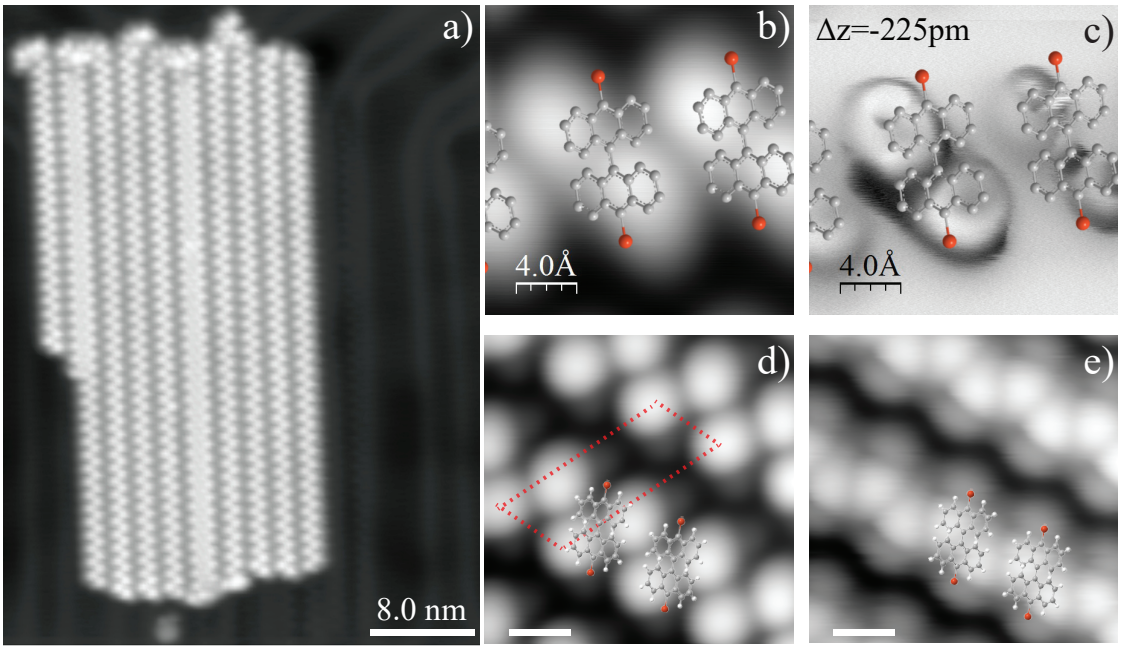

Figure 2.2: STM/AFM topography of self-assembly DBBA molecules on Au(111) surface. **a)** STM overview of DBBA island on Au(111). **b), c)** Constant height STM topography and AFM constant height Δf images at the tip-sample distance ΔZ of 225 pm [114]. The DBBA chemical structure is superimposed onto the STM and AFM images. **d), e)** Zoom-in images of DBBA molecular island. **d)** is taken at V = 1.0 V, I = 50 pA, and **e)** is taken at V = -1.5 V, I = 0.1 nA. The red dot dashed area represents the unit cell. The scale bar in **d)** and **e)** represents 7.6 Å.

To investigate the adsorption behaviours of an individual DBBA molecule, we have also carried out lateral manipulation with the STM tip to the edge bright protrusion of the DBBA molecular island, shown in Figure 2.3. Before the lateral manipulation, we could see that the last DBBA molecule in the row has partly relaxed its 3D structure on the gold surface. The relaxation behaviour of single DBBA molecule at the edge can lead to darker appearance compared to the DBBA molecules within the island. The dark protrusions are laterally dragged out of the molecular island by setting STM tip parameters to I = 5 nA, V = 3 mV, which means the resistance is 600 kΩ. After the lateral manipulation, the last molecule in the row is missing from the edges of DBBA islands and the intact individual

DBBA molecule can be observed in Figure 2.3 b). Note that the individual DBBA molecule relaxes its structure, which is flattened on the sample surface with two darker protrusions symmetrically sitting inside an ellipse shape. The edge of DBBA molecular island has not been influenced by the missing DBBA molecule from the edge.

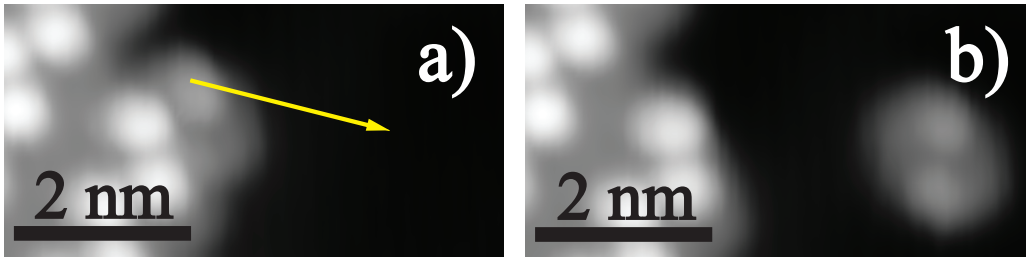

Figure 2.3: Lateral manipulation of DBBA molecules from the edge of molecular island. **a) and b)** STM Images of Individual DBBA Molecule moved laterally by STM tip from DBBA island.(V = 2.0 V, I = 0.1 nA)

Single DBBA molecules have been obtained by repeating the lateral manipulation process. We always observe the detachment of two protrusions from the molecular rows. This agrees with the identification of the molecules based on the AFM measurement. Another isolated DBBA molecule highlighted with colours is shown in the inset image of Figure 2.4 a). Line profile results comparing the single DBBA molecule and rows on Au(111) are shown in Figure 2.4 b). DBBA molecules inside the molecular island show an apparent height of 5.5 Å. The single DBBA molecule is only 3.5 Å height on the gold surface. The 2 Å difference in the apparent height declares that the DBBA molecules within the molecular island are stabilized by the $\pi\cdots\pi$ interactions of aromatic rings in the anthrancene unit play an important role to form the DBBA molecular rows.

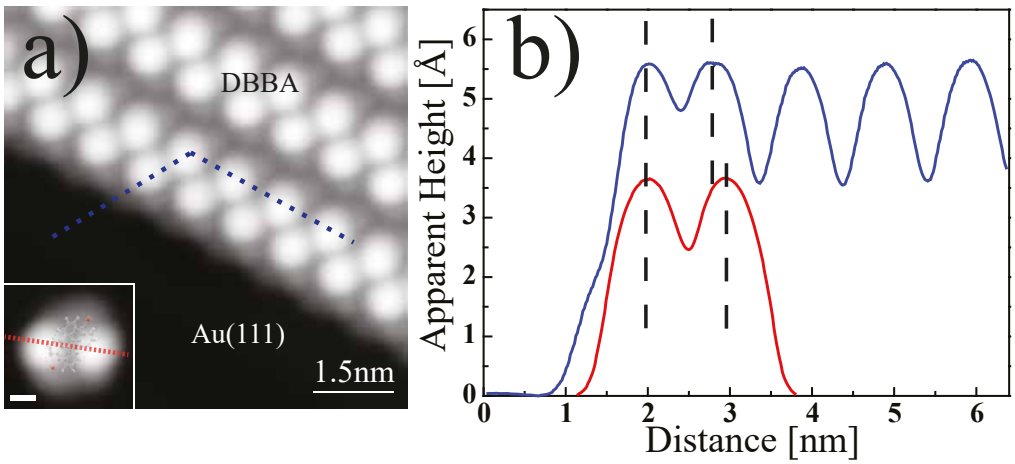

Figure 2.4: a) STM image of DBBA molecular island on Au(111). The individual DBBA molecule is obtained by lateral manipulated from the island. (V = 2.0 V, I = 0.1 nA) The scale bar of inset image represents 4.8 Å. **b)** Apparent height comparison between individual DBBA molecule and DBBA molecular island.

2.3 Electronic Properties of DBBA Molecules

The electronic structures of DBBA molecules in island and individual isolated DBBA molecules are investigated by constant height STS measurement. First, we take the constant height spectra on the clean gold surface as a reference. The black line in the dI/dV spectra of Figure 2.5 b) shows the onset of the Shockley surface state of Au(111) at -490 mV [42]. The constant height STS dI/dV measurement on the DBBA molecular island (green spot in Figure 2.5 a)) reveals that there is a gap of 2.7 eV, which we ascribe to the HOMO-LUMO gap of DBBA molecules on Au(111). The onset located at 1.4 eV and -1.3 eV, respectively. STS measurement with the same parameters on individual DBBA molecules are also shown in Figure 2.5 a). We observe that the HOMO-LUMO gap of the individual DBBA molecule is slightly narrowed down to 2.5 eV. The positions of HOMO and LUMO shifted towards to Fermi level from both sides. We ascribe the down-shift to a larger interaction with the substrate, which arises from the flattening of the individual molecule.

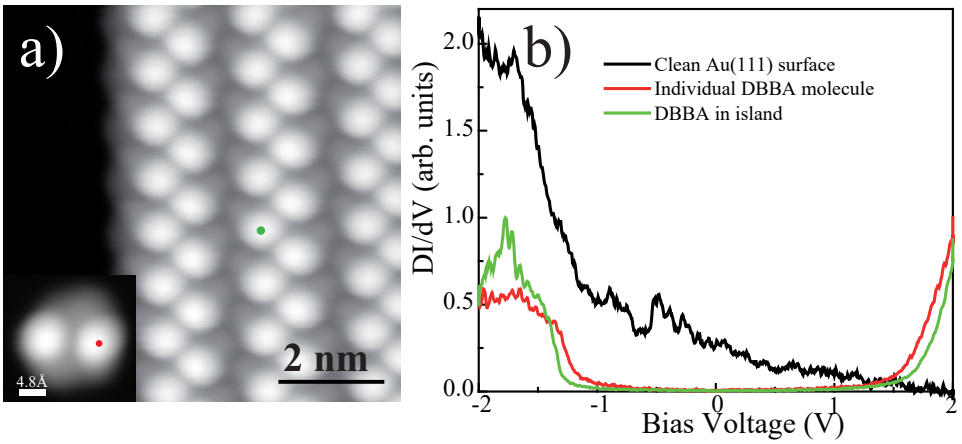

Figure 2.5: a) STM images of DBBA molecular island and individual DBBA molecules (inset). **b)** Constant height dI/dV spectra of clean Au(111), DBBA island and individual DBBA molecule. (Images were taken at $V = 2.0$ V, $I = 0.1$ nA), feedback opened at 0.1 nA and 2.0 V for STS data in **b)**.

Constant height STS measurements in the low energy range has been applied to the DBBA molecular island as well as to the clean gold surface, as shown in Figure 2.6. The measurement points have been marked as blue and orange dots respectively. The graph taken from the clean gold surface shows the onset localized at 490 meV below the Fermi level, which is the characterstic surface state of Au(111) [120]. The onset is shifted to -270 meV on the DBBA island. The reason for surface state shifting has been widely investigated on various metal surfaces, some of which combined with other adsorbates deposited above [121–125]. The origin of surface state shift are generally attributed to the following two possibilities. One is the modification of the image potential by the deposited dielectric medium above the metal surface [125–127]. The other is that a charge transfer process is triggered at the molecule/metal interface leading to the surface state depopulation [128]. Due to the three-dimensional nature and the dense packing of the molecules, we consider a charge transfer unlikely.

2.4 Annealing Products of DBBA Molecules: Polymers and Graphene Nanoribbons

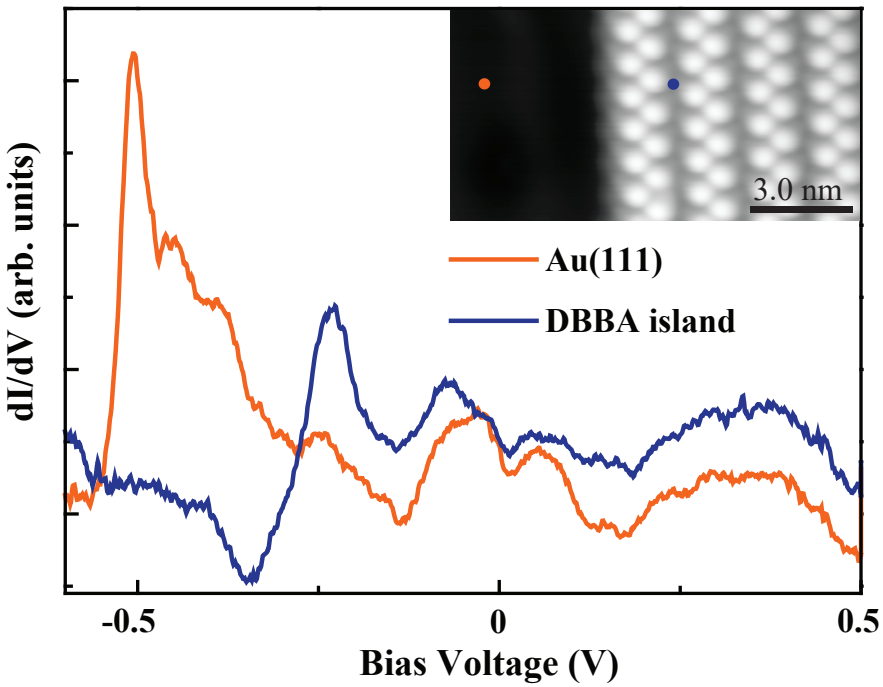

Figure 2.6: Constant height dI/dV measurements on clean Au(111) and DBBA island. The inset STM image shows the positions where the STS were taken. Feedback opened at 0.1 nA and 0.5 V ($V = 2.0$V, $I = 0.1$nA)

2.4.1 Structural and Electronic Properties of Polymer Phases

In order to monitor the influence of heating treatment on DBBA/Au(111) sample, we annealed the sample to various temperatures. In the first place, we heated the sample up to 100 °C for five minutes. This annealing temperature is much lower than that reported for the polymerization in Ref. [14]. Figure 2.7 a) exhibits the overview of the annealed sample.

After zooming in, two characteristic phases are observed on the terrace, seen in Figure 2.7 b). One phase shows a hexamer structure like a flower with six petals (named Phase1). The other phase gives a HARIBO gummy bear impression (named Phase2). In the Figure 2.7 b), Phase1 exhibits the clockwise rotation. A tentative molecular arrangement is shown by the models superimposed on the STM image of Figure 2.7 b). Each pedal of Phase1 represents single DBBA molecule. It is worth mentioning that we keep the Br atoms in the molecular model because the annealing temperature of 100 °C is below threshold temperature of Br atoms detaching from the anthracene units in DBBA molecules [129, 130]. Therefore, the formation of Phase1 is likely a kinetic result rather than the occurrence of dehalogenation process [131]. Besides, it is intriguing to notice that the distance between the Br atoms along the hexamer diagonal is measured to be 3.4 ± 0.1Åand the nearest distance of Br-Br within the hexamer is 1.8 ± 0.1Å, shown in Figure 2.7 c). This distance value suggests that the possibility of the formation of a halogen bond, which is comparable with the strength of the hydrogen bond [116–119]. Additionally, the existence of a weak CH$\cdots\pi$ bond is also possible between the adjacent DBBA molecules [113]. This observation indicates that, under the 100 °C annealing temperature, DBBA molecules prefer to form the homochiral packing through the halogen bonds instead of forming covalent bonds

through chemical reaction. The strengthened intermolecular interactions help to stabilize the hexamer structure on the gold surface.

Comparing to the amount of Phase2, the amount of Phase1 is much smaller through randomly scanning the different areas of the sample (Figure 2.7 a)). Hence, Phase2 needs also to be further studied, shown in Figure 2.7 b) and c). Phase2 consists of three bright parts. The length of Phase2 is less than 3.0 nm according to measurement result shown in Figure 2.7 d). Hence, each bright part can be likely single DBBA molecule. The middle area of Phase2 exhibits two symmetric protrusions, reminding us these would probably be the out-of-plane phenyl rings of the anthracene unit of single DBBA molecule. Therefore, molecular models have been tentatively superimposed on the Phase2. It is notable that, instead of the parallel configurations like in the DBBA molecular island without annealing, three DBBA molecular models with the zigzag configuration fit very well on the STM image of Phase2. The most likely reason of forming this trimer can be ascribed to combined influence of the intermolecular interactions of the halogen bonds between the Phase2 rows, as well as the CH$\cdots\pi$ interaction inside the trimer. Therefore, 100 °C annealing temperature cannot completely trigger the dehalogenation reaction process but offering DBBA molecules enough kinetic energy to realize the local rotation, leading to the formation of the DBBA hexamer and the DBBA trimer. The larger amount of Phase2 suggests that the Phase2 configuration lowers the total energy and makes the system more stable and preferable. It is worth to emphasize that we cannot rule out the possibility that a small part of the Br atoms have detached from DBBA molecules in the Phase2, leading to the covalent bonding inside the trimer. The detachment of Br atoms is likely due to the local over-heating in the molecular crucible during the evaporation process.

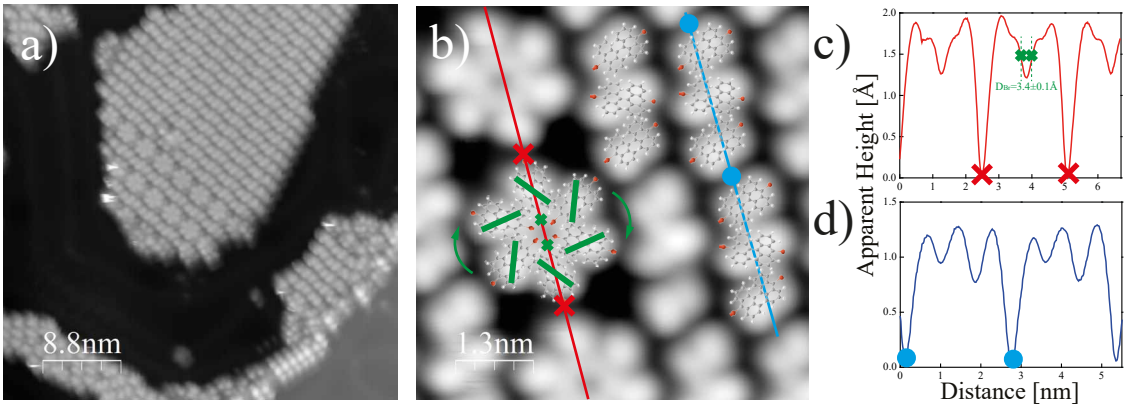

Figure 2.7: Topography of the sample obtained under the annealing temperature of 100 °C. **a)** STM overview of the sample obtained after annealing at 100 °C. **b)** An STM image containing Phase1 and Phase2. DBBA molecular model has been tentatively superimposed. Line profile measurements have been measured along two different phases. (V = 1.0V, I = 0.1nA) **c)** Line profile result of Phase1. **d)** Line profile result of Phase2.

By following the fabrication recipe introduced in ref. [14], the DBBA molecules on Au(111) is annealed up 200 °C for ten minutes. Thermal treatment triggered the Ullmann reaction of DBBA molecules on Au(111), leading to polymer chains (Figure 2.8 a)). From the overview image, the polymer phase island can be clearly observed, growing from the step edges of Au(111). Individual polymer chains can also be seen on the terrace of Au(111) in Figure 2.8 a). Polymer chains are up to 20 nm long. The chains arrange parallel to each other (Figure 2.8 b)). The driving force to make the polymer chains stick to each other is

supposed to be the $\pi \cdots \pi$ interaction. This explains that single bright protrusion of the polymer chain always faces to the space between the two protrusions of the neighbouring polymer chain (Figure 2.8 c)). From the graph in Figure 2.8 d), it is notable that the protrusions have a center to center distance of 0.74 nm which is comparable with the center to center distance between protrusions in the case of DBBA molecular island, which is 0.8 nm. Therefore, it is proposed that at this stage Br atoms have dissociated from the DBBA molecules and covalently bond formation has taken place. The slight difference in distance on the height of DBBA molecule and polymer phase on Cu(111) has been observed [132]. If the chains are lying flat they would have an apparent height of 0.2 ± 0.02 nm (as shown below after the formation of GNR). The apparent height of the chains here is 0.46 ± 0.05 nm as shown in line profiles in Figure 2.8 d), confirming that the anthracene chains are tilted with respect to the Au(111) surface. Steric hindrance between the hydrogen atoms of adjacent anthracene units induces rotation around the connecting C-C bond which leads to this tilting effect and the larger apparent height comparing GNR[133]. An angle of 33° between the anthracene plane and surface normal has been reported by Klues et al. [134].

To prove the covalent bond formation, we drag the molecular arrangements across the surface with the STM tip. Figure 2.9 b)-g) are the STM images of two oligomers with different lengths observed on the terrace of Au(111). The longer oligomer consisting of 16 anthracene units was laterally manipulated 5 times by setting the identical parameters of STM tip, $V = 3$ mV, $I = 2$ nA, which means the resistance is 1.5 $M\Omega$. The oligomer is still intact with constant length and number of bright protrusions after the series of lateral manipulation. The manipulated part can be bent by 180 ° without cleaving the oligomer chains (comparing b) and e)). Therefore, the thermal reaction produced strong covalent bonds between the DBBA molecules.

Around the polymerized phase, some dark fractions with height of 1.8 ± 0.3 Å can be observed highlighted by red dotted square area in Figure 2.9 g). The apparent height of this area is close to the typical AGNRs height [14], which is 0.18 nm. This highlight area might be a defect or a dirt on the surface, but it also cannot be ruled out the possibility of partial formation of GNR patches. This dark fraction also plays a role as an anchor, which fixes the polymer chain on the gold terrace during the lateral manipulation process. Furthermore, lateral manipulation also overcomes the barrier of a 0.2 Å corrugation between fcc and hcp area without breaking or reacting with the surface, reflecting the physical strength and chemical stability of the covalent bonds.

In order to examine whether the electronic properties of the polymerized chain dramatically change during lateral manipulation, constant current $\mathrm{d}I/\mathrm{d}V$ spectra at the positive bias have been recorded. In Figure 2.10, two broad resonances localized at 1.8 eV and 2.8 eV can be observed, which we ascribe them to the LUMO and LUMO+1 of the polymerized chain. By comparing the graphs in Figure 2.10 c) and d), the resonances are not dramatically influenced in the location and intensity by the lateral manipulation. Hence, the lateral manipulation of the polymerized chain not only proves the strong covalent bonds forming inside the chain, but also keeps their electronic properties.

In order to track possible intermediate reaction products, two more different annealing temperature above 200 °C experiments have been performed.

Figure 2.11 a) shows an overview of the sample annealed up to 250 °C. From the overview we could observe that, on one hand, parts of the polymers keeps their characteristic fea-

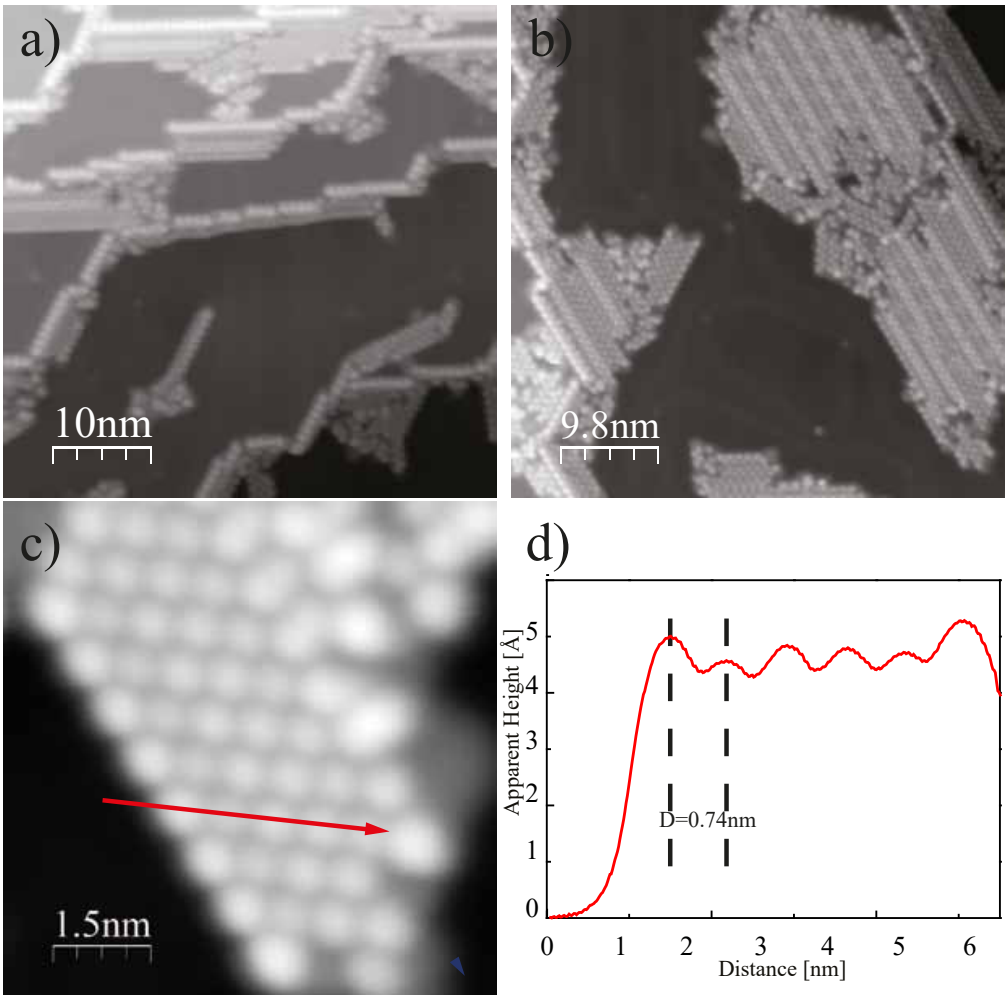

Figure 2.8: STM topographies of polymer phase on terrace and step edges on Au(111). **a)** STM overview of polymer phase on Au(111). Individual polymer chain can be observed in the terrrace of Au(111). **b)** Large polymer island formed with polymer chains on Au(111). **c)** Zoom-in image of polymer island. Line profile along the direction labeled by red arrow. **d)** Line profile graph obtained from **c)**. The center to center of bright protrusions is labeled as D = 0.74 nm.

tures as ones obtained at 200 °C annealing temperature. On the other hand, in the same overview, one can find that some polymer chains have partly changed their 3D appearance into the smooth configuration without obvious internal contrast. The line profile measurements show an apparent height of the bright protrusion is 4.2 ± 0.2 Å which is in a good agreement with the apparent height of polymer chain. The center to center distance of two bright protrusions along the line profile is 0.74 nm, matching well with the polymer chain measurement result. The flat part is only 2.2 Å height (see Figure 2.12 and Figure 2.14, respectively). This observation illustrates that cyclodehydrogenation process has already started from one end of the polymer chain when annealing the sample up to 250 °C. The ribbon shown in Figure 2.11 b) represents a half-GNR chain obtained by the occurrence of a cyclodehydrogenation process from one terminal.

From Figure 2.11 b), we propose the following reaction process. Firstly, the flattening process took place in the lower part of anthracene unit in a zigzag way along the growing

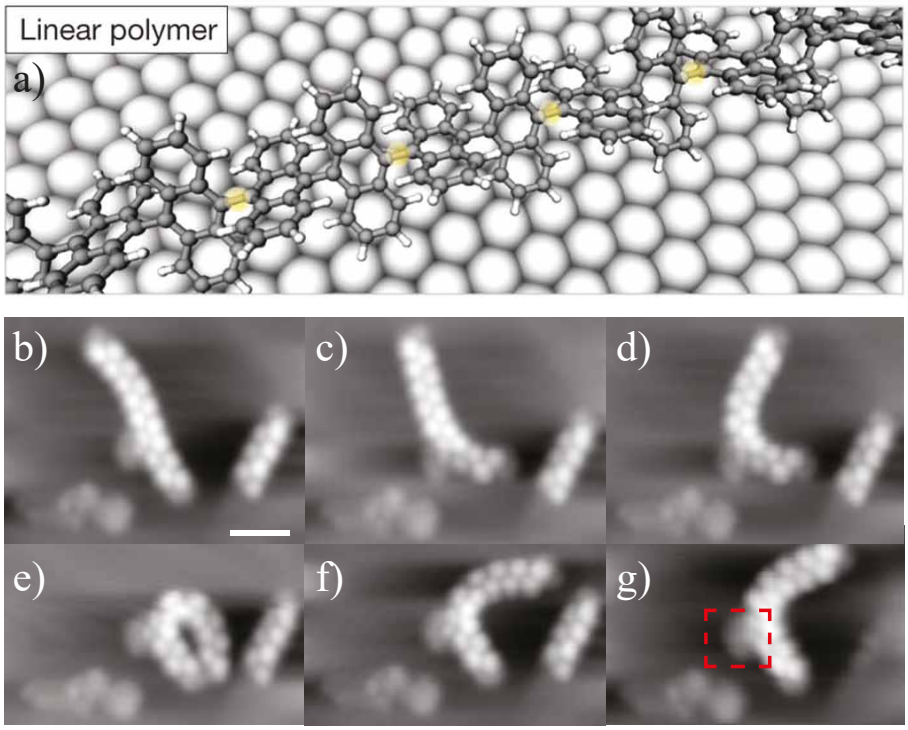

Figure 2.9: Lateral manipulation of a single polymerized chain on Au(111). **a)** Formation of linear polymers by covalently interlinking of the dehalogenated intermediates [14]. **b-g)** After five times manipulation on the longer oligomer, the polymer chain keeps intact and the maximum bending angle could reach 180° by comparing **b)** and **e)**. The red dotted area in **g)** shows an area with apparent height 1.8 Å. All the images are taken at $V = 1.0$ V, $I = 40$ pA. The scale bar represents 2.7 nm in the images from **b)** to **g)**.

direction of the chain. Then, in analogy to the failure of domino effect, 250 °C annealing temperature is not capable of providing enough energy to support the whole polymer chain to overcome the increasing energy barriers generated in the cyclodehydrogenation process. Therefore, fully cyclodehydrogentated GNR can be only obtained with higher annealing temperature above 250 °C. We also observed structures, which exhibit protrusions on one side of the polymer, but are flat on the other half (Figure 2.11 d)-f)). This suggests that domino reaction of the cyclodehydrogenation along half of the polymer chains.

This phenomenon clearly confirms that there are two cyclodehydrogenation process channels opened below 400°C before reaching the complete GNR phase. One is starting cyclodehydrogenation process from the single terminal of polymer chain in a zigzag way, and the other is beginning with the half of the polymer phase along the long axis of the polymer chain. It is difficult to find one phase under the sample of the other phase, and this is due to the competition between these two processes under each annealing temperature. The energy barriers in these two processes need to be further investigated with DFT calculation.

2.4.2 Heat-generated graphene nanoribbons

In the following part, we report on the products after annealing to 400 °C. From the overview image in Figure 2.12 a), we could observe straight molecular chains with various

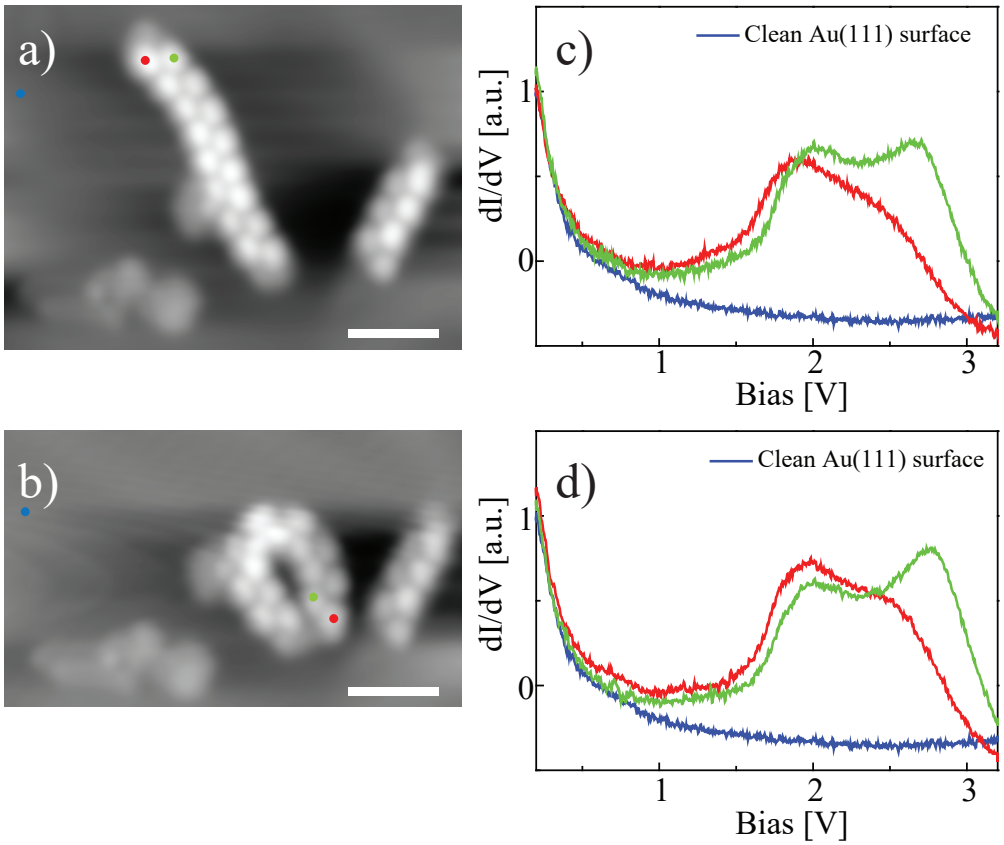

Figure 2.10: dI/dV STS measurements of single polymerized chain before and after lateral manipulation. **a)** Before lateral manipulation (V = 0.6V, I = 10pA). **b)** After lateral manipulation (V = 1.0V, I = 40A). **c)** and **d)** Constant current STS measurements on the oligomer chain on Au(111) surface. Feedback is closed in **a)** and **c)**, and set point is 50 pA and 0.2 V.

length and identical width distributing on the gold surface. These chains are atomically precise seven-armchair graphene nanoribbons (7-AGNR) with hydrogen terminated edges lying on the gold surface which has also been confirmed with the same preparation conditions in some other work [14, 135].

The GNRs appear smooth with little internal structure, and instead of forming GNR island, they are distributed separately from each other on Au(111). This can be ascribed to the repulsive force induced by the side hydrogen atoms of GNR. In the overview image of 520 × 520 nm^2 in 2.12 a), the longest GNR could reach more than 30 nm and the GNR orientation is random, suggesting that there is weak interaction between the GNRs and the underlying Au substrate. We also observe some T-shaped structures in the overview image, highlighted with yellow dotted circle in Figure 2.8 a). According to the explanations in the former reports, partial dehydrogenation and missing hydrogen positions create new active sites for bonding [136, 137]. Therefore other activated GNRs could bind to these active sites, leading to the T-shaped structures.

Figure 2.12 b) is a zoom-in image of one terminal of a GNR and the apparent height is measured as shown in Figure 2.12 c). The zoom-in GNR image shows the terminus as "two eyes and three antennae" [64]. By taking the constant height dI/dV measurement on

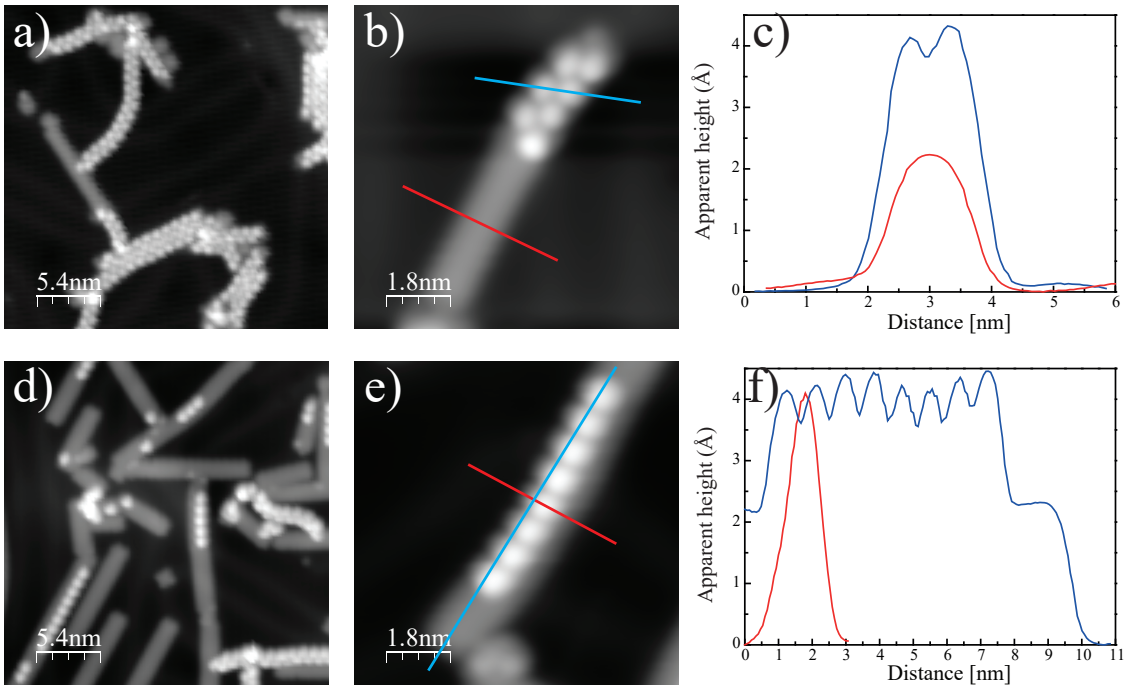

Figure 2.11: Polymerized samples obtained under two different annealing temperatures. **a)** Overview of the sample annealed to 250°C (V = 1.0 V, I = 11 pA). **b)** Zoom-in STM image of the sample annealed to 250°C (V = 1.0 V, I = 0.1 nA). **c)** Line profile results of **b)**. **d)** An overview image of the sample annealed to 330°C (V = -1.0 V, I = 0.1 nA). **e)** Annealed to 330°C (V = -2.0 V, I = 0.1 nA). **f)** Line profile results of **e)**.

the position of zigzag termini around zero bias voltage, which is the black dot shown in Figure 2.12 b), we could obtain a spectrum with an obvious asymmetric resonance below the Fermi level, which owns a sharp onset shown in Figure 2.12 d). This resonance has been identified as Tamm State [64, 85]. The sharp peak close to Fermi energy shown in Figure 2.12 d) belongs to two flat bands with a wave vector k between $2/3\pi$ and π close to E_F [12]. This state cannot be obtained at the armchair edges of GNR [12].

Measuring electronic states with large $k_{\|}$ values is unusual in STM because the decay rate of the tunneling current increases with $k_{\|}$, which is equivalent to less efficient tunneling of electrons with large $k_{\|}$ [35]. Generally speaking, in the STM system, electronic states with $k_{\|} \approx 0$ dominate the tunneling current. Only if there exist no states with small wave vectors tunneling from states with larger $k_{\|}$ can be observed [36]. This seems to be the reason which can explain our experiments since the Tamm state is localized close to the Fermi energy at a k-vector between $2/3\pi$ and π [12]. However, one cannot estimate k of the tunneling electrons due to the unknown of effective mass of the electrons. The topographies show that the appearances are different of GNR taken under small and large voltages Figure 2.13. At high bias voltages (both positive and negative), the terminal of GNRs is featureless. On the contrary, taking images between -0.2 V and +0.2 V has a high resolution of the appearance of the GNR terminus. Figure 2.13 c) and d), taken under -0.05 V and 0.05 V, respectively, show a "two eyes and three antennae" terminus. The small bias window and the Tamm state which is located at 0.03 V in the dI/dV spectrum, point out a property of an electronic not a topographic effect of GNR. However, the theory predicts that the Tamm state of AGNRs should split in energy due to an antiferromagnetic coupling between

the individually ferromagnetic edges has not been observed to the 7-AGNRs obtained in our experiment [66].

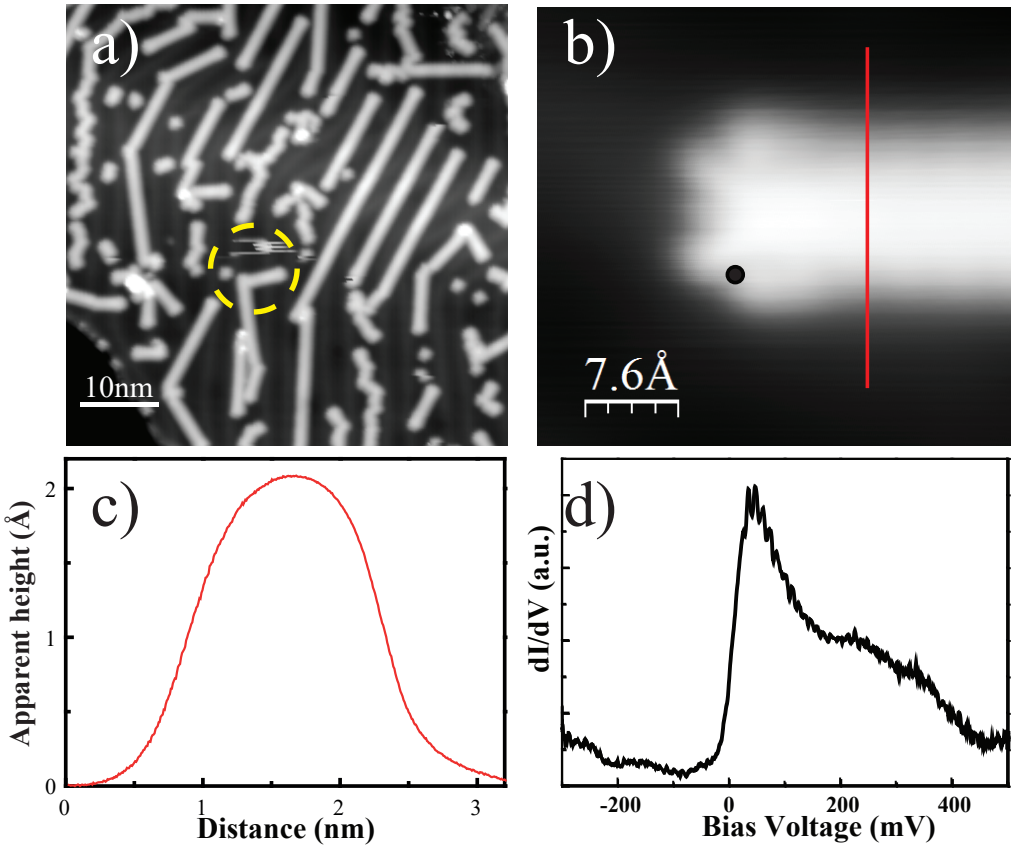

Figure 2.12: Thermally induced GNRs sample on Au(111). **a)** Overview of GNRs obtained by annealing DBBA submonolayer molecules up to 400°C. The size of image is 520 × 520 nm^2. **b)** One terminal of single GNR on Au(111). Red line represents the line profile which showed in **c)**. Image is taken at V = -0.05 V, I = 0.1 nA. **c)** Line profile of GNR on Au(111). **d)** STS measurement at the black spot position around Fermi level shown in **b)**. Feedback opened at 0.1 nA and 0.5 V.

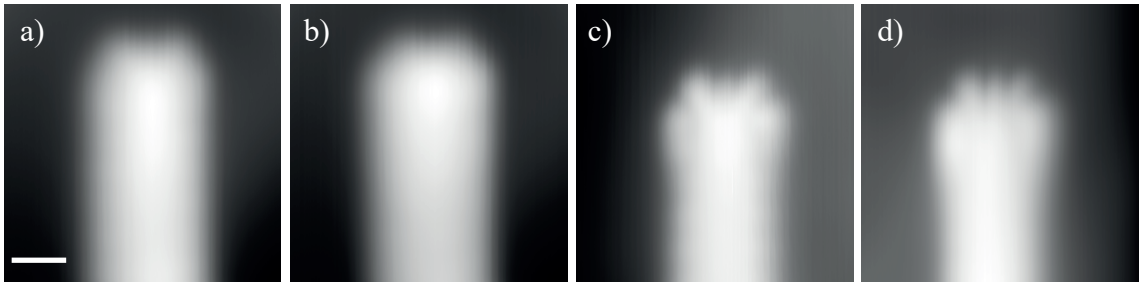

Figure 2.13: GNR topogrophies taken under different bias voltages. **a)** V = -2.8 V, I = 0.1 nA. **b)** V = 2.0 V, I = 0.1 nA. **c)** V = -0.05 V, I = 0.1 nA. **d)** V = 0.05 V, I = 0.1 nA. All the images are with the same size and the scale bar represents 7.6 Å.

The apparent height of GNRs on Au(111) under various biases has been measured, shown in Figure 2.14. From the data with error bar, we find the apparent height of GNR is much lower than a DBBA height of 5.5 Å and polymer height of 4.6 Å, respectively. The average

height is 1.90 ± 0.25 Å. This small fluctuation in the value indicates that the apparent height of GNRs on Au(111) is bias independent.

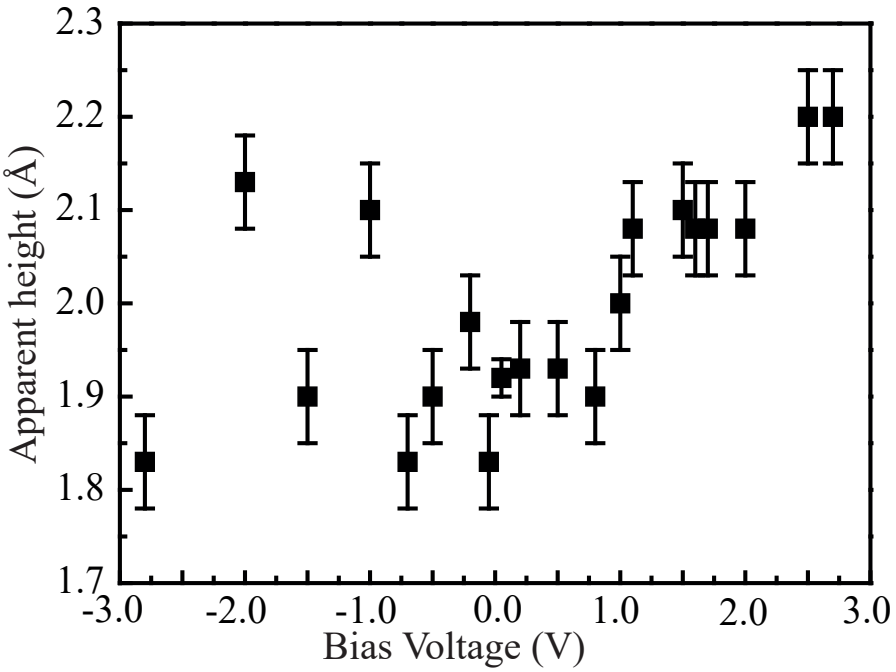

Figure 2.14: Apparent height of GNR on Au(111) under various voltages. Error bars are due to the different arbitrary measurements of GNR. Average height is 1.90 ± 0.25 Å.

We have carried out the experiment of lateral manipulation on individual GNR on the terrace of Au(111) like we have performed on the polymer chain. Figure 2.15 shows the process of lateral manipulations with STM tip. In total, we have already performed five times lateral manipulations on a short GNR with setting STM tip $V = 3$ mV and $I = 40$ nA. Another GNR can be observed in all the topographies as a reference. The intact shape of GNR after multiple lateral manipulations suggests that the interaction between GNR and Au(111) surface is rather weak, and the covalent bonding inside GNR is rather strong. These properties agree very well with the strength properties of graphene material [58].

Constant height and constant current $\mathrm{d}I/\mathrm{d}V$ spectra were carried out on GNR, shown in Figure 2.16 a). In the constant height $\mathrm{d}I/\mathrm{d}V$ spectrum, the signal increases below -0.9 eV which can be assigned to a tail of the HOMO of the GNR at -1.1 eV (the graph of Figure 2.16 b)). The LUMO resonance of GNR can be observed at +1.7 V. The HOMO-LUMO gap thus amounts to 2.8 eV which is in a good agreement with the published result of E_g = 2.8 ± 0.4 eV [138]. We could also observe the small resonance at the Fermi level, which is associated to the Tamm state originating from the zigzag edges. The Tamm state can be also confirmed by the $\mathrm{d}I/\mathrm{d}V$ map, seen in Figure 2.16 d).

In contrast, at LUMO energy of +1.7 V, a bright feature decorates the armchair edges of the GNR. Therefore, the LUMO is delocalized along the armchair edges of the GNR. The STM topography and $\mathrm{d}I/\mathrm{d}V$ map at a bias voltage inside the HOMO-LUMO gap, which is $V = 1.0$ V, is shown in Figure 2.16 g) and h). In the STM topography, no obvious feature can be observed. In the $\mathrm{d}I/\mathrm{d}V$ map, due to far away from the LUMO energy, the low conductivity phenomenon can be seen due to the dark side area in the Figure 2.16 h).

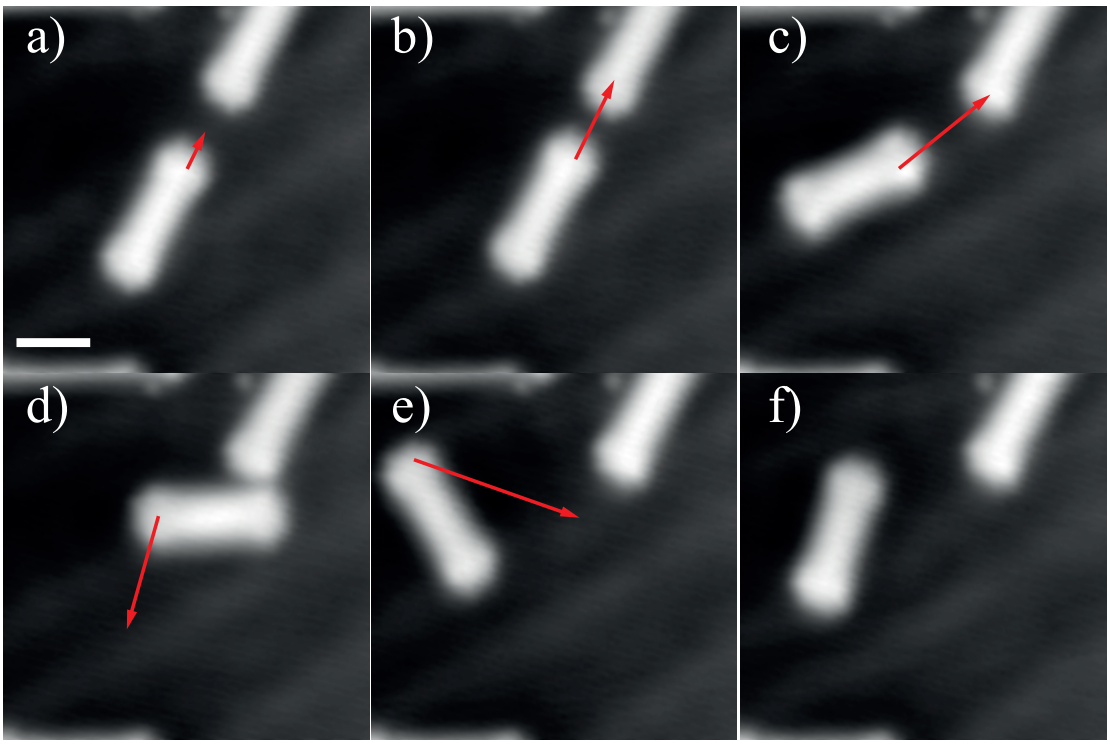

Figure 2.15: Lateral manipulation of GNR on Au(111). The red arrows in the images clarify the manipulating direction at each time. Images from **a)** to **f)** are taken at $V = 0.05$ V, and $I = 5$ pA. The lateral manipulations are carried out by setting $V = 3$ mV, and $I = 40$ nA. The scale bar represents 2.4 nm.

STS line spectra have been measured in the LUMO energy range across GNR (labeled by the yellow arrow), perpendicular to the growth direction of the GNR. The line spectra in Figure 2.16 b) reflect the strong charge in LUMO intensity across the GNR in agreement with the $\mathrm{d}I/\mathrm{d}V$ maps. The LUMO is located at the armchair edges.

2.5 Investigation of Laser Illumination of DBBA Precursor Islands

As described in the previous section, atomically precise GNR can be obtained by annealing self-assembled DBBA molecules on Au(111). However, the limitation of this approach is the lack of possibility to locally control the synthesis by triggering the reaction on the whole substrate surface. Topochemical reactions circumvent this problem. In this approach, molecules are immobilized on the surface and coupling reaction is triggered by light. Following this concept, we investigate the effect of laser illumination of the DBBA molecules on Au(111).

We use a UV laser to illuminate the sample which is kept being cooling with LHe. We have conducted three experiments in total and the preparation details can be found in Table 2.1. In order to quantify light-induced reactions by a cross section, photon dose d can be expressed as:

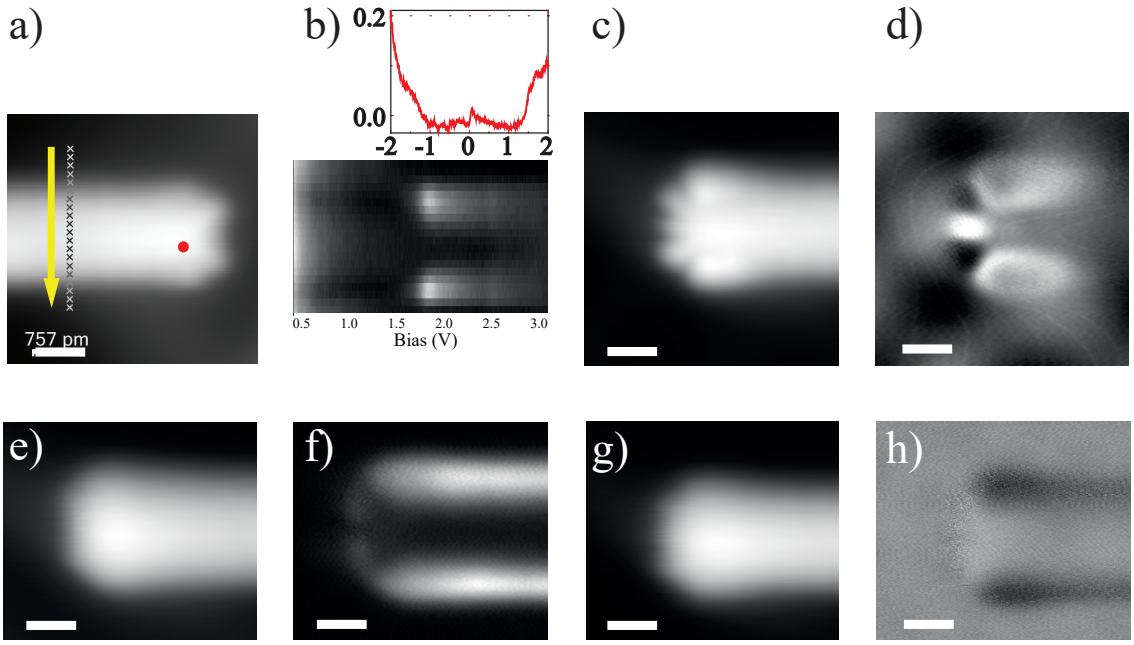

Figure 2.16: Line spectra across the graphene nanoribbon along the direction highlighted with yellow arrow. Measuring points are labeled with small crosses. **a)** STM image of GNR with one terminal (V = -0.2 V, I = 0.1 nA). **b)** Line STS across the GNR in **a)** (V = 0.5 V, I = 40 pA) (Feedback is closed and set point is 50 pA and 0.2 V.). The graph shows the constant height dI/dV spectrum of GNR, measuring position is highlighted in **a)** with a red point (Feedback opened at 0.1 nA and 2.0 V). **c)** Topography of GNR taken at V = 0.05 V, I = 0.1 nA. **d)** dI/dV map of GNR in **c)** taken at V = 0.05 V, I = 0.1 nA. **e)** Topography of GNR taken at V = 1.7 V, I = 0.1 nA. **f)** dI/dV map of GNR in **e)** taken at V = 1.7 V, I = 0.1 nA. **g)** Topography of GNR taken at V = 1.0 V, I = 0.1 nA. **h)** dI/dV map of GNR in **g)** taken at V = 1.0 V, I = 0.1 nA.

$$\mathrm{d}[cm^{-2}] = 47.686 \times 10^{24} \frac{P[\mathrm{mW}] \times t[\mathrm{min}]}{h\nu[\mathrm{eV}] \times D^2[\mu\mathrm{m}^2]} \tag{2.5.1}$$

Where P represents the time-averaged power of the laser beam, t is the illumination time length and D is the laser spot diameter [139]. The illumination is provided by a ArF excimer laser with working wavelength λ = 193 nm, which means $h\nu_{illu.}$ = 6.42 eV.

Preparation	Laser Power (mW)	Illumination Time (hours)	Illumination area (mm^2)	Photon dose (cm^{-2})
1st	30±2	1.0	2×2	3.3×10^{33}
2nd	29±2	1.0	3×3	1.4×10^{33}
3rd	23±1	2.5	2×2	5.1×10^{33}

Table 2.1: Preparation details of laser illumination experiments.

Figure 2.17 a) shows the STM image obtained from the 1st preparation. After 1 hour UV laser illumination on the sample surface, we could see that the drastic modification of the

molecular appearance has taken place. Instead of observing DBBA molecular island with characteristic zigzag pattern introduced above, the islands illuminated by laser exhibited a strong disorder without any clear structure on Au(111). However, the shape of the islands is similar to before, which points to a small diffusion deriving from laser illumination.

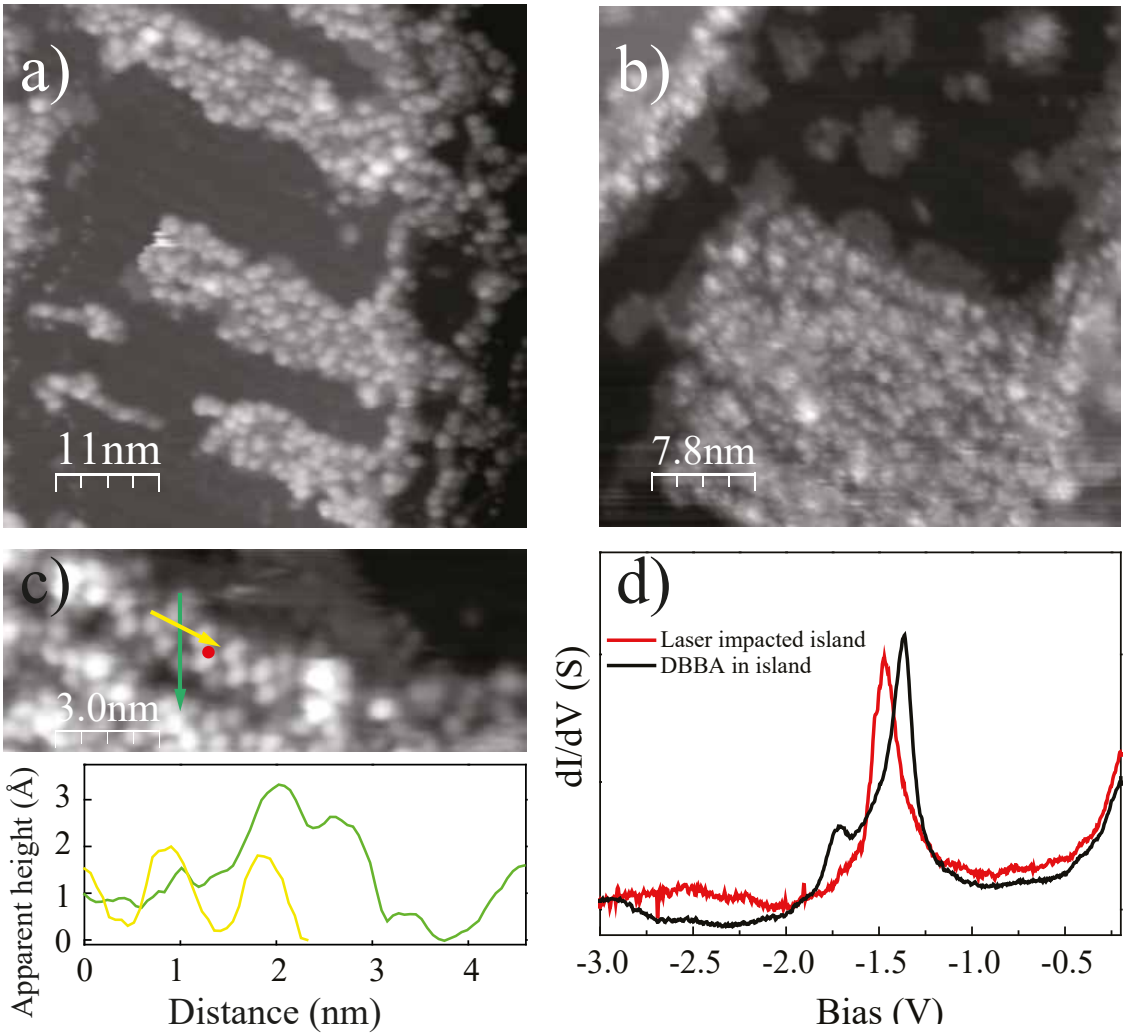

Figure 2.17: Laser induced sample obtained with STM measurements. **a)** STM image of DBBA molecular island illuminated by laser in the 1st preparation. (V = 1.0 V, I = 18 pA) **b)** An image of illuminated sample with some ordered structures obtained from the 2nd preparation. (V = 0.56 V, I = 30 pA) **c)** The zoom-in image of **b)** and line profile result. **d)** Constant current STS measurements comparison between on laser impacted island and on DBBA precursor in the molecular island. Feedback is closed at 50 pA and -0.2 V.

The STM image of Figure 2.17 b) is obtained from the 2nd preparation. It shows a molecular island found on Au(111) with intact island shape and limited clear structures inside. After zooming in the area highlighted by red dotted circle in Figure 2.17 b), a small amount of ordered structure can be observed. From the graph shown in Figure 2.17 c), we find that the former distance is 0.76 ± 0.4 nm (labeled with green arrow), and this value is only 10% smaller than the same measurement way in the case of DBBA precursors inside the molecular island, which is 0.8 nm (detail can be found in Figure 2.4). Furthermore, the latter distance along the protrusions in the row is 1.0 nm, which agrees perfect with the

value of DBBA inside the molecular island. Constant current STS show the same shape of HOMO resonance of DBBA molecule before illumination (Figure 2.4 d)). A small shift of the HOMO resonance might be ascribed to the surrounding which is different than that in the ordered islands. One of the possibilities to explain these observations is that the laser induced bond cleavage between Br atoms and anthracene units, but also between the bonds of anthracenes. The decomposed molecules give rise to the disordered structures.

Comparing measurement results between the 1st and 2nd preparations, lower photon dose in the 2nd preparation is not enough due to existence of the intact DBBA molecules. More energy need to be put into the sample, therefore, we have performed the 3rd preparation with the highest photon dose comparing to the first two preparations. An STM overview is obtained from the sample of the 3rd preparation which owns the highest photon dose in the three preparations, shown in Figure 2.18. An island can be clearly observed with ordered lower parts and a disordered overlayer. Figure 2.18 b) shows an image of a larger island consisting of four rows of uniform height. It consists of parallel structures of length 2.0 nm. The angle between these rod like features and the Au(111) soliton lines is approximately 85°.

With the STM tip, lateral manipulation on this rod like island has been performed. Figure 2.18 b) and d) are the STM images during the STM tip pulling process. We could see that the single unit can be laterally dragged out of the row without destroying the ordered island or itself. This reflects the non-covalent interaction between the rod like structures, as well as the weak interaction between this unit and gold substrate. Figure 2.18 h) shows a high-resolution STM image of this rod like unit. The intensity distribution of it is relatively homogeneous, with the intensity maximum along the long axis of this unit.Comparing the apparent height with that of DBBA inside the molecular island and an individual DBBA molecule lying on the surface, we find that the laser induced structure is flatter than the other two on the surface, which is only approximately 1.5 Å, shown in Figure 2.18 c). The length of this rod like structure is nearly 2.0 nm which is about two times of the length (0.93 nm) of the anthracene units of DBBA molecules. The measured lateral distance between neighbouring rod like structures is equal to 5 Å. This value coincides very well with the reported value of the internal distance of the self-assembly tetradecane molecular island on Au(111) [140]. This value is also reported in the other observations of tetradecane and some other alkane molecules self-assembling on Au(111) [141–144]. Therefore, we superimpose the tetradecane molecular model on the laser induced unit, seen in Figure 2.18 h). We ascribed the formation of tetradecane molecules to the laser influence on the DBBA precursor molecules. The energy provided by laser cleave the bonds in the anthracene unit of DBBA molecules, like opening a zipper, leading to the generation of tetradecane molecules. The number of carbon atoms in a single anthracene unit is in a good agreement with that in the tetradecane molecule, which is 14 carbon atoms.

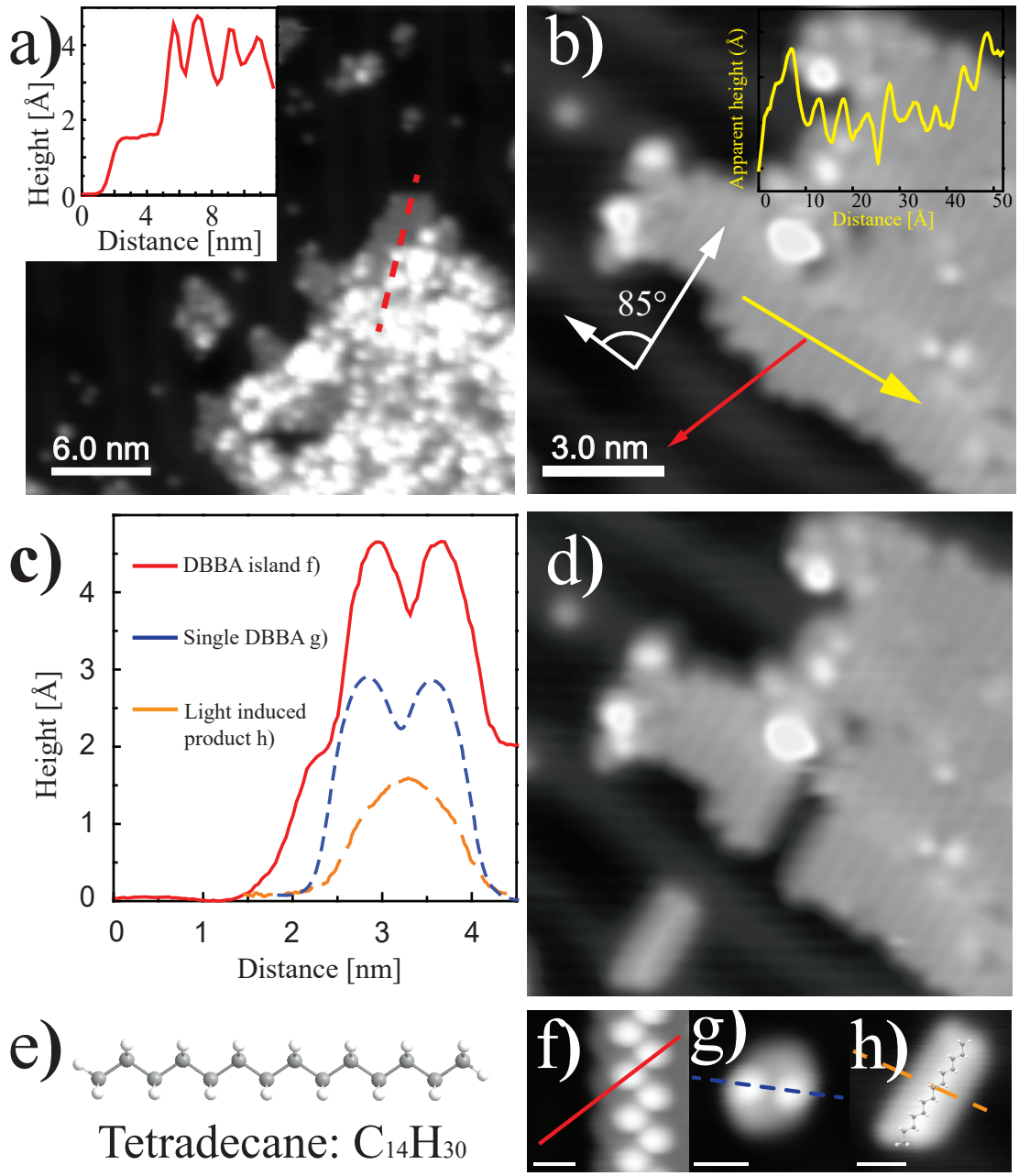

Figure 2.18: STM experiments on the photo-product of DBBA on Au(111). **a)** STM overview image of illuminating DBBA molecular island on Au(111) by laser for one hour. ($V = 0.76$ V, $I = 18$ pA) **b)** Ordered structure observed after illumination. The red arrow indicates the tip-induced manipulation. The angle between the soliton line of Au(111) and the long axis direction of the rod like structure is highlighted, which is approximately 85°. Line profile perpendicular to the parallel structures is shown in the inset image. ($V = 1.9$ V, $I = 19$ pA) **c)** Line profiles of the edge of a DBBA island **f)**, an isolated DBBA molecule **g)** and the isolated laser induced unit **h)**. **d)** After lateral manipulation by STM tip compared to **b)**. ($V = 2.0$V, $I = 140$ pA) **e)** Model of tetradecane molecule. **f)**, **g)** and **h)** are DBBA molecular island, single DBBA molecule and laser induced unit, respectively. The scale bar represents 1 nm. Tetradecane molecular model has been superimposed on the image of **f)**.

2.6 Conclusions

In this chapter, we investigated the structural and electronic properties of DBBA molecules on Au(111). DBBA molecules adsorb on the gold surface in a 3D configuration due to the steric hindrance of the hydrogen atoms between the two anthracene units. The molecular islands are stabilized by $\pi\cdots\pi$ interaction between the anthracene units of the adjacent DBBA molecules. Using lateral manipulation we could drag single DBBA molecule out of the molecular island while keeping the molecule intact. This suggests the non-covalent interaction between DBBA precursor molecules inside the island.

Annealing the DBBA/Au(111) sample under different temperatures could lead to various phases. Under the low annealing temperature of 100 °C, DBBA molecules tend to form two phases through halogen bonds without detaching the Br atoms. When annealing up to 200 °C, Br atoms dissociate from the anthracene units, and the radicals start the Ullmann reactions, coupling to each other through covalent bonds. The new generated polymer chains own high flexibility on the gold surface. By further annealing the polymer chains, the 7-AGNR can be obtained. GNR weakly interact with the gold surface underneath and keeps the typical Tamm state at the two terminals of the ribbon.

The experiment of illuminating the pulsed laser upon the DBBA/Au(111) has also been performed. Interestingly, the laser induced C-C bond cleavage and reconnection have been observed. Especially, the laser induced tetradecane molecular island has been observed.

3 Structural and Electronic Properties of Ferrocene-Carboxylic Acid Molecules on Metal Surfaces

In order to implement graphene for potential application in electronic devices for the future, more and more focus was put onto the graphene growth with controllable diameter and shape such as GNR [14], equiangular hexagonal graphene island [145] and triangular graphene [15]. These fabrication methods could properly avoid the generation of various defects during the preparation process. Among these investigation, fabricating triangle shaped graphene flakes on Cu(111) [15] is paid much attention, not only because of its bottom-up fabrication method and feasible reaction conditions, but also due to its precursor molecules, which is called 1,1-ferrocenedicarboxylic acid (FcAd), provide a new concept for the researchers to synthesize graphene with ferrocene-based molecules on metal surfaces.

3.1 Metallocene and Metallocene Derivatives

Metallocenes were discovered in the 1950s and, to a great extent, have accelerated the development of organometallic chemistry. Fischer and Wilkinson were rewarded the Nobel Prize in chemistry in 1973 thanks to their tremendous contribution on the investigation of organometallic system, which is also known as sandwich compounds. This special structure can be also defined as double-decker configuration with two cyclopentadienyl rings (C_5H_5-Cp) connected by a transition metal atom in the center (M). For example, the nickel atom in the middle of two Cp rings lead to nickelocene molecules, the iron atom in the middle of two Cp rings lead to ferrocene molecules and so on.

Ferrocene molecules, as it is well known, are easily to be obtained as three-dimensional metalorganic molecule with the zero-spin ground state [146, 147]. It is also a promising building block for applications oriented to spintronics and hetero nanojunctions. For example, the property that ferrocene molecule by accepting single electron could make it a promising substitution for building blocks of molecular quantum cellular automata, in which a couple of ferrocene molecules could be regarded as a couple of quantum wells for a charge moving between them [147–151].

There are two preferential configurations of ferrocene molecules, which are called eclipsed conformation and staggered conformation, respectively (Figure 3.1 b)) [152]. It is reported that the stability of the two dimensional structure depends crucially on the combination of vertical and horizontal molecules having their Cp rings in the eclipsed configuration (D_{5h} symmetry, seen in the upper image of Figure 3.1 b). In the bulk structures, the presence of the vertical and horizontal orientations ensures the cohesion of the crystal through T-shaped interactions, and the staggered configuration (D_{5d} symmetry), unlike in the two dimensional structure, is favored over the eclipsed configuration in the crystal.

The adsorption and desorption of ferrocene molecules on the different surfaces with various surface index have been widely investigated under UHV conditions in the past decades, such as on Au(111) [153], Ag(100) [154–156], Cu(100) [154], and graphite [157], claiming that the molecular axis of the ferrocene molecules, which is represented as Cp-M-Cp (M is metal for short), is either perpendicular or parallel to the substrate surfaces depending on the substrate material and its orientation, shown in Figure 3.1 a). However, the knowledge of interaction mechanism between ferrocene molecules and metal substrates, especially

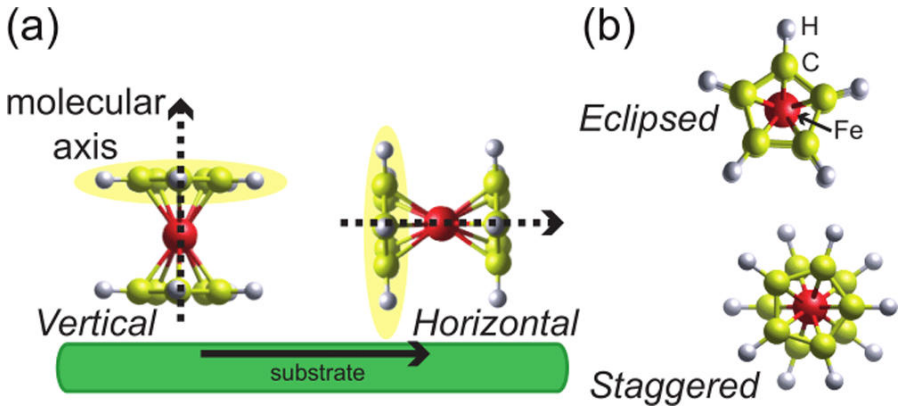

Figure 3.1: a) Vertical and horizontal adsorptions of ferrocence molecules on the Cu(111) substrate. The dashed line with arrow indicate the axis of the molecules. White, yellow, and red balls represent H, C, and Fe atoms, respectively. **b)** Eclipsed and staggered conformations of a ferrocene molecule (images adapted from Ref. [152]).

the interplay between ferrocene derivatives and metal surfaces, is still limited. Numerous past researches have proved that the self assembly molecules can be strongly influenced by functional groups which adjust the binding behaviour of molecules [158–163]. Among these modified binding behaviours, hydrogen bond O$\cdots$HO, with bonding angle of 180° between two carboxylic groups (COOH), is one of many strong bindings which can be regarded as powerful non-covalent connectors for supramolecular networks on the substrate surface [162, 164].

Therefore, by considering the involvement of the multi-functional groups, COOH groups in our case, of the ferrocene molecules, there would be more possibilities for this molecule to show various adsorption behaviours and orientations on the different metal surfaces. Therefore, it is very interesting to investigate the properties of FcAd molecule on different substrates, such as Cu(111) and Ag(111). Experimental results and further analysis will be introduced in the following.

3.1.1 Bulk Crystal Structure of FcAd Acid Molecule

Before introducing the specific adsorption behaviours and properties of FcAd molecules on metal surfaces, it is necessary to have a general idea of its structures in the bulk crystal. Former work indicated that FcAd dimers are the main building blocks of the FcAd bulk crystal, in which both carboxylic acid groups of every single FcAd molecule form double hydrogen bonds with the ones of the paired molecule, leading to a four-hydrogen-bond dimer [165–171]. Among the bulk crystal structure studies, the distance between the iron atoms, or the distance between the cyclopentadiene centroids, of a dimer pair is reported as 9.1 Å.

3.1.2 DFT Calculation of FcAd Acid Molecule

Figure 3.2 illustrates the DFT calculation result of gas phase FcAd molecule with two carboxylic groups pointing to the same directions (named Configuration1). It is notable that the HOMO of FcAd molecule, which is shown in Figure 3.2 a), localizes in the ferrocene body part. On th contrary, the LUMO of the FcAd molecule is more distributed over the

carboxylic groups and comparably less over the ferrocene part. Furthermore, it can be clearly seen that the FcAd molecule in the bulk is in the staggered configuration instead of the eclipsed configuration. Our calculation result is different from the ones published before, in which the different theoretical approaches have been carried out to calculate the most stable configuration for ferrocene molecules, but leading to that the two Cp-rings are parallel to each other and oriented in the same direction, in another word, in the eclipsed configuration [152, 172, 173]. Therefore, we could here preliminary propose that the incorporation of carboxylic groups into ferrocene molecules changes the interaction mechanism inside the ferrocene base.

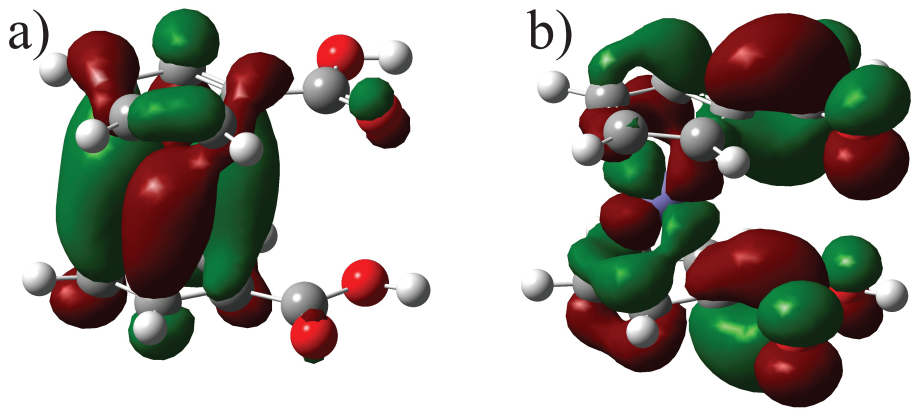

Figure 3.2: Gas phase DFT calculation result of FcAd molecule with carboxylic groups pointing to the same direction. **a)** HOMO of FcAd gas phase. **b)** LUMO of FcAd gas phase.

DFT calculation has also been carried out in the configuration of FcAd molecules with two carboxylic groups pointing to the opposite directions (named Configuration2). Figure 3.3 shows the orbital distribution of FcAd molecule in the gas phase. In the case of HOMO, the orbital mainly localized in the FcAd body part, which means localizing in the ferrocene base, regardless of HOMO or HOMO-1, shown in Figure 3.3 a), b), c) and d), respectively. Therefore, from the top and side view, the orbital distribution of HOMO and HOMO-1 can be simply regarded as a cylinder shape. On the contrary, in the case of unoccupied states, the orbital distributed in the whole molecule inhomogeneously. In detail, it can be observed that more molecular orbital localized in the two carboxylic group moieties from the side view of the molecular LUMO model, shown in Figure 3.3 g). From the top view, the shape of LUMO can be simply seen as an elongated ellipse, which is similar to the calculation result of LUMO+1. However, in the case of LUMO+1, the molecular orbital only distributes in the two cyclopentanecarboxylic moieties instead of the iron center, seen in Figure 3.3 d) and h). By comparing the HOMO and LUMO between Configuration1 and Configuration2, we find that the orientation of carboxylic groups of an FcAd molecule does not dramatically influence the orbital distribution.

3.2 Self-assembly of FcAd molecules on Ag(111)

In the past years, more and more studies on the adsorption behaviours of metallocene and its derivatives have been performed on various metal surfaces [147, 152, 153, 164, 165, 174]. Especially, a recent publication with the result of X-ray photoelectron spectroscopy (XPS) measurement about FcAd molecule on Ag(111) proposed a model of FcAd adsorbing on Ag(111) [175]. In this work, they compared the interface between FcAd molecules on

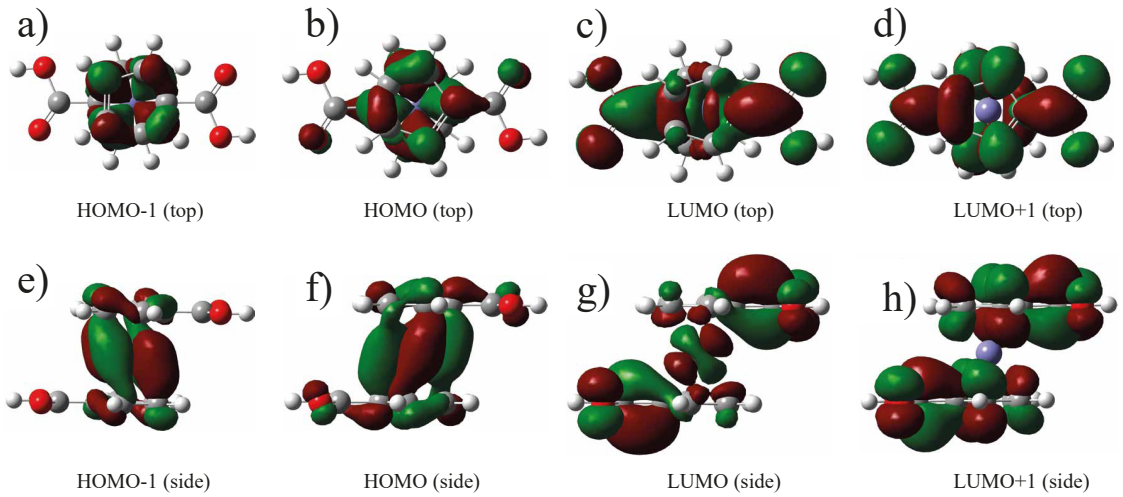

Figure 3.3: DFT calculation of the FcAd gas phase with two carboxylic groups pointing to the opposite directions. **a)** Top view of HOMO-1 of FcAd gas phase. **b)** Top view of HOMO of FcAd gas phase. **c)** Top view of LUMO of FcAd gas phase. **d)** Top view of LUMO+1 of FcAd gas phase. **e)** Side view of HOMO-1 of FcAd gas phase. **f)** Side view of HOMO of FcAd gas phase. **g)** Side view of LUMO of FcAd gas phase. **h)** Side view of LUMO+1 of FcAd gas phase.

Ag(111), on Cu(110), and on Cu_3N/Cu(110) through monitoring the O 1*s* core level line shape in the XPS spectra, since single carboxylic group owns two nonequivalent oxygen atoms, belonging to carbonyl (CO) and hydroxyl (OH), respectively. However, in the both cases of FcAd molecules on Cu(110) and on Cu_3N/Cu(110), only single O 1*s* resonance can be observed in the XPS spectra, indicating that the dehydrogenation process has taken place in both cases and the chemical bond between COO^- with copper substrate has formed. On the contrary, in the case of FcAd on Ag(111), they observed that there is an unambiguous dip in the middle of a broad resonance in the XPS spectrum, which can be fitted into two sharp resonances with same intensities, referring to the equal number of hydroxyl and carbonyl groups, indicating the existence of intact COOH group (seen in Figure 3.4 a)). In the measurement of near edge X-ray absorption fine structure (NEXAFS) result, it shows that a prominent set of π resonances in the grazing incidence geometry and a strong σ signature in the normal incidence geometry. Since the FcAd molecules own the cyclopentadienyl rings, they attribute these features to a prevailing orientation of the rings parallel to the substrate. In other words, with the measurement results of XPS and NEXAFS, they prove that, besides the lying-flat configuration on Ag(111), the FcAd molecules also exhibit an upstanding configuration on Ag(111) (details can be seen in Figure 3.4 b)).

In addition, the STM measurement with functionalized tip is an efficient method to obtain better resolution of the topography, especially the molecular shape and adsorption behaviour on metal surfaces. Previous investigations on metallocene molecules have shown that, bright round protrusions or donut-like structures under STM measurement tend to be the pentagon rings of metallocene molecules, and the rod-like structures between these features are ascribed to the metallocene molecules lying on the surface with the molecular axis paralleling to the surface [152, 175–177] (details can be seen in Figure 3.5 a)-d)).

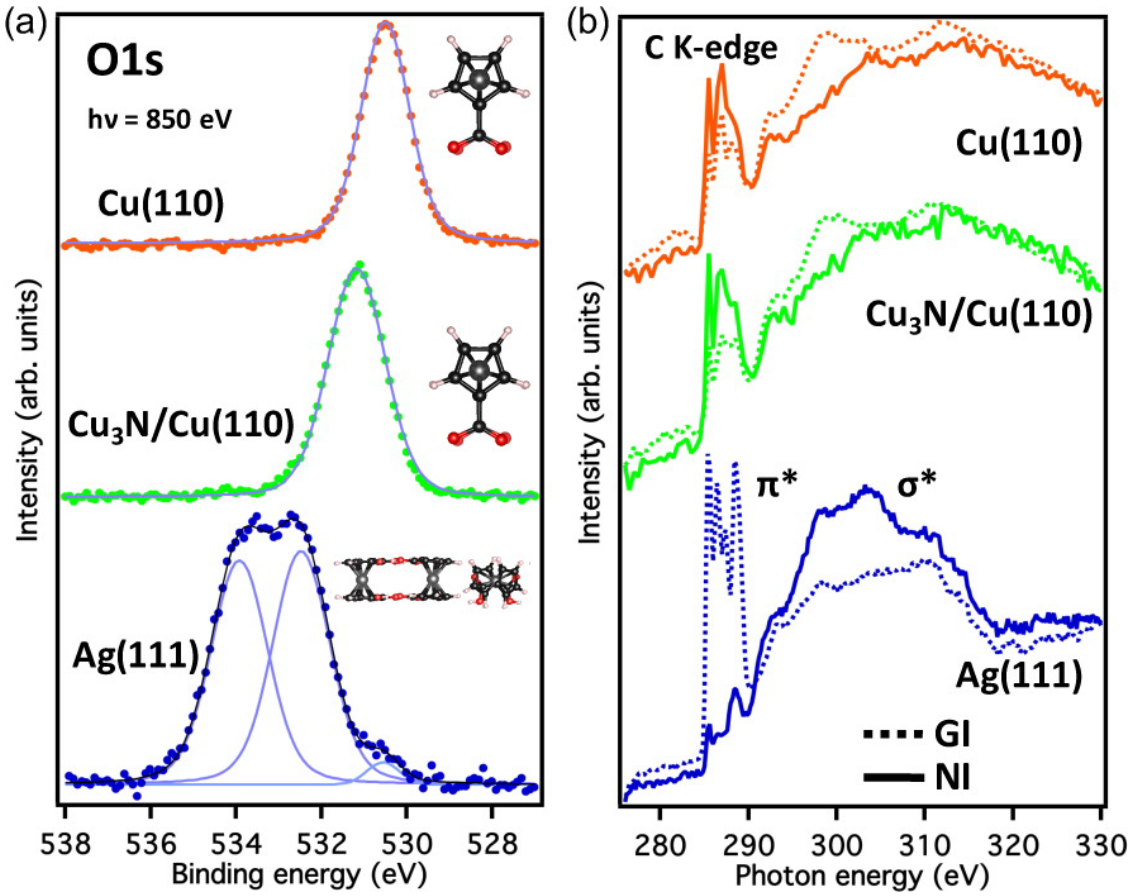

Figure 3.4: XPS and NEXAFS measurement results of FcAd on Cu(110), Cu_3N/Cu(110) and Ag(111) substrate, respectively. Two images are cited from [175]. **a)** XPS spectra of O 1s of FcAd molecule on different substrates adsorbed on different substrates (dotted graphs are experimental spectra and the solid lines are fitted line.). The inset models schematically indicate the positions of the molecules with respect to the substrate surface. **b)** NEXAFS spectra of the C K-edge corresponding to the samples with the spectra in a). The solid lines represent normal incidence (NI) and dotted lines the grazing incidence (GI) geometries.

3.2.1 Adsorption Structure of FcAd Molecules on Ag(111)

Here, we investigated the adsorption behaviour of FcAd molecules on Ag(111) with STM. Submonolayer FcAd molecules were deposited onto the Ag(111) through molecule evaporation. From the overview image in Figure 3.6 a), ordered molecular island was firstly observed after the molecules deposition. The molecular island consists of uniform bright round protrusions. After further zooming into the island, every two protrusions form a dimer-like structure (hereafter referred to as dimer), which, instead of existing individually, also forms the rows leading to the molecular island in the end. By considering the model shape and the geometric structure of FcAd molecules, the vertical FcAd molecular model has been preliminarily superimposed onto the zoom-in image of FcAd island, shown in Figure 3.6 c). Through the enlarged area obtained from the large molecular island, we can clearly observe the bright round protrusions, which represent the upper pentagon rings of FcAd molecules, are forming dimer rows, shown between the yellow dashed lines in Figure 3.6 c). However, the bright protrusions are not centrosymmetric in the STM image. The similar asymmetric feature has also been observed in the FcAd

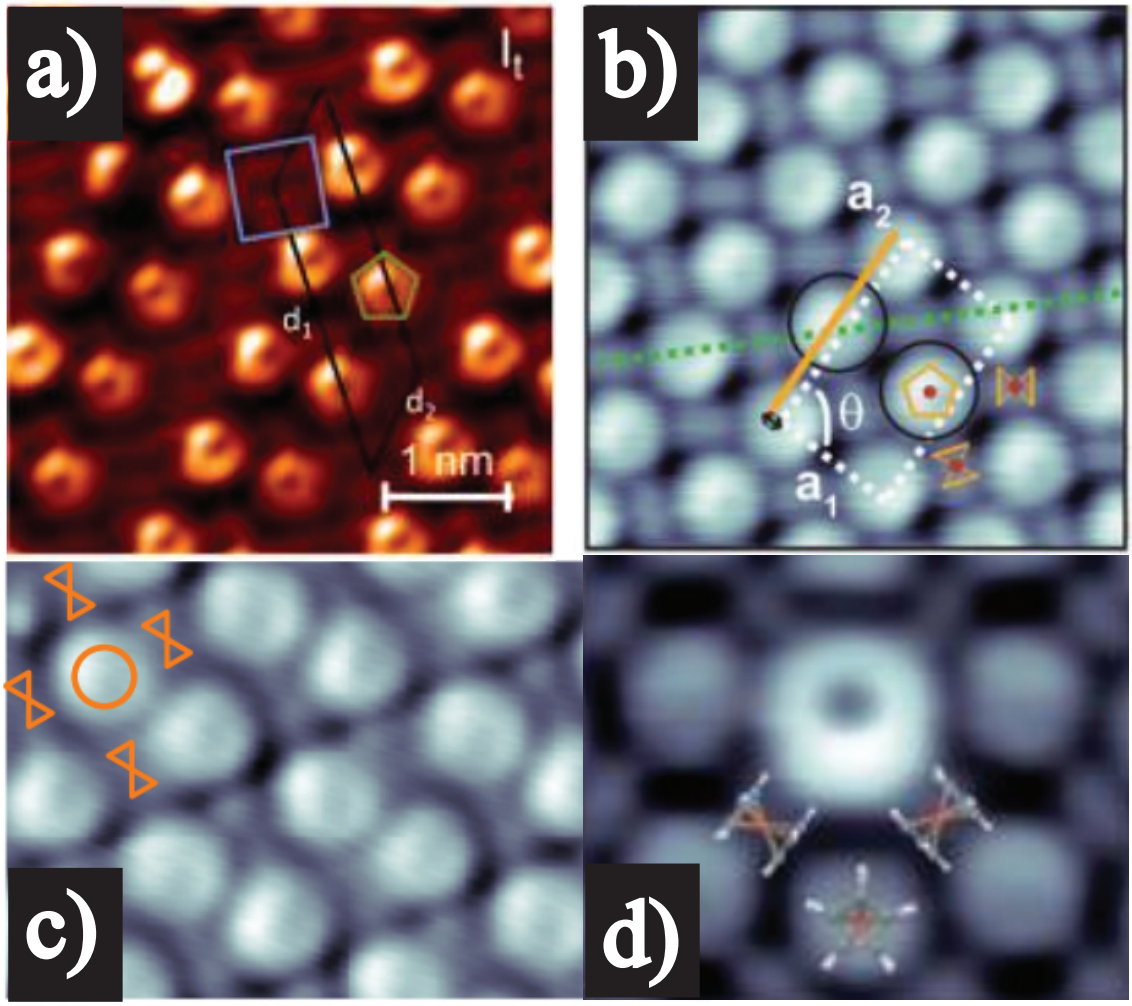

Figure 3.5: STM images of metallocene and derivaties on metal surfaces. **a)** FcAd on Ag(111), image adapted from Ref. [152]. **b)** Ferrocene on Cu(111), image adapted from Ref. [175]. **c)** Nickelocene on Cu(100), image adapted from Ref. [176]. **d)** Ferrocene on Cu(111), image adapted from Ref. [177].

DFT calculation result of LUMO, where the molecular orbitals mainly distribute in the cyclopentanecarboxylic moiety, seen in Figure 3.2. Therefore, we ascribe the asymmetric appearance to the cyclopentanecarboxylic moiety of the upstanding FcAd molecules on the silver substrate. Line profile has been measured along two directions in the Figure 3.6 a) and result was shown in Figure 3.6 b). The upstanding dimers exhibit an apparent height of 2.7 Årespect to the surface. This value is also close to the DFT calculation result of the height of FcAd gas phase model, which is 3.2 ± 0.1 Å. Moreover, this measurement result also agrees well with the experiment results of other metallocene molecules on metal substrates [152, 153, 174, 175]. The slight height difference between the measurement result and model height can be ascribed to the better conductivity of the metal substrate. Line profiles have been measured along two different directions across the FcAd island, labeled by red and green lines with arrows respectively, seen in Figure 3.6 a) and b). The width of the dimer is d = 1.2 ± 0.01 nm, and width of two molecules from the neighbouring rows is D = 1.4 ± 0.01 nm, respectively. The peak-peak distance along carboxylic interaction

axis of FcAd is 10.0 Å, which agrees with the value derived from the bulk crystal structure very well, which is 9.1 Å [152].

If we assume all the FcAd molecules are standing upright on Ag(111), it is hardly to explain the formation of the molecular island since the hydrogen atoms of the dimers would be electrostatically repulsive to each other. Furthermore, the previous research results have evidently shown that, dehydrogenation process is widely known to happen for carboxylic acids being deposited onto the various metal surfaces [178–188]. In the dehydrogenation process, the hydrogen(H) atoms of carboxylic groups would detach from the molecules, leading to the chemical reaction of COO^- interacting with the metal substrate. Considering the effect that dehydrogenation process would bring as well as the formation of dimer island of FcAd molecules, the molecular model lying on the substrate, which means the axis of FcAd molecule is parallel to the surface needs to be taken into account (shown in Figure 3.6 c)). Our proposed molecular model of FcAd on Ag(111) is also in a good agreement with the intermolecular arrangement of the ferrocene molecules, in which horizontal and vertical molecules are simultaneously present in the molecular island [152, 164, 189]. Due to the two carboxylic groups pointing to the opposite directions towards the flanking vertical FcAd molecules, the horizontal FcAd molecules could play a role as a bridge vising the vertical FcAd molecules belonging to different dimer rows, so that the FcAd molecular island can be formed. There are a total of three molecules, horizontal and vertical, per unit cell. The packing density is 0.025 molecules / $Å^2$ of FcAd on Ag(111), and this value is agreed well with that of the ferrocene molecules on Cu(111) and Cu(100), which is 0.03 molecules / $Å^2$ [152, 176].

The STM measurement with a functionalized tip is a common method to obtain better resolution of the topography. In our measurement, we have unintentionally obtained a few images with functionalized tip, seen in Figure 3.7. In both a) and b), we could clearly observe the previous mentioned bright round protrusions showing a donut-like shape, which has been ascribed to the cyclopentane ring of FcAd. Every two round protrusions form a FcAd dimer also seen in Figure 3.6 c). Previously, we claimed that we could not measure the area between the dimer rows due to the limitation of bare STM tip, however, with this functionalized tip, we are able to evidently see that there is a rod-like structure filling up the area between the adjacent dimer rows. This finding coincides very well with a few other published work about the STM measurement of metallocene molecules on various metal surfaces [152, 164, 189].

Although the proposed unit cell of vertical FcAd dimer and horizontal FcAd monomer coincides quite well with our measurement results and others publication, the adsorption behaviour of the carboxylic groups in the lower pentagon of vertical FcAd molecules is not clear due to the limitation of STM tip measurement. However, the ordered molecular island, to some extent, could express that the arrangement in the lower decker of FcAd molecules, which is also in a regular configuration. In the lower decker inside the dimer, we propose that the hydroxy of one side FcAd molecule could form the hydrogen bond with the oxydren atom of the other side of FcAd molecule. This configuration will further help the formation and the stability of the molecular island. Further evidence needs the DFT calculation combining FcAd molecules with Ag(111).

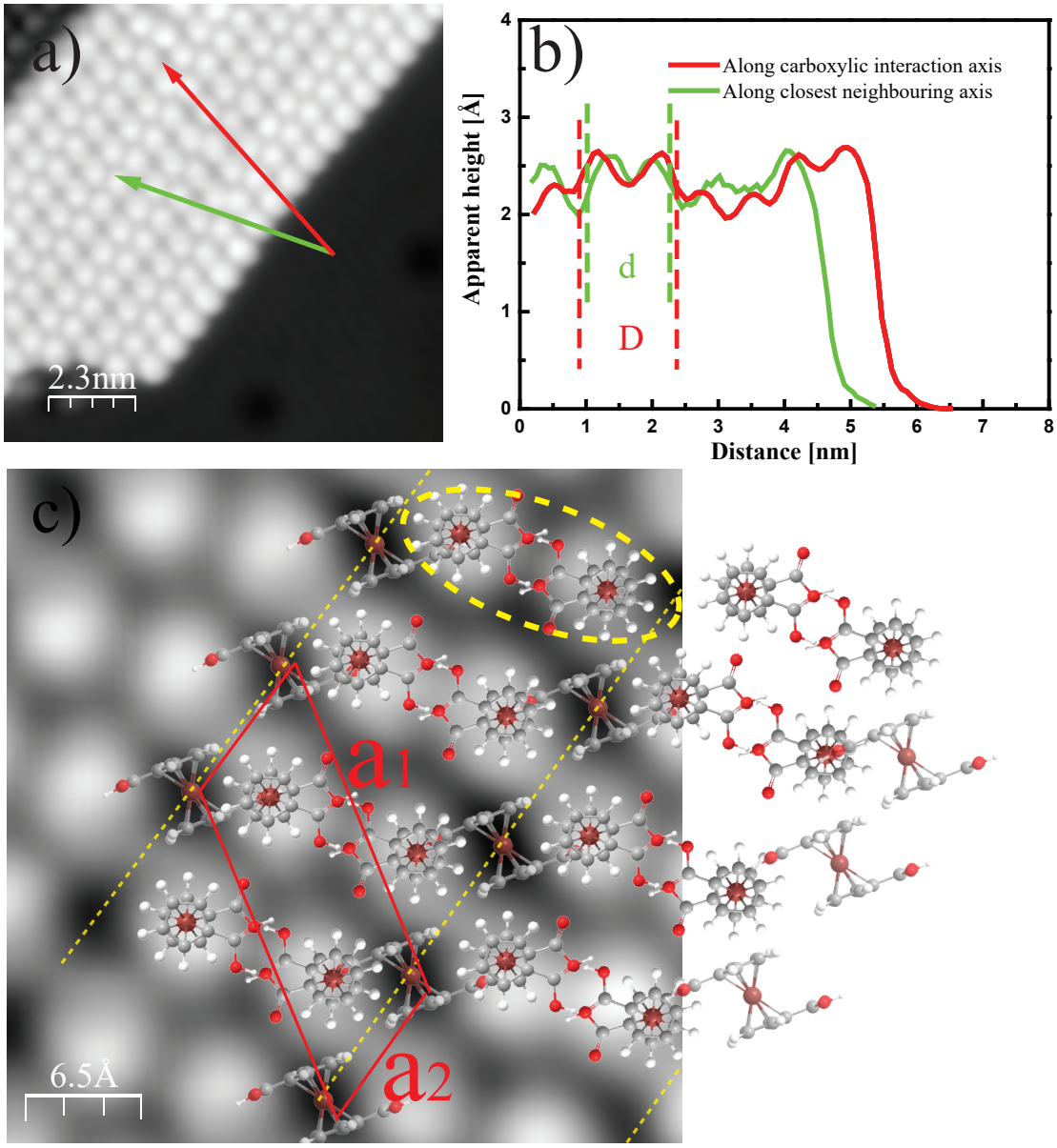

Figure 3.6: STM topography of FcAd on Ag(111). **a)** Overview image of FcAd molecular island on Ag(111) ($V = 0.5$ V, $I_k = 0.1$ nA). **b)** Line profile on the FcAd island along carboxylic interaction axis and closed neighbouring axis, respectively in image a). The width of the dimer is d $= 1.2 \pm 0.01$ nm labeled with green colour, and width of two molecules from the neighbouring rows is D $= 1.4 \pm 0.01$ nm labeled with red colour. **c)** a Zoom-in topography of FcAd island on Ag(111) ($V = 0.5$ V, $I = 0.1$ nA). The area between two yellow dotted lines marks the FcAd dimer rows. FcAd molecular models have been superimposed on the STM image. The red, gray, dark red and white balls in the molecular model represent oxygen (O), carbon (C), iron (Fe) and hydrogen (H) atoms, respectively. The bright protrusions represent the upstanding FcAd molecule on Ag(111) and the dark area between the dimer row, FcAd molecules are lying on the silver surface, connecting the upstanding FcAd molecules to form the molecular island. The red rhomboid area is the unit cell of FcAd molecular island. The angle between a_1 and a_2 is 58°/122°, respectively.

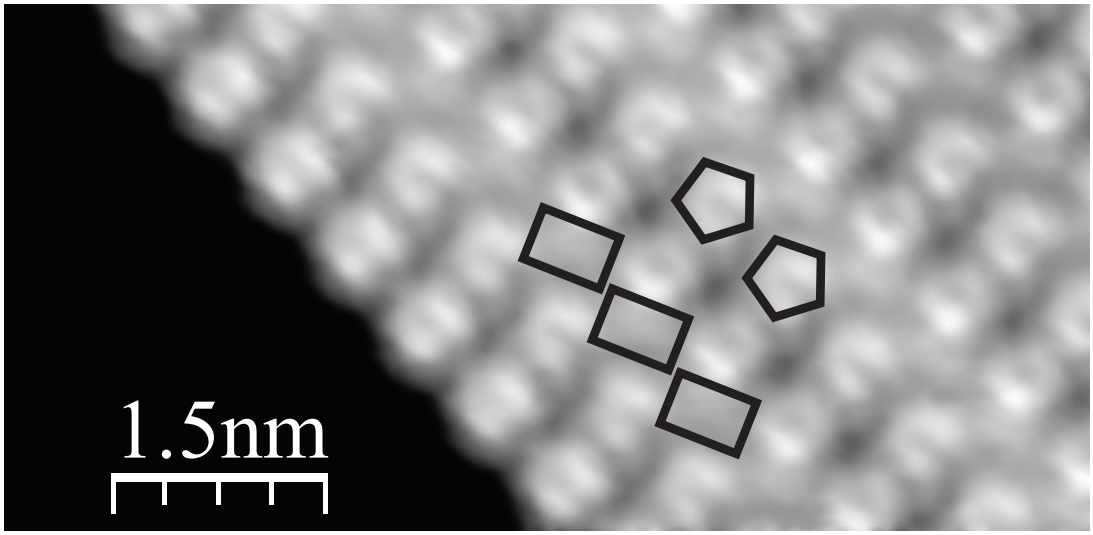

Figure 3.7: STM images of FcAd molecular island on Ag(111) with unclear functionalized tip. The regular pentagon represents the Cp ring of vertical FcAd molecules. The rectangles highlight horizontal FcAd molecules. The image is taken under U = 0.5 V, I = 0.5 nA.

3.2.2 Electronic Properties of FcAd Molecules on Ag(111)

In order to investigate the molecule-substrate interaction and the electronic properties of FcAd molecules on Ag(111), constant height STS measurements have been performed on the vertical FcAd molecules (Figure 3.8). In the constant height dI/dV spectra shown in Figure 3.8 b), we compared the graphs obtained from clean Ag(111) surface with the one on the vertical FcAd molecule. Firstly, almost the same sharp onsets and shape can be seen in both graphs. From the black graph showing the energy of 70 meV below the Fermi level, which is the typical surface state of Ag(111) [190–192], we could deduce that the STM tip and local Ag(111) surface is not contaminated by other atoms/molecules. In the purple curve obtained from the measurement on the bright round protrusion, we observe that the nearly exact same shape of the black graph, but shifting to the high energy up to 110 meV above the Fermi level. This phenomenon could directly reflect the weak interaction between the vertical FcAd molecule and silver substrate.

From the dozens of STM images we have taken in the large area, there is no FcAd molecular island forming in the terrace area, but growing from the step edges. This observation could well indicate that the diffusion barrier is rather low for the FcAd molecules on Ag(111), comparing to the intermolecular interaction. Therefore, we believe that the driven force leading the formation of FcAd molecular island on Ag(111) can be ascribed to the hydrogen bonds. Recent calculation result from Berger Jan *et al.* has expressed that the hydrogen bond between the opposite carboxylic groups is the strongest [175]. Interaction of molecules with the substrate is a bit weaker. Their DFT calculations also revealed that there is only negligible charge transfer between FcAd molecules and Ag substrate. This further confirms that the interaction between FcAd molecules and Ag(111) should be vdW interaction instead of chemical bonding, which means the molecules are physisorbed on the metal surface. Similar observation on the shift of surface state has been published with other molecules on the various substrates [193–196]. In our experiment, the Ag(111) Shockley surface state is not disrupted by the adsorbed submonolayer of FcAd molecules. There is only a small energy shift across the Fermi level can be observed by STS measurement.

Since charge transfer is not triggered at the molecule/metal interface leading to the surface state depopulation, thus we can ascribe the shift of surface state to the modification of the image potential by deposited FcAd molecular island above the silver substrate.

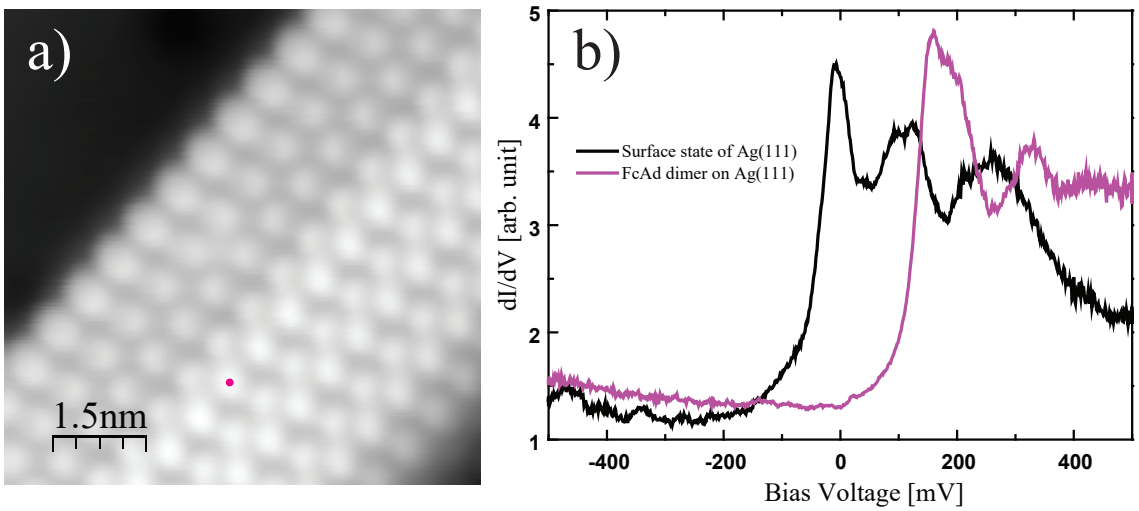

Figure 3.8: Shift of surface state of FcAd on Ag(111). **a)** FcAd molecular island on Ag(111) (V = 0.5 V, I = 0.1 nA). **b)** Shift of Ag(111) surface state. The black graph was obtained from the clean Ag(111) close to the molecular island. The purple graph was measured on the vertical FcAd molecujjile in the molecular island.

Constant current STS measurements have also been performed on the FcAd molecules on Ag(111), at negative and positive bias range respectively, seen in Figure 3.9. From the Figure 3.9 a) and b), we observed that on the clean Ag(111), there is no resonance by sweeping the bias up to -2.5 V. On the contrary, there is a small resonance starting from -2.0 V and reaching to the maximum at -2.2 V when measuring on the vertical FcAd molecules. We ascribed this resonance to the HOMO of the FcAd molecules on Ag(111). Similar measurement has been conducted at the positive bias, and the results can be seen in Figure 3.9 c) and d). There is an obvious resonance at 2.2 V, which cannot be observed on the clean silver substrate. We attribute this resonance to the LUMO of FcAd molecules on Ag(111). Therefore, we obtain the HOMO-LUMO gap of FcAd molecules on Ag(111) which is about 4.4 V. It is notable that, when sweeping the bias at the positive range up to 2.5 V, the unstability of FcAd molecules can be observed from the spectrum. The inset image of Figure 3.9 c) is the image taken after the constant current STS measurement. The FcAd molecular island has become locally disordered because of the excessive bias voltage upon. This observation further indicates the physisorption behaviours of vertical FcAd molecules on Ag(111).

3.3 Self-assembly of FcAd Molecules and Thermal Products on Cu(111)

Self-assembled metallocene molecules tend to show two adsorption behaviours on the same substrate, horizontally and vertically, respectively. However, the metallocene molecular acids dramatically change their interaction mechanism with the surfaces due to the presence of single or multiple carboxylic groups, such as the observation of recent published paper [164]. According to the previous studies in the past decades, organic molecules with carboxylic groups are always apt to self-assemble through hydrogen bonding or metal-

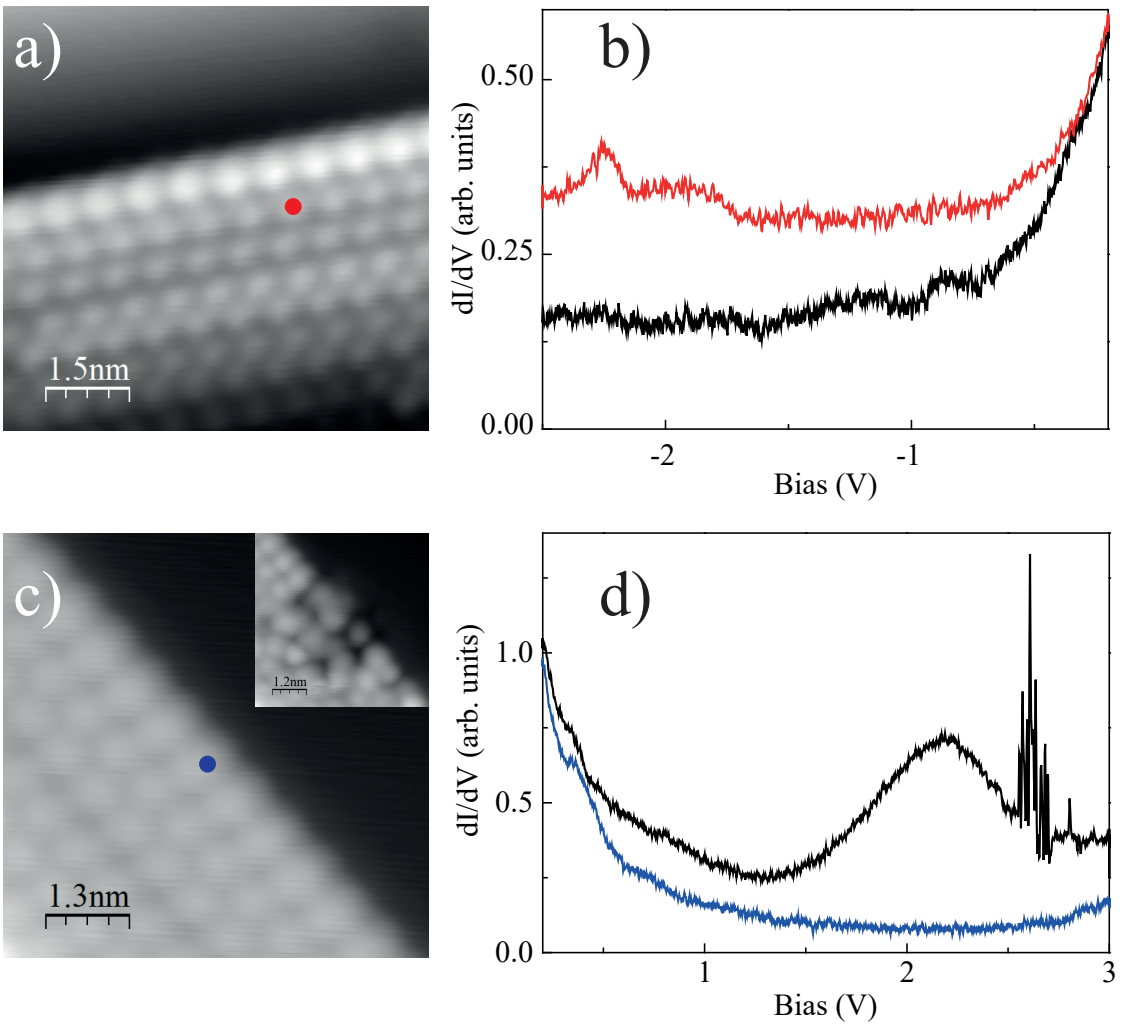

Figure 3.9: HOMO and LUMO measurement of FcAd on Ag(111) **a)** FcAd molecular island on Ag(111) ($V = 0.5$ V, $I = 0.1$ nA). The red dot highlights the STS measurement position. **b)** Constant current STS measurement at negative bias on clean Ag(111) and vertical FcAd molecules. **c)**FcAd molecular island on Ag(111). ($V = 0.2$ V, $I = 50$ pA). The blue dot represents the STS measurement position. The inset image is taken after the constant current STS measurement. **d)** Constant current STS measurement at positive bias on clean Ag(111) and vertical FcAd molecules.

organic ligands, and preferably form into flat-lying two-dimensional structures on substrates [178, 186, 197–203]. However, only a few studies have focused on the vertical adsorption configuration of acid molecules with single or multiple carboxylic groups on the sample surface [204–207]. Furthermore, there is limited investigation of molecular carboxylic groups vertically bonding to the copper surface [208–215]. Although there are quite a few similar properties between Cu(111) and Ag(111) substrates, we cannot indiscriminately transfer the model of adsorption behaviour of FcAd molecules on Ag(111) to the case of FcAd on Cu(111). The weaker coordination bond between carboxylic groups and Ag compared to Cu leads to a very different balance between molecule-substrate and intermolecular interactions [179, 188, 207, 216–222].

3.3.1 Structural Properties of FcAd Molecules on Cu(111)

The structural properties of FcAd molecules have been studied by evaporating FcAd molecules onto clean Cu(111) substrate in STM system. Depositing FcAd molecules onto Cu(111) surface results in self-assembled monomer islands with bright protrusions, which can be seen in Figure 3.10 a). The long-range well-ordered molecular submonolayers consist of large number of uniformed molecules with limited defects, which is different from the result published in ref. [15]. They claimed that the FcAd molecules could not form submonolayer on Cu(111). It is notable that there are some bright protrusions forming the bright rows, and between these bright rows, there are four to five protrusions as an interval. In the upper right of Figure 3.10 a), a bright row exhibits a dislocation phenomenon. We ascribe this observation to the limited defects inside the molecular island.

Line profile measurement has been conducted on the FcAd molecular island. The apparent height of FcAd molecular island on Cu(111) is only about 2.5 Å, shown in Figure 3.10 b). The COOH groups of the FcAd molecules tend to chemically react with copper surface through dehydrogenation process [152]. Therefore, we could preliminarily propose that, on the Cu(111) substrate, FcAd molecules tend to form the molecular island with Cp-Fe-Cp axis paralleling to the copper sample surface through the coordination bonding.

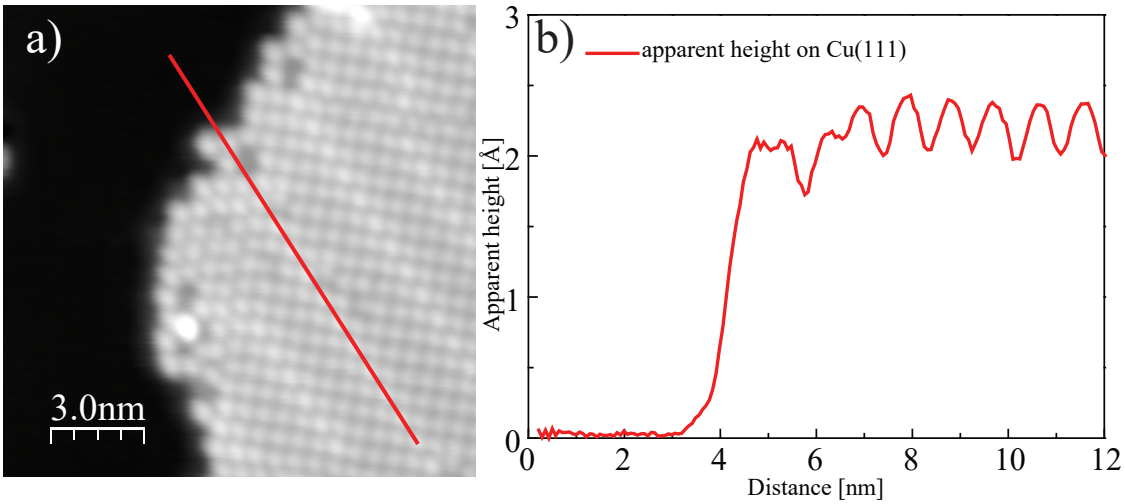

Figure 3.10: STM topography of self assembled FcAd molecular island on Cu(111). **a)** STM topography of FcAd monomer island on Cu(111). (V = 0.5 V, I = 0.3 nA). **b)** Line profile of FcAd molecular island on Cu(111).

In the experiment of FcAd molecules on Cu(111), we also obtained the STM images acquired in the same area with both bare STM tip and functionalized STM tip, seen in Figure 3.11 a) and b). From these two zoom-in STM images, we could observe that the FcAd molecules form the molecular island consisting of alternately dim and bright protrusions with the same intermolecular intervals. However, in the image of Figure 3.11 a), the protrusions are ellipse like feature while in the Figure 3.11 b), they emerge as a weaving shuttle shape. Hence, the observation in Figure 3.11 b) is derived from the functionalized STM tip since the measurement parameters are same comparing that in Figure 3.11 a). In the Figure 3.11a), the ellipse shape of protrusions looks in a good agreement with the DFT calculation result of the LUMO with the top view, seen in Figure 3.3 c), in which the molecular orbitals mainly distribute in the cyclopentanecarboxylic moiety. In the Figure 3.11b), the ellipse shape is better depicted due to the functionalized tip. The unit cell is marked in Figure 3.11 b) with red square area and labeled with a_1 and a_2 which both equal 8.4 Å. This equilibrium can also reflects that, for each FcAd molecule inside the molecular island, its nearest neighbouring molecules have the same center-center distance to it. It can be calculated that the packing density is 0.028 molecules / Å^2 for FcAd molecules on Cu(111), which is also in a good agreement with the packing density of FcAd molecules on Ag(111) of 0.025 molecules / Å^2 introduced in the last subchapter. Further studying the STM image acquired with functionalized STM tip, we find that FcAd molecules aligned like a windmill structure with four blades. Each of the blades represents an ellipse protrusion in Figure 3.11 a). Each blade is perpendicular to the four surrounded ones, pointing to the center of the neighbouring molecule through T-shaped interaction.

In the past years, it has been widely reported that organic molecules with carboxylic acid end groups tend to get deprotonated upon deposition on copper substrate [179–181, 188, 207, 223–225]. Thereinto the coordination between carboxylic groups with the copper adatoms through deprotonation process has been published [179]. In the recent work, FcAd molecules have been proved to interact with Cu(110) and Cu_3N/Cu(110) surface through the coordination bond between COO^- with Cu atom. We also notice that noncovalent interactions determining the molecular stability have been investigated elsewhere, such as CH$\cdots\pi$, NH$\cdots\pi$ and cation$\cdots\pi$ interactions [226–232]. Therefore, it is highly possible that the FcAd molecules interact with Cu(111) through the COOH groups and copper atoms of the surface. This means the carboxylic groups of FcAd molecules point to the copper surface, leaving the Cp-Fe-Cp axis parallel to the surface. The geometry also coincides well with the line profile measurement result of the self-assembly STM image in Figure 3.10 a) and b). The hydrogen atoms of the cyclopentadiene ring form the hydrogen bonding through CH$\cdots\pi$ interaction with the cyclopentadiene ring of the neighbouring molecules, leading to the T-shaped orientation of FcAd molecules on Cu(111).

Therefore, the FcAd molecular models can be superimposed according to the discussion above, shown in the right bottom part of Figure 3.11 b). To be specific, the carboxylic groups of FcAd molecules point to the copper substrate, forming the coordination bond between COO^- with Cu atoms. It can be determined that CH$\cdots\pi$ interaction is the driving force leading to the formation of FcAd molecular island on Cu(111). Similar arrangement has recently been published in the cobaltocene crystal structure [233]. Line profile measurement has been performed on the FcAd molecular island on Cu(111), seen in Figure 3.10 b). The lateral distance between two bright protrusions can be read out from Figure 3.10 c), which is 3.1 ± 0.5 nm. This value is exactly 12 times of the lattice constant of Cu(111), which is 2.56 Å. This multiple relationship suggests that the brighter FcAd molecules inside the self-assembly molecular island on Cu(111) adsorbed in a periodic configuration.

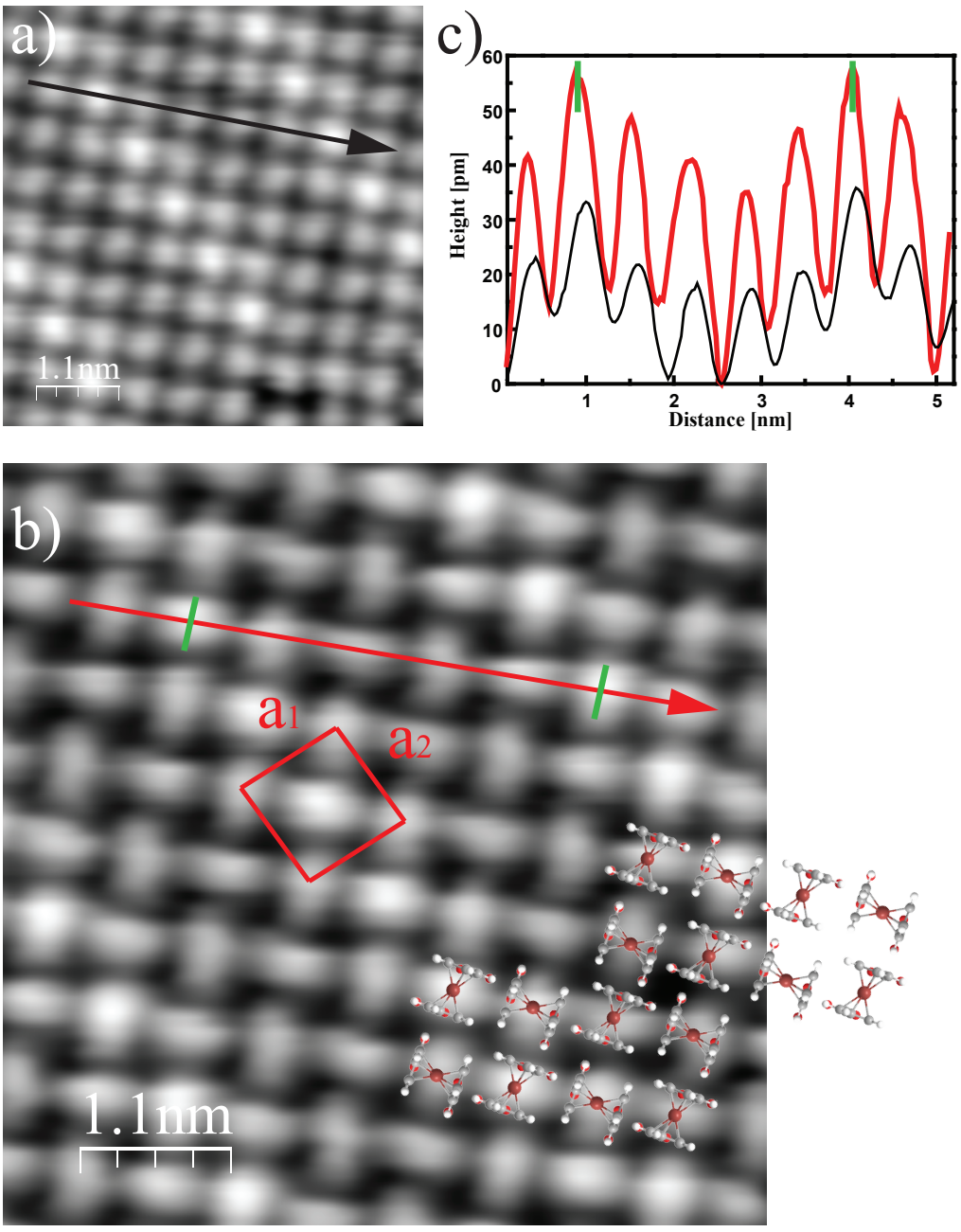

Figure 3.11: Zoom-in STM images of FcAd molecular island on Cu(111). **a)** Zoom-in STM image of FcAd molecular island on Cu(111) with bare STM tip. **b)** Zoom-in STM image of FcAd molecular island on Cu(111) with functionalized STM tip. The rectangular area represents the unit cell of self-assembled FcAd molecules on Cu(111) with a_1 and a_2 vectors. The superimposed FcAd molecular model is scaled according to the size of the STM image. **c)** Apparent height along the two arrows shown in **a)** and **b)** The distance between the two vertical green lines show the maximal height with lateral distance equals 3.1 $\pm$ 0.5 nm. The two STM images are taken under $V = 0.2$ V, $I = 0.3$ nA.

By utilizing the STM tip with bias voltage pulse to manipulate the molecules has been conducted elsewhere [234–236], and molecular manipulation has been realized with STM tip in rotating C_{60} experiment [237]. In our experiment, we have also conducted an STM experiment by applying bias voltage pulses to the bright FcAd molecules on Cu(111). To be more specific, the bias voltage pulses with certain time length have been applied to the center of the birght FcAd molecule. STM images of before and after applying the voltage pulses can be seen in Figure 3.12 a) and b). By applying a voltage pulse of 1.0 V with 50 seconds upon FcAd molecule, the molecule evidently changed its appearance from bright protrusion in Figure 3.12 a) to the dimmer protrusion in Figure 3.12 b). At the same time the neighbouring FcAd molecule, which shows dimmer appearance before applying the voltage pulse, turned into the bright protrusion instead. This means that, by applying the voltage pulse, the two FcAd molecules next to each other switched the adsorption configuration. The exchange in the apparent height in both molecules can be read out in Figure 3.12 d) and the value turned out to be the same. Similar phenomenon has been observed in a molecular motor [238]. They reported that through the tunneling electrons from the STM tip into the ferrocene moiety of a large molecule with five arms and three legs, the anticlockwise rotation of the molecular arms can be realized. Hence, in our case, we propose to ascribe the change in the molecular appearance to the slight shift off the adsorption site of the horizontal FcAd molecule. To be specific, voltage pulse induced inelastic tunneling electrons force the brighter FcAd molecules slightly off the ontop adsorption sites, simultaneously, the adjacent dimmer molecule changes its adsorption behaviour to adopt the stress coming from the neighbouring molecule.

3.3.2 Electronic Properties of FcAd Molecules on Cu(111)

The electronic properties of FcAd on Cu(111) has been investigated by measuring constant current STS. Figure 3.14 shows the constant current STS of FcAd on Cu(111), both of which have been compared with the results of clean Cu(111) surface. Figure 3.14 a) clearly shows two resonances in the unoccupied states of FcAd on Cu(111), which cannot be observed on the clean Cu(111). The two resonances are locating at 1.7 V and 2.35 V, respectively, which we ascribe to LUMO and LUMO + 1 of FcAd molecules on Cu(111). On the other hand, in the negative voltage range, by sweeping the bias upon the FcAd molecules on Cu(111) as well as upon the clean Cu(111), we could firstly observe the sharp onset in the black graph, which represents the surface state of Cu(111) and also expresses no other molecules/atoms influencing our STM tip. Two sharp resonances located at -1.8 V and -2.2 V can be found in the graph obtained on the FcAd on Cu(111), which are supposed to be HOMO and HOMO-1, respectively. Therefore, the HOMO-LUMO gap of FcAd molecules on Cu(111) can be derived as 3.5 V. This value is much smaller than the HOMO-LUMO gap of FcAd molecules adsorbing on Ag(111), which is 4.4 V (-2.2 V of HOMO and 2.2 V of LUMO). Note that the HOMO and LUMO of FcAd on Cu(111) shift close to the E_F from both sides comparing to that of FcAd on Ag(111). This reflects that FcAd molecules more strongly hybridize with Cu(111) than Ag(111). This is also well support the fact that FcAd weakly physisorbed on Ag(111). The charge transfer between FcAd molecules and Cu(111) can be preliminarily assumed.

Constant height $\mathrm{d}I/\mathrm{d}V$ spectra have also been measured on the FcAd molecules on Cu(111), seen in Figure 3.15. The black curve in Figure 3.15 b) represents the result obtained from the area without molecular coverage in Figure 3.15 a). The small kink at -0.44 V indicates that the surface state of Cu(111) is intact. However, the surface state cannot be observed in the curve obtained from FcAd on Cu(111). This phenomenon clearly reflects that the

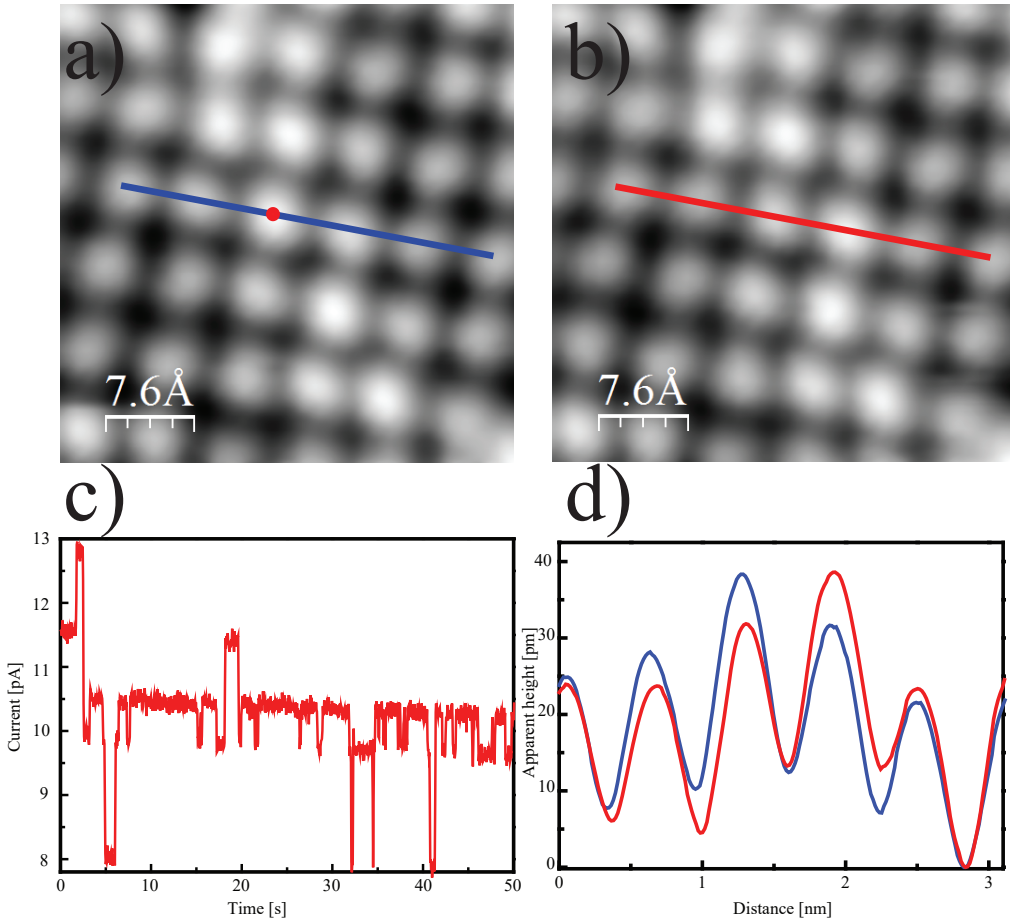

Figure 3.12: Bias voltage pulse applied on the FcAd molecules on Cu(111). **a)** and **b)** STM images before and after the bias voltage pulse application with 2.0 V. The impacted molecule has been highlighted with the red dot. Both STM images of this figure are taken under $V = 1.0$ V, $I = 0.1$ nA). **c)** The graph of tunneling current against time with 50 seconds. **d)** Apparent height comparisons before/after the voltage pulse.

strong hybridization between the FcAd molecules and Cu(111). The surface state has been depopulated by the charge transfer process at the molecule/metal interface. This also coincides well with the downshift of LUMO of FcAd molecules on Cu(111), seen in Figure 3.14 b).

3.4 Thermal Products of FcAd Molecules on Cu(111)

In the past years, fabrication of graphene has been widely achieved on solid surface. The epitaxial growth of graphene on SiC wafer has been reported by annealing the wafer at 1200 °C [239]. By thermal decomposition of hydrocarbon, graphene has been successfully grown on Ru(1000) [240]. Graphene quantum dots with regular sizes and films have also been realized on metal surfaces by thermal decomposition of fullerene molecules [241, 242]. Although many methods of growing graphene by thermal treatment have achieved, direct growth of graphene with controllable shape and edges has been fulfilled with limited success. In the following part, we introduce a method by thermal decomposition of FcAd

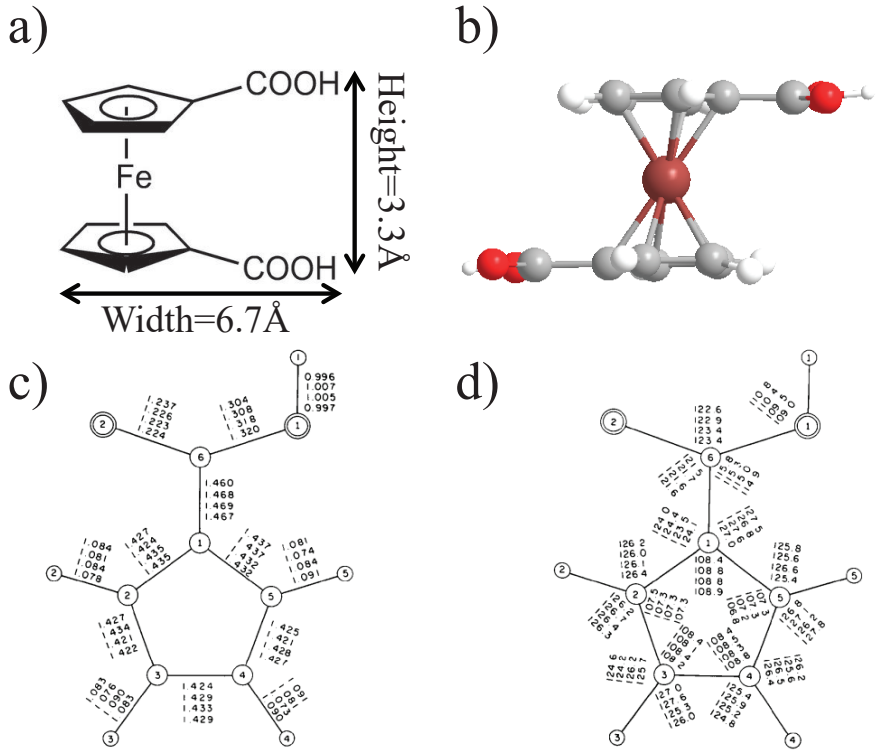

Figure 3.13: Sketch of FcAd molecules and parameters. **a)** Size of FcAd model with two carboxylic groups pointing to the same direction. The distance between two Cp rings is 3.3 Å and the width of FcAd molecule is 6.7 Å. **b)** Sketch of FcAd molecular model with two carboxylic groups pointing to the opposite directions. **c)** Bond distances (Å) in the cyclopentanecarboxylic moiety. **d)** Bond angles (°) in the carboxylcyclopentadienyl moiety. The images of **c)** and **d)** are cited from ref. [170]

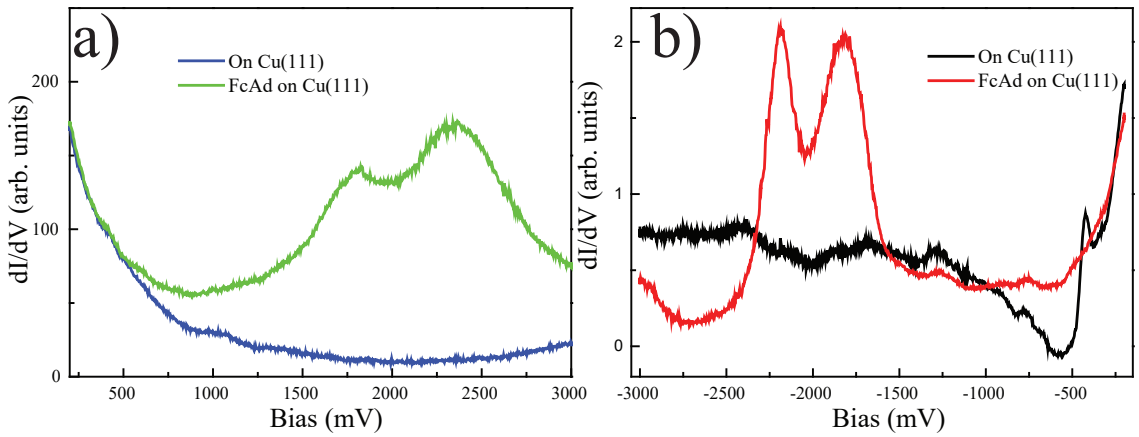

Figure 3.14: Constant current dI/dV spectra of FcAd on Cu(111). **a)** Constant current spectra in positive range (I = 50 pA). **b)** Constant current spectra in negative range (I = 50 pA).

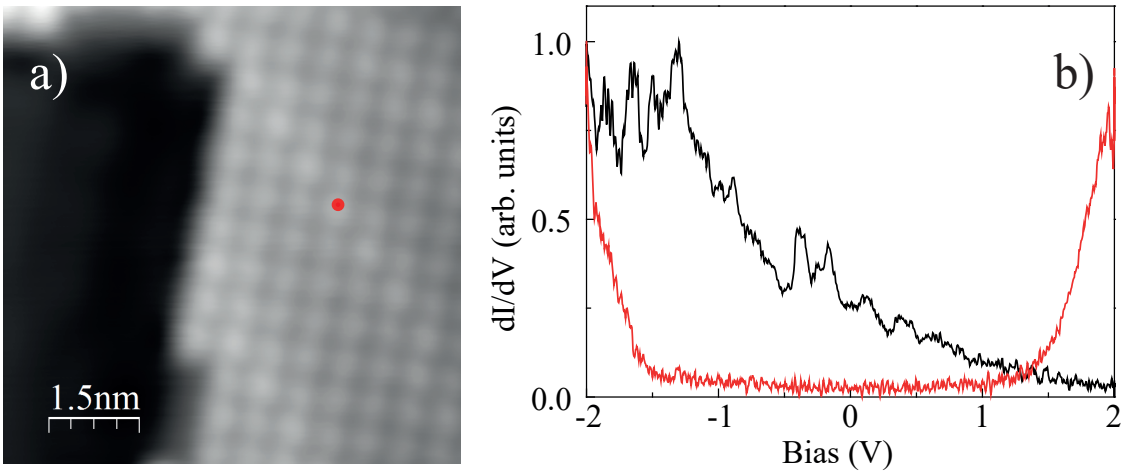

Figure 3.15: Constant height dI/dV spectra of FcAd on Cu(111). **a)** The STM overview image of FcAd molecular island on Cu(111) (V = 0.2 V, I = 0.5 nA). The red dot highlighted the measurement position. **b)** Constant height spectra on the clean Cu(111) and the FcAd molecule. (feedback opened at 50 pA and -2.0 V).

acid molecules on Cu(111) in an ultrahigh vacuum chamber.

Figure 3.16 shows an overview image of the heating products obtained from FcAd molecules under 300 °C annealing temperature, in which annealing products demonstrate dramatic differences from the ordered FcAd molecules self-assembled on Cu(111). In the overview image, we could directly observe that the copper surface is nearly completely covered by the annealing products without any ordered structures. We find the triangular shape of molecular patches growing from the step edges. The side length of this triangle patch is approximately 12 ± 2 Å . Former publication have reported that after annealing the FcAd molecules on Cu(111) up to 573 K, triangular graphene patches can be obtained on the copper substrate surface [15]. Therefore, the triangular shape island obtained in our experiment can be ascribed to graphene patches as well.

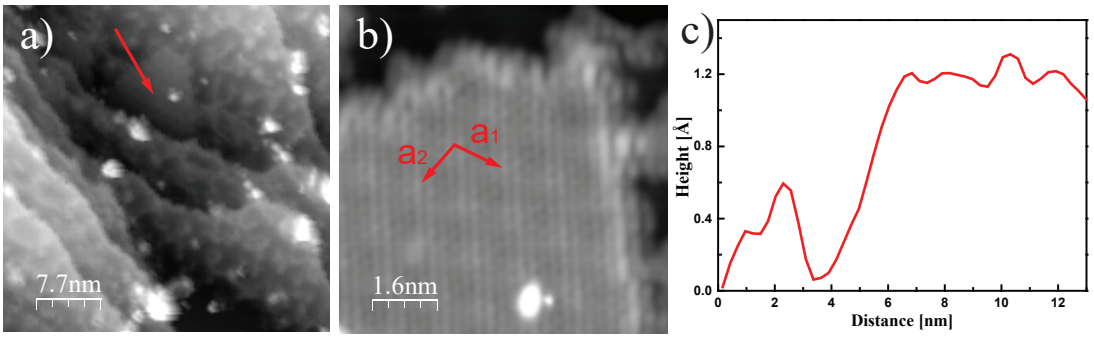

Figure 3.16: Annealing products of FcAd on Cu(111) under 573 K. **a)** Overview STM image of annealing products of FcAd on Cu(111) (V = 1 V, I = 56 pA). **b)** Zoom-in image of triangle island in a). Basic vectors a_1 and a_2 are labeled with red arrows with angle equals 120 °. **c)** Line profile of triangle graphene on Cu(111).

Figure 3.16 b) is the zoom-in image of the triangle graphene observed in Figure 3.16 a). The island appears as an equilateral triangle shape with unordered structures, which are

the reaction derivatives, decorating the three edges. These thermal induced derivatives hinder the growth of triangular island so that the length of a triangle side shows no more than 15 nm in all the scanning areas in our experiment.

Inside the island, there are periodic bright protrusions can be clearly observed. Close examination with measuring the basic vectors, shown in Figure 3.16 b) as a_1 and a_2, demonstrate that two basic vectors equal 1.2 nm with the included angle 120 °. The similar superstructure with the Moiré patterns has been reported on graphene grown on other metal surfaces [243]. According to the result of line profile measured in Figure 3.16 a) and shown in Figure 3.16 c), the apparent height of patches on Cu(111) is 1.1 ± 0.1 Å depending on the bias voltage applied to take the image, and this value also coincides very well with large area graphene on Cu(111) [244]. We could infer that this kind of triangle island consists of single atomic layer. Therefore, the presences of Moiré patterns and single atomic layer unambiguously confirm that the one-layer graphene with a triangle shape is formed on the copper surface by annealing FcAd molecules on Cu(111). Although the mechanism of the formation of this triangular shape of graphene patches is not clear at this experimental stage, it is highly possible that the cyclopentanecarboxylic moiety of FcAd molecules undergoes a 5-carbon ring open and re-form the benzene ring with the 6th carbon atom obtained from the carboxylic group of the cyclopentanecarboxylic moiety. Cu(111) substrate plays a crucial role as a catalyst during this process.

Furthermore, we find it interesting to mention that, in the published work, before the annealing treatment, the amount of evaporated FcAd molecules has been measured and reached up to 1.1 monolayer [15], nevertheless, according to the measurement in our preparation, we only prepared about one third monolayer FcAd molecules covered on the copper surface. However, the amount and size of triangular graphene patches derived from heating are basically equal in both experiments, seen in Figure 3.17. The possibility of this intriguing phenomenon is either due to the quality differences of the sample crystals in these two experiments, which likely play a very important role as a catalyst during the heating process, or the triangular graphene patches are not the main chemical reaction products in this thermal experiment. The experiment with the same amount of the FcAd molecules has also been conducted on Ag(111) under the identical annealing temperature, which is 300 °C. However, the graphene patches or other shape of graphene island cannot be observed, shown in Figure 3.17 d). We conclude that different substrates can dramatically influence the thermal products due to their distinct chemical reactivities.

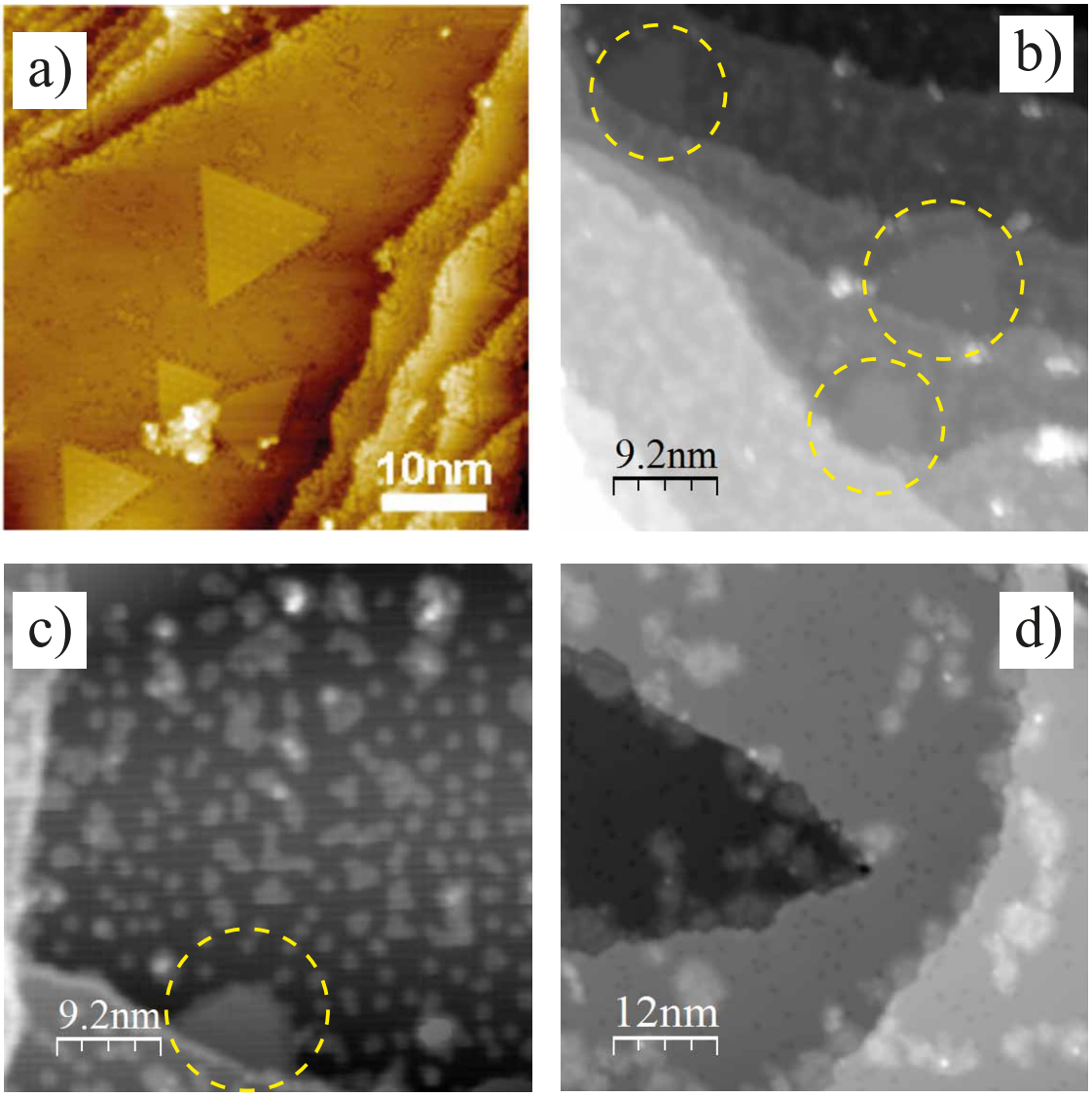

Figure 3.17: Annealing products of FcAd on metal surfaces. **a)** An overview STM image of annealing products of FcAd on Cu(111) (V = -2.5 V, I = 0.07 nA). The image is cited from Ref. [15]. **b)** and **c)** Overview STM images of annealing products of FcAd on Cu(111). The triangular graphene patches have been highlighted by yellow dotted circle. (images taken under V = 1.0 V, I = 10 pA and V = 1.3 V, I = 0.1 nA, respectively). **d)** Overview STM images of annealing products of FcAd on Ag(111). (V = 1 V, I = 22 pA).

3.5 Conclusions

In this chapter, we investigate the structural and electrical properties of FcAd molecules on Ag(111) and Cu(111) surface by STM method. FcAd molecules self-assemble into condensed molecular islands on both substrates.

On the Ag(111), FcAd molecules form dimer island through hydrogen bonds provided by COOH groups of FcAd molecules. There are two adsorption configurations of FcAd molecules on Ag(111), vertically and horizontally, respectively. The horizontal FcAd molecules play a role binding the two adjacent FcAd dimers. These two adsorption configurations have also been observed with the STM functionalized tip. The weak interaction between FcAd molecules and Ag(111) can be further proved by STS measurements. The intact but upshift of Ag(111) surface state obtained by measuring the constant height STS on FcAd molecular island indicate the modification of the image potential by depositing FcAd molecular island.

On the Cu(111), FcAd molecules could also form molecular island, however, only the horizontal adsorption behaviour can be deduced on Cu(111). The formation of the FcAd molecular island is driven by the force of $CH\cdots\pi$ interaction. The bias voltage pulse could change the local adsorption site of FcAd molecule inside the molecular island. The heating treatment upon FcAd/Cu(111) sample could lead to the small size of triangular graphene patches on Cu(111). However, the large scale of graphene island or graphene sheet cannot be observed on Cu(111) due to the large number of unordered thermal induced derivatives on the surface, which hinder the growth of graphene island. We propose that the formation of graphene patches is likely obtained from the process of 5-carbon ring opening and re-bonding to the 6th carbon atom of COOH group of the same cyclopentanecarboxylic moiety. Similar experiment has been performed on Ag(111) by annealing the FcAd/Ag(111) sample, however, the thermal induced triangular graphene patches were not observed on Ag(111) due to the different catalytic activities comparing to the Cu(111) substrate.

4 Electron- and Heat-Induced Ethylene Decomposition on Au(111)

Although graphene is valuable for research purposes, the methodologies to fabricate large amount of graphene to meet the requirement from the industrial applications are insufficient. One interesting method attempted to fabricate graphene is the reduction of graphene oxide flakes, however, the mobility of the charge carriers has been unavoidably reduced [245]. The graphitization of silicon carbide substrates has been realized, but leaving the problem of the detachment from the SiC substrate [246, 247]. Therefore, many efforts have been put onto developing new methods of obtaining graphene on metal surfaces, such as the growth on polycrystalline films of Ni, Co, and Cu-Ni alloy [248], dissolving carbon atoms in a transition metal melt [249], growth on Ru and Pt [250]. The most commonly conducted technique is thermal decomposition of hydrocarbons catalyzed via its adsorption on the surface of the metal by means of chemical vapor deposition (CVD) [251–253]. However, because of the catalytic role of the metal surface, CVD could fail with some low reactivity metals where the hydrocarbons are hardly adsorbed. Au is a rather inert substrate compared to Pt, Ir, where the growth of graphene is a well established reaction. Some experiments have shown that growth of graphene by this method is also possible on Au(111) [254], but requires high temperature of $\sim$ 1000 K. The aim of this chapter is to establish a similar growth mode in our lab. Therefore, we constructed an oven for heating up the Au(111) substrate. The preparation temperature displayed from the thermocouple has been simultaneously calibrated by a pyrometer. The thermal products have also been analyzed and discussed.

4.1 Experimental Reaction Conditions

In the sample preparation process, we followed the method reported in Ref. [254]. The fragments of ethylene molecules are generated from the electron bombardment of the ion beam, which is the same one used to clean the sample as a sputter gun. The preparation chamber is filled with ethylene gas at high pressures ranging from 10^{-6} mbar to 10^{-5} mbar in two different preparations. Higher ethylene pressure has been tested and would have highly influenced the emission current of our home-built oven and hindered the temperature increment of the sample. The ethylene gas in the preparation chamber is in the floating status with the support of turbo pump. The current of accelerated ions is around 20 mA. During the 30 min of irradiation, the ethylene molecules are ionized by electron impact and accelerated against the high temperature gold surface. The ion beam is composed of $C_2H_4{}^+$ ions, as well as some smaller ions such as $C_2H_3{}^+$, $C_2H_2{}^+$ and $CH_4{}^+$ [255]. As soon as the ions reach the substrate surface, they are supposed to be neutralized or dissociated into small fragments or even implanted in the first subsurface layers [254]. Therefore, post annealing at higher temperatures after the irradiation has been performed. The post annealing temperature is about 100 °C higher than the sample temperature (T_s) in the preparation and last for 10 minutes.

The Au(111) sample, in the electron-bombardment process, was kept being heated with the emission current provided by a home-built oven with a high voltage (HV) controller. T_s is measured and monitored with the *K*-type thermocouple wire connected to the sample. The properties of thermocouple wire may change with use and time (especially when used at elevated temperatures) resulting in measurement drift and a thermocouple probe might be

$I_{filaments}$	$U_{filaments}$	$I_{emission}$	$U_{external}$	T_{sample} (thermal couple)	T_{sample} (pyrometer)
5.2 A	7.2 V	6.0 mA	1.5 kV	403 ℃	448 ℃
5.4 A	7.5 V	8.0 mA	1.5 kV	464 ℃	482 ℃
5.5 A	7.7 V	11.0 mA	2.0 kV	521 ℃	527 ℃
5.5 A	7.7 V	13.0 mA	2.0 kV	627 ℃	620 ℃
5.6 A	8.0 V	16.7 mA	2.0 kV	726 ℃	708 ℃
5.6 A	8.2 V	20.0 mA	2.0 kV	782 ℃	760 ℃

Table 4.1: Pyrometer calibration with the thermocouple connected to the sample. The filaments belong to the oven and has been applied to negative HV, and sample is grounded above the oven which will generate the emission current to locally heat up the sample. The emission current has been monitored during the heating process.

mechanically damaged in service [256]. Therefore, we have used a pyrometer to monitor the T_s by setting focus on the area close to the center of substrate surface. The pyrometer has been calibrated by simultaneous measurement with K-type thermocouple, and calibration details can be seen in the Table 4.1.

4.2 Reaction Products

We have conducted two experiments with different ethylene gas pressure during the preparation, 8.2×10^{-6} mbar $\sim 1.0 \times 10^{-5}$ mbar and $1.0 \sim 2.0 \times 10^{-5}$ mbar, respectively. The latter pressure is roughly doubled compared to the former one. The ethylene gas is bombarded while the T_{pyro} is 776 ± 3 °C for 30 minutes. Post-annealing has also been conducted at 870 ± 3 °C for 10 minutes in both experiments.

Preparation with lower ethylene pressure

Figure 4.1 shows the STM overview image acquired over an area of 121 nm × 121 nm. The image exhibits a couple of island-like structures growing from the step edges of gold surface. It is noticeable that some islands grow across the step edges which have been highlighted by the orange dotted lines shown in the topography of Figure 4.1 a). The scale of the islands range from $\sim$ 100 nm^2 to $\sim$ 500 nm^2 by rough calculation through Figure 4.1 a) and b). Noted that the islands tend to grow across the step edges when they started at the area with multiple step edges.

Zoom-in image has been taken over an island growing from the straight step edge, shown in Figure 4.1 c) and d). The unperturbed pattern of the herringbone reconstruction of Au(111) can be observed through the island structure. This indicates a weak interaction between the substrate and the adsorbed layer. Figure 4.1 d) is the contrast enhancement result of image c), to underline the soliton line positions that being highlighted with yellow dotted lines over the hcp region.

The apparent height of graphene nano flakes/dots grown by an intercalation-based all-

epitaxial method has been reported to be 2.4 ± 0.1 Å [257], which is well in line with our measurement results which is 2.3 ± 0.1 Å, shown in Figrue 4.1 e). We have also found that the apparent height of the island shown in Figrue 4.1 c) is independent of voltage bias ranging from -0.2 V to 1.0 V, which can be seen in Figrue 4.1 f). However, both of the values are much lower than the calculation result of graphene on Au(111), which is around 3.3 Å [258, 259]. We ascribed this large difference in value to the low conductance of graphene. Due to the low conductance of graphene physically adsorbing on Au(111), STM tip needs to approach closer to the less conductive graphene island to maintain the constant tunneling current.

The phenomenon that graphene growth crosses the step edges has also been observed on many metal surfaces in the past years [260, 251, 252]. Therefore, we have reasons to preliminarily propose the islands growing on Au(111) are graphene islands. The smoothness of these islands, shown in Figrue 4.1 c), indicating that there is no substantial interaction between the edge and the Au(111), otherwise it would lead to the pronounced corrugation at edges or lead to dome-shape structures [261, 262]. We also rule out the possibility of forming carbon-Au alloy since the herringbone reconstruction surface of Au(111) is intact.

Electronic structure of graphene on Au(111) has been investigated by differential conductance spectra. STS measurements have been performed at the positions of clean gold terrace close to the graphene island (as a reference) and above the graphene island, respectively, labeled with blue and red dots in the Figure 4.2 a) . From the spectra measurement result shown in Figure 4.2 b), the characteristic V shape of free-standing graphene close to Fermi level has not been observed, which indicating that the Dirac cone feature of free-standing graphene has not been detected with STS measurement. Similar phenomenon that the absence of Dirac point at Fermi level of the spectra taken on the graphene/Ag(111) or graphene/Cu(111) have been reported [263, 252]. This absence of Dirac point in the spectra is currently explained as the slight doping in graphene. The characteristic fingerprint of graphene, honeycomb structure, has not been observed either even though the low bias and high tunneling current parameters have been set according to previous reported parameters.

Preparation with higher ethylene pressure

Figure 4.3 a) shows the example of large island overgrowing the step edges of Au(111). Several bright dots can be observed inside the islands. These are even better visible in smaller-scale images or pseudo 3D representation of the STM image, shown in Figure 4.3 b) and c), respectively. Line profile results are displayed across three different directions in Figure 4.3 d). Firstly,the height difference across the step edge has also been measured, which is 2.3 ± 0.1 Å in the red curve. This also agrees quite well with the characteristic height of Au(111) step edge [46].

The apparent height of the island can be read out from the black curve in Figure 4.3 d), which is 3.1 ± 0.2 Å. This value is very close to the ones in the previous calculation reports of graphene on Au(111) [258, 259]. However, it is notable that, in Figrue 4.1, the apparent height of the island is around 2.2 Åindependent from the bias from -0.2 V to 1.0 V. The large difference in the value of the apparent height can be about 1.0 Å. Noted that the STM image of Figure 4.3 b) is obtained at 3.2 V, which is rather larger than that of Figrue 4.1 c). It means more electronic states between the island and the Au(111) have been measured. Moreover, the absence of Moiré pattern here indicates that the island is likely

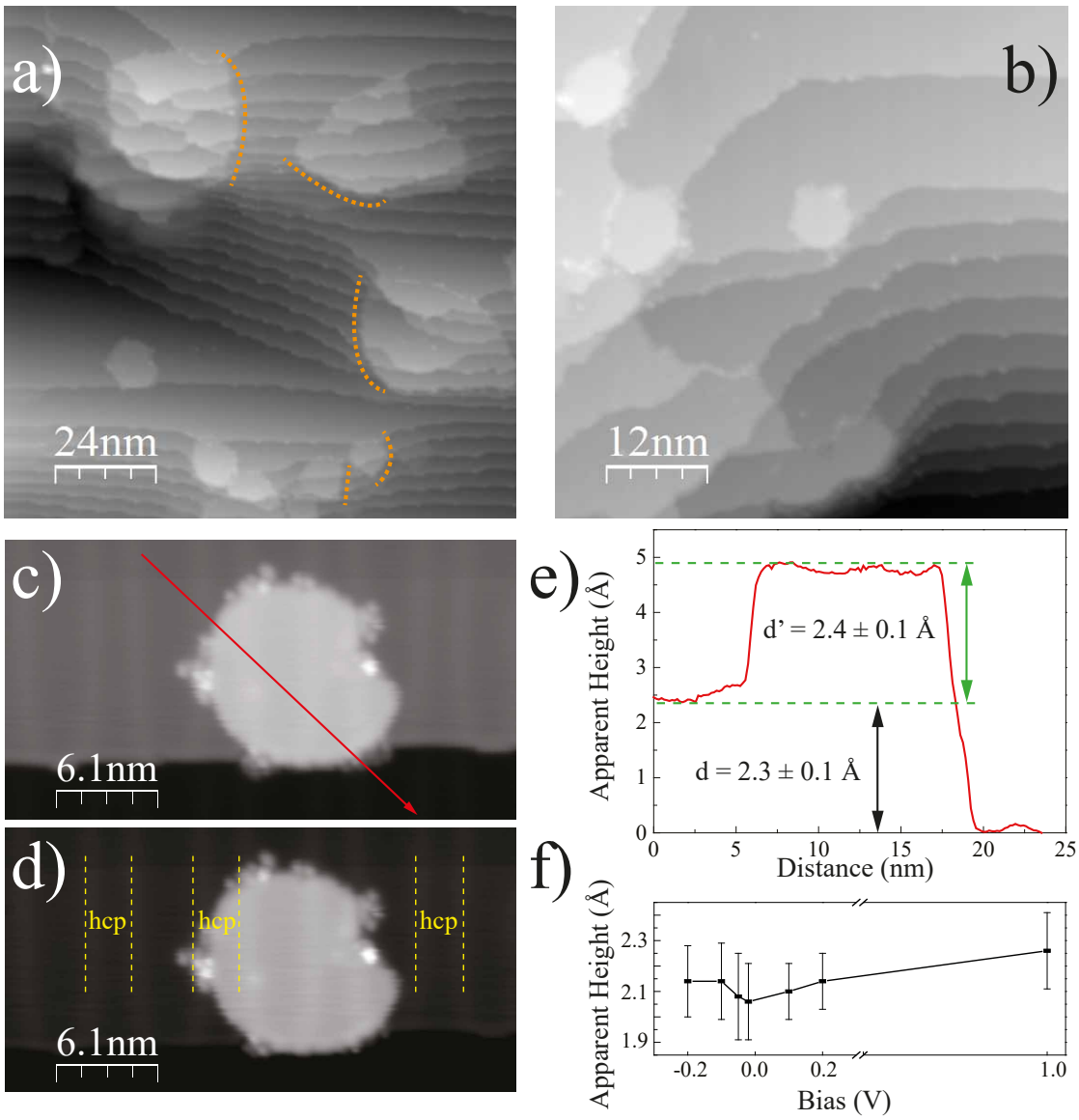

Figure 4.1: The organic island on Au(111). **a)** STM overview image of islands growing on Au(111) (V = 1.1 V, I = 38 pA). **b)** Another STM overview image of islands growing on Au(111) (V = 1.0 V, I = 23 pA). **c)** Zoom-in image of island growing from the step edge of Au(111). The red arrow marks the line profile in **e)** with direction. (V = 1.0 V, I = 0.1 nA). **d)** The contrast enhanced image of **b)** and hcp region and soliton lines have been highlighted with yellow dotted lines. **e)** Line profile result of **c)**. The height of step edge of Au(111) is d = 2.3 ± 0.1 Å. The apparent height of the island on Au(111) is d' = 2.26 ± 0.15 Å. **f)** Bias dependent apparent height of the island on Au(111).

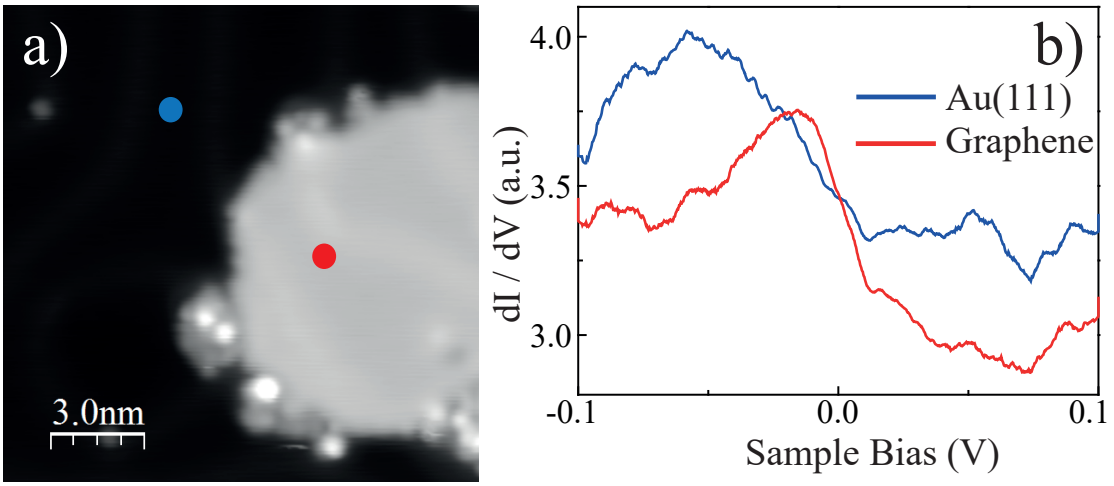

Figure 4.2: STS measurements around Fermi energy on graphene/Au(111) **a)** STM image of graphene island on Au(111). ($V = 1.0$ V, $I = 0.1$ nA.) **b)** STS measurements on gold terrace and graphene island/Au(111) respectively.

contacted from the surface below. The bright dots seen Figure 4.3 b) can also contribute the generation of the interface states. Similar observation has been reported and ascribed to the contacting between graphene and Ni(111) [264]. They are more likely some defects such as nanobubbles which have been reported in the case of graphene growth on Au(111) [254] and on Pt(111) [265]. The possibility of the impurities also cannot be excluded. Therefore, we conclude that the islands we obtained on Au(111) are graphene islands with defects and/or impurities. The interface states generated between graphene islands and Au(111) have dramatically influenced the apparent height measured with various biases.

4.3 Conclusions

We have growed graphene islands on Au(111) through sputtering ethylene gas and keeping the Au(111) surface at 1000 K. The islands exhibited some common features like previous reported graphene sheet on Au(111) as discussed above. The absence of the typical honeycomb structural appearance and electronic structure of Dirac cone of grpahene can be ascribed to the influence of the interface states due to the doping/contacting between the graphene islands and Au(111). Impurities can also play a role in the absence of typical graphene features. Doubled the amount of ethylene pressure in the preparation did not improve the quality of graphene islands. Higher annealing temperature may help to get rid of the impurities in the 2nd preparation and re-distribution of carbon atoms on the surface. Carbon-Au alloy can be ruled out in our experiments since the herringbone reconstruction surface of Au(111) is intact.

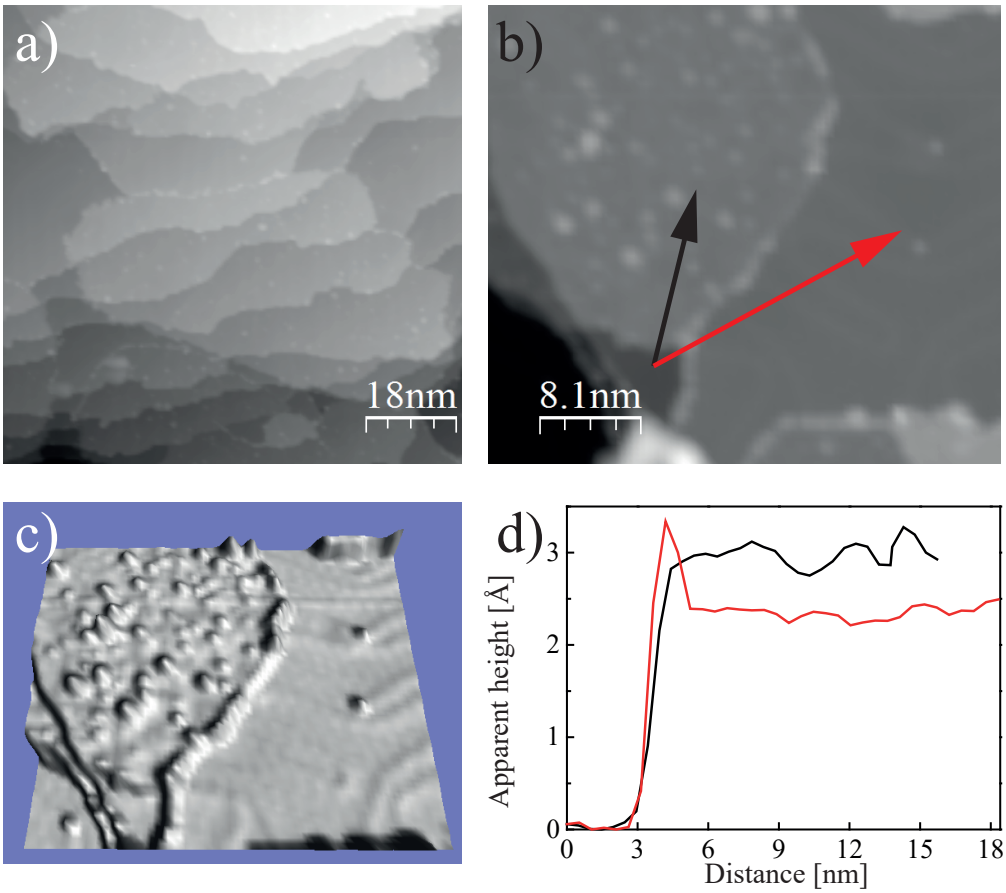

Figure 4.3: Apparent height of the island growing from the step edges of Au(111). **a)** STM overview image of islands growing on Au(111). (V = 2.0 V, I = 20 pA.) **b)** STM image from other area derived from the same preparation. Two line profiles crossing between the step edges and island have been measured, graphs can be seen in d) (V = 3.2 V, I = 11 pA). **c)** Pseudo 3-dimension image of **b)** area. A few protrusions can be found on the clean gold surface and a large number inside the island. The herringbone structure of Au(111) can be also resolved. **d)** Line profile results of b). The measured apparent height of step edge of Au(111) is 2.3 ± 0.1 Å, labeled with red arrow in b) and red curve in the graph of d) (similarly hereinafter). The apparent height of the island on Au(111) is 3.1 ± 0.2 Å according to the measurement along the black arrow.

5 Coordination of CBA Molecules with Cobalt Atoms on Au(111)

Metal-organic combination provides various possibilities to synthesize supramolecular architectures [266–268], nanoporous materials and low-dimensional nanostructures such as ladder structures, metal-organic coordination chains, etc. [158, 162, 269–276]. Among them, azobenzene molecules have been widely investigated theoretically and experimentally because of its interesting switching characteristics in the past years [277–280]. The interaction between azobenzene molecules and the metal surfaces is capable of tuning the switching characteristics. It has been reported that, for instance, di-metacyano-azobenzene (DMC) molecules with two isomers is stable on Au(111) [281]. The switching between two configurations can be triggered by STM tunneling electron. The incorporation of metal atoms could modify the alignment of molecular orbitals through metal-ligand hybridization [16, 282]. The involvement of evaporating cobalt (Co) atoms on DMC/Au(111) could lead to the metal-organic ligands and dramatically change the energy alignment in the mixed structure [283]. It is also notable that DMC molecule exhibits two stable configurations, named *trans* and *cis* on Cu(111) [284]. 4-carboxy benzylideneaniline (CBA) molecule is another acid molecule that has been investigated in our group. Compared to DMC molecule, instead of azo group, imine group connects two benzene rings. Two symmetric CN triple bonds are also replaced by single carboxylic group. Our colleague Christian Lotze has observed the wide-angle switching behaviour in the experiment of CBA/Au(111) with STM/STS [285]. It is notable that there are lone pair electrons of the N atom in the imine group of the CBA molecules. The lone pair electrons tend to form the metal-organic coordination bonding with the metal atoms [286]. It is foreseeable that the coordinated metal atoms will potentially influence the electronic structure and switching behaviours of CBA molecules on Au(111). The coordination competition between N atoms of the imine group and O atoms of the carboxylic group is also likely to take place. Therefore, in this chapter, we will investigate the influence of transition Co atoms in the CBA/Au(111) system.

5.1 DFT Calculation of CBA Molecule

As shown in Figure 5.1, a CBA molecule consists of two benzene rings connected by imine group, and single carboxylic group bonds to the benzene ring in the para-position close to the nitrogen atom side. The chemical formula of CBA is $C_{14}H_{11}O_2N$. It has been reported that there are two configurations of CBA molecule, called *trans* and *cis*, as shown in Figure 5.1 a) and b), respectively [285]. The *trans* state keeps two benzene rings in the same plane. In the *cis* phase one benzene ring is rotated out of the plane of the other benzene ring around the imine group. The two *trans-cis* isomerization can be reversibly switched by electrons induced by STM tip.

Density functional theory (DFT) calculation of the CBA molecule in gas phase has been carried out with Gaussian software. All the DFT calculation results were performed by referencing the Gaussian 09 program package [112] unless noted otherwise. All the calculations including geometry optimizations and electronic excitation energies were conducted on isolated systems, without considering the metal surfaces, using the B3LYP exchange-correlation function. The 6-31G (or 6-311G) basis set was chosen for the CBA gas phase calculation.

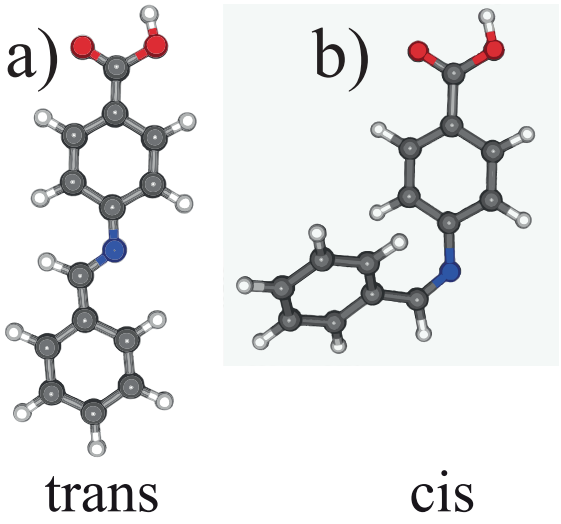

Figure 5.1: Two configuration gas phases of a CBA molecule. The gray, blue, red and white balls in the model represent C, N, O and H atoms, respectively. **a)** *trans* phase of CBA molecule **b)** *cis* phase of CBA molecule.

DFT calculation result of CBA in gas phase is shown in Figure 5.2. Figure 5.2 a) and b) represent the calculation results of HOMO and LUMO, respectively. The HOMO orbitals distribute homogeneously on the whole backbone of CBA molecule except the hydroxy moiety. To our surprise, we also find that the homogeneous orbital distribution of LUMO on CBA in gas phase. This means that the imine group of CBA molecule, where C=N double bond bridges two benzene rings, owns no extra orbitals as it would be expected due to the electronegativity of the C atom in the C=N double bond [287].

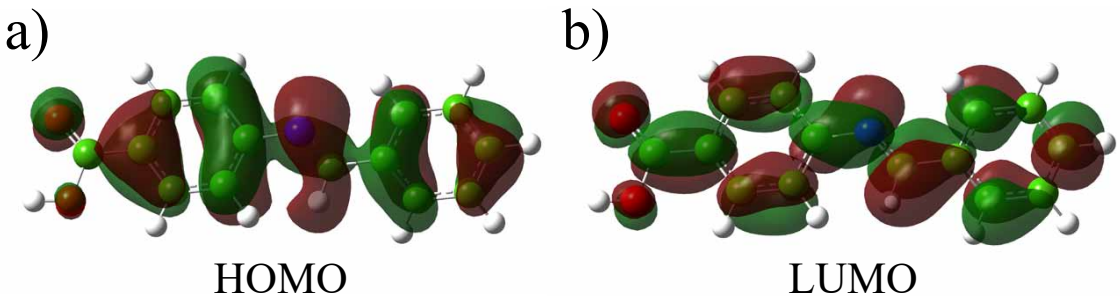

Figure 5.2: DFT calculation result of CBA molecule in gas phase. **a)** HOMO of CBA in gas phase. **b)** LUMO of CBA in gas phase.

5.2 Self-assembly of CBA Molecules on Au(111)

An experiment of self-assembled CBA molecules on Au(111) has been carried out with LT-STM under UHV condition. The CBA molecules have been preliminarily evaporated onto the gold surface cleaned by repeated sputtering and annealing process. The evaporation temperature of CBA molecules is approximately 170 °C and the substrate is kept at room temperature.

Figure 5.3 a) shows the overview STM image of self-assembly of CBA molecular chains

on Au(111). The Au(111) herringbone reconstruction can be clearly observed and nearly all the CBA molecules adsorb on the fcc regions. This preference indicates that the CBA molecules are more stable on the fcc regions than on the hcp regions. It is also notable that all the CBA molecules are lying planar on the surface, in another word, exhibiting *trans* state on Au(111). This adsorption behaviour has also been reported as the more stable configuration for CBA molecules on Au(111) [285].

We also notice that CBA molecules exhibit a dimer structure on the surface. This is in a good agreement with the feature of carboxylic group, which is facing each other through hydrogen bonds and mediating the formation of molecular assembly [205]. The zigzag CBA dimer row, which is shown in Figure 5.3 c), has been studied and proved to be consisted of two enantiomeric forms of *trans* CBA molecules when confined into a plane, called λ and ρ, respectively [285], shown in Figure 5.3 b). The formation of CBA dimer rows can be ascribed to the hydrogen bond between the H atom of benzene ring and N atom of imine group of the two adjacent CBA molecules. Therefore, it can be summarized that the stabilization is highly depended on the electrostatic intermolecular forces between positive hydrogen atoms and negative N site.

Constant current STS has been performed on the CBA molecule on Au(111). Spectra in Figure 5.3 d) are acquired at the center of two benzene rings of CBA molecule. The measured positions are highlighted in the image c) with blue and red dots respectively. There is a resonance of 2.0 V located in the outer benzene ring center, and a broader resonance 2.1 V located in the inner benzene ring center of CBA molecule. This resonance can be ascribed to the LUMO of CBA molecule. From the spectrum, it is notable that the intensity of the two resonances are nearly identical, indicating the distribution of LUMO in CBA molecule adsorbed on Au(111) is homogeneous. This phenomenon coincides very well with our DFT calculation result, suggesting the adsorption of CBA molecules on Au(111) did not dramatically influence the distribution of the molecular orbital.

Due to the limited strength of hydrogen bonds among the CBA dimers, during the constant current STS measurements, bias voltages cannot be swept higher than 2.5 V between tip and sample, otherwise the CBA molecules would jump out of the scanning area or distorted, even decomposed. For instance, in Figure 5.3 c), the terminal CBA dimers are obviously influenced by the constant current STS measurement. Before the measurement, the CBA dimers are parallel to each other in the row, seen the inset image of Figure 5.3 c). After the constant current STS measurement, the two terminal CBA dimers exhibit no longer parallel configurations, but crossed ones with CBA molecules facing each other. This observation gives us the presentative impression that the interaction between CBA molecules and Au(111) is weaker than the intermolecular interaction of the hydrogen bonding.

Bias dependent topographies have been measured on the CBA dimer chains. Figure 5.4 a) and b) are images taken at 0.2 V and 2.0 V, respectively. The 2.0 eV is also the LUMO energy measured from constant current STS measurement in Figure 5.3 d). In Figure 5.4 a), each CBA molecule performs the same appearance without prominent difference. Line profile measurement crossing the neighbouring molecules has been performed, which is along the red line in Figure 5.4 a). The apparent height of CBA molecule could reach 1.5 Å under 0.2 V. Due to the double hydrogen bonds OH$\cdots$N between the two neighbouring CBA molecules of the adjacent CBA dimer, CBA molecules could form dimer row on Au(111). In the image taken at the LUMO bias, shown in Figure 5.4 b), the two round shape benzene rings of each CBA molecule cannot be observed. Instead, more unoccupied

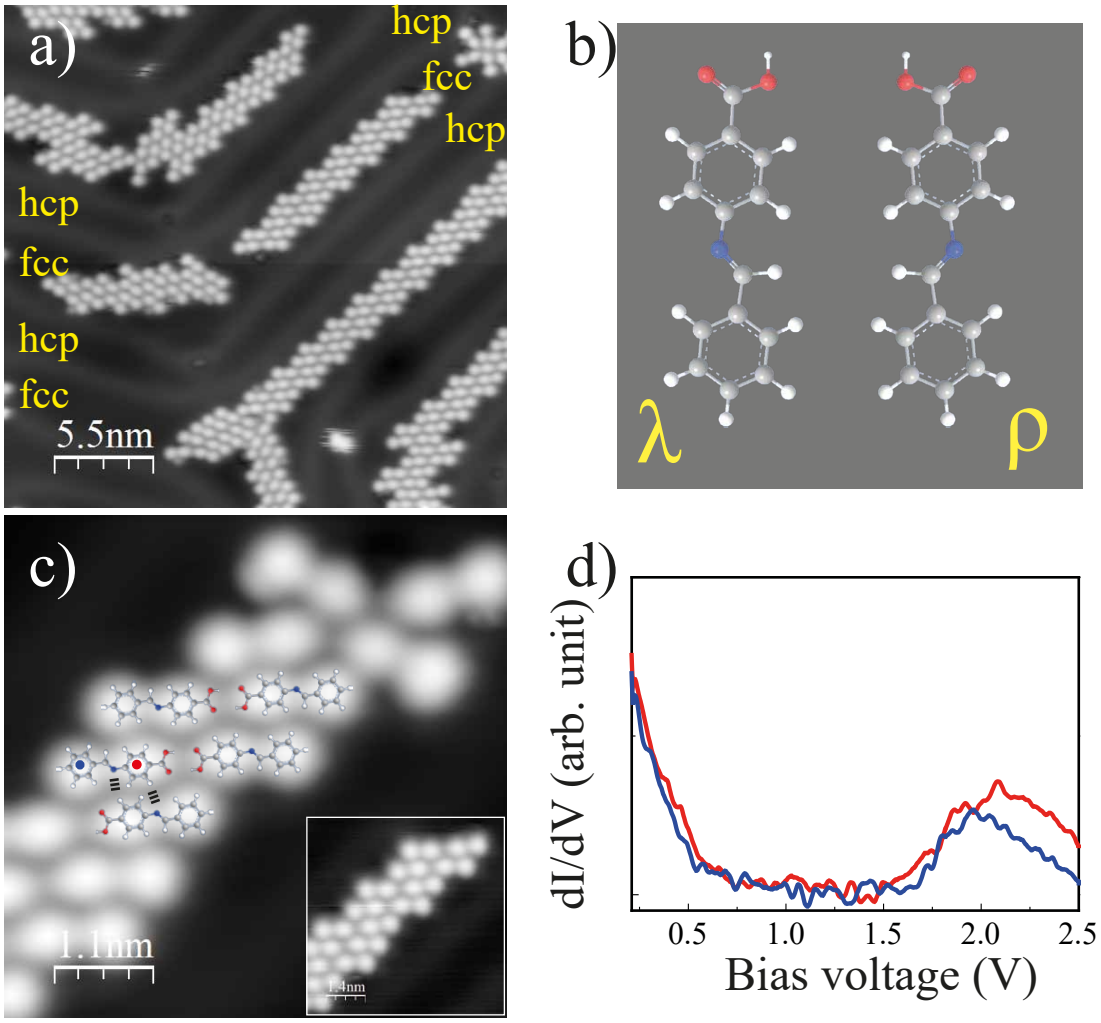

Figure 5.3: Self-assembly of CBA molecules on Au(111). **a)** Overview of STM topography of sub-monolayer CBA molecules on Au(111). The region of hcp and fcc of Au(111) has been highlighted ($V = 0.4$ V, $I = 0.1$ nA). **b)** The image shows the chiral structures of *trans* CBA molecule λ and ρ, respectively. The image is cited from ref. [285]. **c)** Zoom-in STM image of CBA dimer chain. The inset image is the CBA molecular behaviour before being performed constant current STS. CBA molecular model has been superimposed and hydrogen bonds OH$\cdots$N have been highlighted with triple black lines. The blue and red dots on the bright protrusions are the positions where constant current STS were taken. **d)** Constant current STS measurement results at the positive bias range on CBA molecules.

density of states can be observed in the imine group of CBA molecule, which is highlighted by purple circle in the same position of Figure 5.4 a) and b). Furthermore, the hydrogen bond OH···N also shows a stronger contrast enhancement which has not been observed under low bias voltage at all. This phenomenon can be explained as the elastic tunneling process has taken place at the LUMO resonant energy of 2.0 V bias. The tunneling electron tunneled through the resonant molecular channel into the metal substrate.

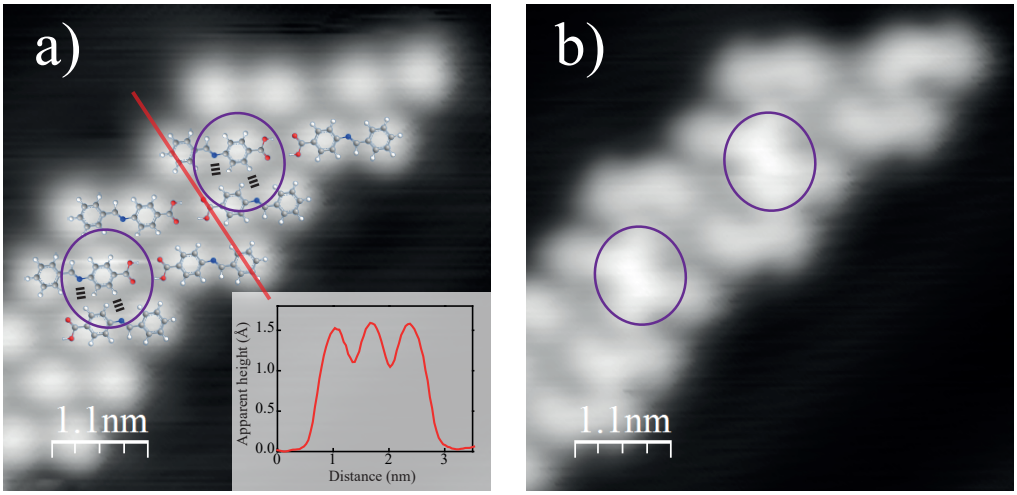

Figure 5.4: Bias dependent STM topographies of CBA dimer chains. **a)** CBA dimer chain image taken under $V = 0.2$ V, $I = 0.1$ nA. The OH···N hydrogen bonds have been highlighted by purple circles. **b)** CBA dimer chain image taken under $V = 2.0$ V, $I = 0.1$ nA.

5.3 Cobalt-CBA Metal-Organic Coordination on Au(111)

The combination of organic linkers with metal atoms on top of inorganic substrates offers promising perspectives for electronic devices. Coordination bonds between organic linkers and transition metal atoms could lead to the self-assembly of metal-organic nanostructures. Previous studies have shown that transition metal atoms binding to N sites of organic linkers could control the formation of metal-organic motifs, in which the metal atoms play a role as an anchor to connect the organic molecules [288–291].

In this part of experiment, transition atoms Co are evaporated onto the clean Au(111), which is kept at room temperature, by using a commercial Omicron UHV evaporator EFM3 equipped with high purity (> 99.995 %) metal rods. An integrated flux monitor is used to check the metal atom flux and control the metal coverage on the substrate surface. From the STM image shown in Figure 5.5, we could directly observe that Co nanoarrays are growing at the elbows of the reconstruction lines, which are the preferential nucleation sites for adsorbates on the reconstruction surface of Au(111) [46, 292–294]. From the line profile, the superlattice unit cell can be measured, which is approximately 6×16 nm^2 like a rectangle. The apparent height of 2.8 ± 0.2 Å reflects that the Co are clustered in 3D structures. Investigations of Co atoms adsorbed on Au(111) have been conducted in some previous works [293, 295–297], and 2.8 ± 0.2 Å of apparent height have been proved to be the bilayer Co clusters. The clusters lower than 2.8 ± 0.2 Å but higher than single Co atom can be given rise to the combination of Co atoms and impurities on the surface.

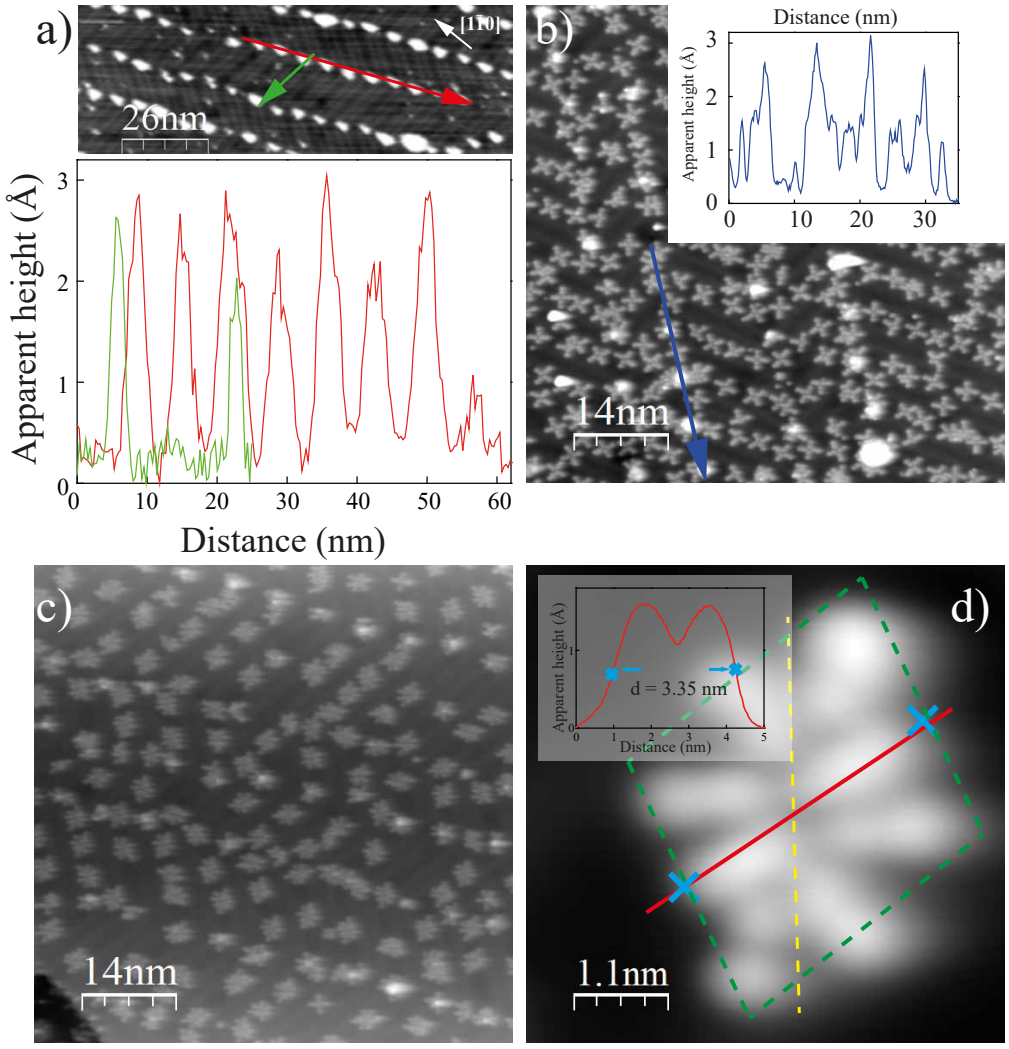

Figure 5.5: Measurement results of Co atoms and CBA molecules on Au(111). **a)** STM image of Co clusters on Au(111). The red line profile indicates that Co clusters locate at the elbow positions of Au(111) herringbone reconstruction. Green line profile measures the distance between two Co clusters in the neighbouring rows. The surface orientation is labeled in the topography with white arrow. ($V = 0.3$ V, $I = 0.1$ nA). **b)** STM overview image of evaporated CBA molecules onto Co/Au(111) sample. The inset graph is the line profile measurement along Co clusters on Au(111). ($V = 0.2$ V, $I = 47$ pA). **c)** STM overview image of annealing the sample in b) up to 370 K for 5 min. ($V = 0.2$ V, $I = 54$ pA). **d)** Zoom-in image of single metal-organic coordination structure taken from c). The line profile measurements shows the apparent height is approximately 1.6 Å. And shape of this structure is parralelogram, which is circled by the green dotted lines.

Next, CBA molecules have been evaporated onto the prepared Co/Au(111) sample surface without annealing the sample after the deposition. From the overview STM image shown in Figure 5.5 b) here, instead of self-assembled CBA dimer molecular chains, gold surface is covered with molecular cross. Some of the Co clusters cannot be observed on elbow positions of the gold surface, indicating that partial consumption of Co clusters has taken place. However, from the line profile measurement shown in the inset image of b), the apparent height of Co clusters exhibits the same value as it is measured before the CBA evaporation, which means the amount of Co atoms reacting with evaporated CBA molecules is limited.

Furthermore, it is notable that the increasing number of CBA cross conformation and absence of CBA dimer rows has taken place, comparing with the sample without evaporating Co atoms. In the CBA cross conformation, the bonding node indicates that four carboxylic groups are pointing towards each other. This kind of bonding configuration is highly unfavorable for the COOH terminations of CBA molecules on Au(111), otherwise we were supposed to observe it in the sample without evaporating Co atoms. Unless there is a metal atom center coordinating with them, which is supposed to be Co atom in our case. Thus, we propose that Co atoms are located in the center of the four CBA molecules, incorporated into the four carboxylic groups by coordination bonds, leading to a windmill structure. And similar arrangement has been introduced on the other acid molecules with transition metal center on Au(111) [298].

To study the behaviour of Co atoms in the clusters under thermal treatment, postannealing on the previous sample has been carried out under 370 K for 5 min. Figure 5.5 c) shows the overview STM topography of annealed sample. Here the number of Co islands is dramatically reduced compared to the observation in the Figure 5.5 a) and b). This phenomenon provides the evidence that a large amount of Co clusters is consumed to form the metal-organic nanostructure. We also notice that the windmill conformation in Figure 5.5 b) is nearly completely missing. Instead, the molecular clusters can be found on the gold surface, especially in the fcc region of Au(111). The small rest amount of Co clusters also states that, under the 370 K annealing temperature, metal organic coordination structures of this sample have been saturated by cobalt atoms. Further dissolution of Co island would be expected to be observed when annealing the sample to higher temperature, which is likely to generate the new reaction sites for CBA molecules. It is also notable that Au(111) keeps its hcp region intact, indicating that the intermixing or alloy formation between Co and Au(111) substrate has not taken place, Co atoms only reacted with CBA molecules.

Zoomed-in STM topography of coordination structures has been measured, shown in the Figure 5.5 d). From the initial look we could observe there are eight CBA molecules in total, forming a parallelogram shape structure which is framed by green dotted lines, symmetrically coordinating to the center of the molecular cluster. Among them, six of these molecules are showing up as two symmetric dimers, and two dimers are much more closer to the cluster center than the rest four molecules, which are located on the diagonal positions along the long axis of the coordination structure (symmetric line is labeled by yellow dotted line in the image). Line profile has been measured along the direction labeled in Figure 5.5 d), the apparent height is still 1.6 ± 0.1 Å which agrees very well with that measured on the self-assembled CBA dimer on Au(111), seen in the inset image of Figure 5.4.

Due to annealing the sample up to 370 K, chemical reaction between CBA molecules with

Co atoms can be expected. Indeed, deprotonation process can take place between CBA molecules and Co atoms on Au(111) [299]. The chemical reaction is also a irreversible process because the carboxylic groups of CBA molecules are triggered the deprotonation process, which means the H atoms of COOH would form molecular hydrogen H_2, desorbing from the gold surface, leaving the dangling bond of COO^- to coordinate with Co atoms. Hence the formation of metal-ligand bonds is predictable in this metal-organic coordination structure. The chemical reaction can be generally represented by the following chemical equation:

$$2R - (COOH) + Co_n \rightarrow Co_n(R - COO)_2 + H_2 \uparrow \tag{5.3.1}$$

We have also measured the constant current tunneling spectra on the metal-organic coordination structure. Figure 5.6 b) and d) show the measurement results corresponding to the positions taken in Figure 5.6 a) and c), respectively. We performed the STS measurements on the centers of the benzene rings close to and away from the center of metal-organic structure separately. From the spectra obtained on the benzene ring close to the coordination structure center (green, purple and blue squares in Figure 5.6 b)), there is a resonance at 1.5 eV and a relatively weak resonance at 2.7 eV. However, the spectrum measured on the red square position in Figure 5.6 a) shows only single strong resonance at 1.9 eV. The value slightly smaller than the LUMO energy of self-assembly CBA molecules on Au(111), which is 2.1 eV. We have also measured the constant current tunneling spectra on the outer benzene ring of this metal-organic coordination structure, and the measurement positions and results can be seen in Figure 5.6 c) and d). Again, we observe the common feature in the measured positions with blue, purple and green circles, which is the strong resonance at 1.9 eV and the relatively weaker resonance at 1.5 eV. The measurement on the red circle position exhibits no obvious peak. Only a small resonance at 2.1 eV can be observed, which position agrees well with the result obtained from the self-assembly of CBA molecules on Au(111).

Due to the overall distribution of 1.5 eV resonance, here we ascribe 1.5 eV to the new LUMO of CBA molecule due to the coordinated hybridization with the Co atoms. The hybridization is expected to happen between the Co 3d states and O atoms of CBA COOH group [283]. We also propose that 1.9 eV is the new LUMO+1, which has higher weight in the outer benzene ring moiety of the CBA molecule in the cluster. It is worthy to mention that, in Figure 5.6 b), the red square labeled position also exhibits a 1.9 eV. We assign it to the slight downshift of original LUMO of CBA molecules on Au(111) due to the intermolecular interaction [300, 301]. Hence, the 2.7 V resonance shown in Figure 5.6 b) can be ascribed to the LUMO+2 due to the coordination between CBA molecules and Co atoms. For the CBA molecule measured with red square and red circle in Figure 5.6 a) and c), there is no1.5 eV resonance in the constant current STS measurement, indicating the absence hybridization between the CBA molecules with Co atoms. Therefore, it is confirmed that there are two coordination mechanism in this metal-organic coordination structure, which are CBA molecules coordinating with and without Co atoms, respectively.

It can be concluded that the incorporation of Co atoms modifies the electronic structure of the CBA molecules. The new resonance at 1.5 eV proves the generation of the coordination between CBA molecules and Co atom centers. The downshift of the LUMO state from 2.1 V to 1.5 V can be attributed to the effect of hybridization between CBA molecules and Co atoms, leading to the re-distribution of the molecule-metal orbital. Due to the differences

the red labeled CBA molecule and mirrored one in the cluster bring about, especially the LUMO of the CBA molecule in this position is identical with that of the self-assembly CBA on Au(111), we ascribe this observation to the absence of interaction with Co atoms. The brighter benzene ring located uppermost in the in Figure 5.6 a) and c) is likely the *cis* state of CBA molecule or some other adatoms/dirt trapped inside, which needs to be further investigated.

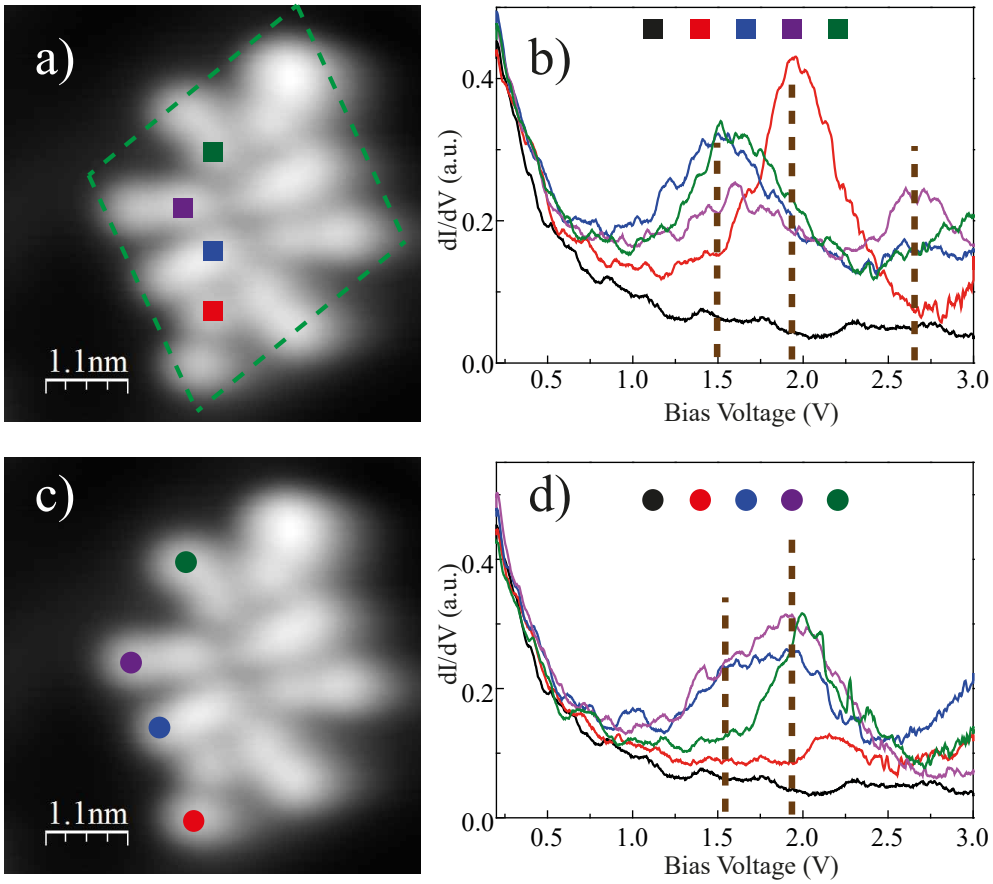

Figure 5.6: Constant current STS on metal-organic coordination structure. **a)** STS measurements on the inner benzene ring of CBA molecules. $V = 2.0$ V, $I = 54$ pA) **b)** STS measurement results on the inner benzene ring of CBA molecules. **c)** STS measurements on the outer benzene ring of CBA molecules. $V = 2.0$ V, $I = 54$ pA). **d)** STS measurement results on the outer benzene ring of CBA molecules.

Scanning tunneling line spectra along the long axis to the position passing the center of the coordination structure has been carried out, seen in Figure 5.8 a). The colour image as an inset in a) is the contour plot of the line spectra with 50 measurement points. The measurement range is fixed under positive bias ranging from 0.2 V to 3.0 V. It is notable that the coordination structure is stable and intact on the gold surface during sweeping the bias from low to high. By comparing with the unstable behaviour of CBA dimer structure on Au(111), there is supposed to be a mechanism of anchoring this new coordination structure on the gold substrate.

At the beginning of the line spectra measurements, there is no obvious resonance in the

measured range. Until to the center area of the coordination structure, resonance 1.9 eV has been observed. It starts from the the inner benzene ring of CBA molecule sitting on the long axis of parallelogram. This observation is in a good agreement with the result acquired from the CBA dimer (shown in Figure 5.3 c) and d)) as well as the measurement result in Figure 5.6 a) and b). Further approaching to the center of the coordination structure, two symmetric positions in the center exhibit a strong resonance located at 1.5 eV. But the 1.9 eV resonance cannot be observed in this area any more. Between these two symmetric centers with 1.5 eV resonance, there is a small window showing that no 1.5 eV resonance but a moderate resonance at 2.6 eV. Therefore, according to the resonance positions acquired from the line spectra contour map, we could conclude that, in this coordination structure, there are two coordination mechanism in this metal-organic coordination structure, which are CBA molecules coordinating with and without Co atoms, respectively.

A $\mathrm{d}I/\mathrm{d}V$ map has also been measured at the new LUMO energy position, i.e. 1.5 eV. Figure 5.8 b) is the STM topography simultaneously taken when $\mathrm{d}I/\mathrm{d}V$ map Figrue 5.8 c) is recorded. It is notable that, in the Figrue 5.8 c), the center of metal-organic coordination structure, there are two bright protrusions which are symmetrically sitting in the center of the coordination structure. This indicates that, the new LUMO of CBA molecule coordinated with Co atoms has more weight in the center of the metal-organic cluster. This $\mathrm{d}I/\mathrm{d}V$ map corroborates the fact that the molecular orbital alignment and spatial distribution within the cluster are highly modified by the incorporation of Co atoms.

Investigation on the carboxylic groups coordinating with transition metal center has been deeply performed for many years [302–304]. Among the numerous reports, there are two common features about the coordination between metal atoms and organic ligands. Two main 2D configurations related to COOH and metal (M) interactions can be summerized as: a monodentate configuration [302, 304–306] and a bidentate configuration [302, 304, 307, 308], seen in Figure 5.7. For the monodentate configuration, it means COOH group only provides single O atoms to coordinate with M atoms while leaving the other O atom coordinating with surroundings. The bidentate configuration can be further categorized into two sub-configurations: bridging bidentate and chelating bidentate, respectively. In the bridging bidentate situation, two ligands are at the bridging positions, which means single carboxylic group bridges two M atoms by bonding every single O atom of COOH to each M atom. Usually there will be another bridging bidentate in the mirrored position, making a symmetric configuration along the M-M axis. In the chelating bidentate situation, both oxygen (O) atoms of COOH bond to the same M atom (collinear with the M-M axis) and in the same way, there will be another at the axial positions in the mirrored position.

The combination of these two bidentate configurations have been observed in the experiments with the dinuclear centers [302, 273, 309–311], which states that M atoms prefer to form dimer conformation surrounded by organic ligands. With the modification on the functional groups of the organic molecules, the formation of large area metal-organic networks can be even realized, theoretically [312] and experimentally [304]. It is also notable that, among these published reports, the metal-organic bond length along the direction perpendicular to the M-M axis is always smaller than that collinear with the M-M axis, indicating the bidentate ligands are shorter than monodentate ligands. Moreover, the distance between the transition metal centers depends on the specific metal atoms, which falls into the range of 4 ± 1 Å. Such as the distance of Fe-Fe 4.7 ± 0.1 Å [302], Co-Co 4.105 Å [313], Co-Co 3.335 Å[314] and Co-Co 3.56 Å [315].

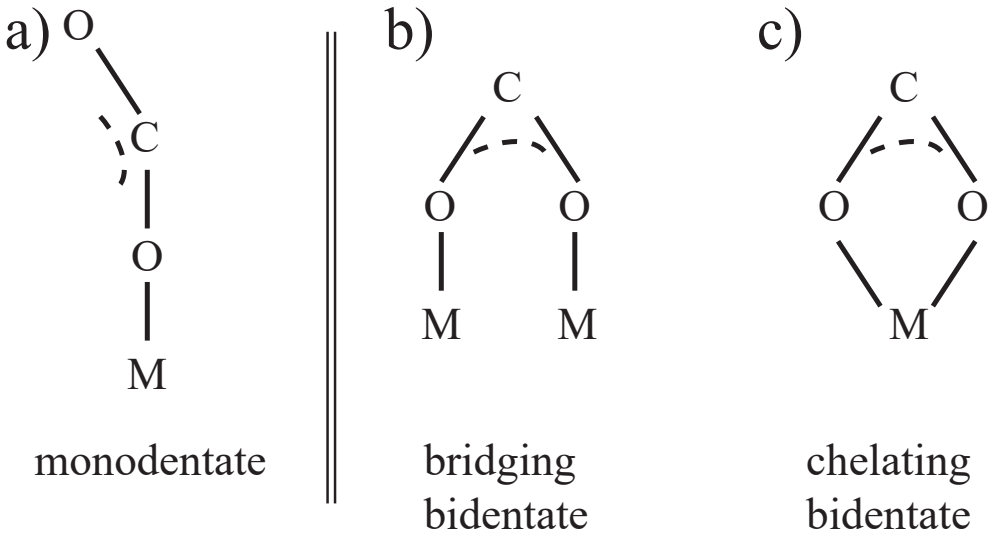

Figure 5.7: Two types of carboxylate-bridged dinuclear metal structures. **a)** Monodentate configuration **b)** Bridging bidentate configuration **c)** Chelating bidentate configuration

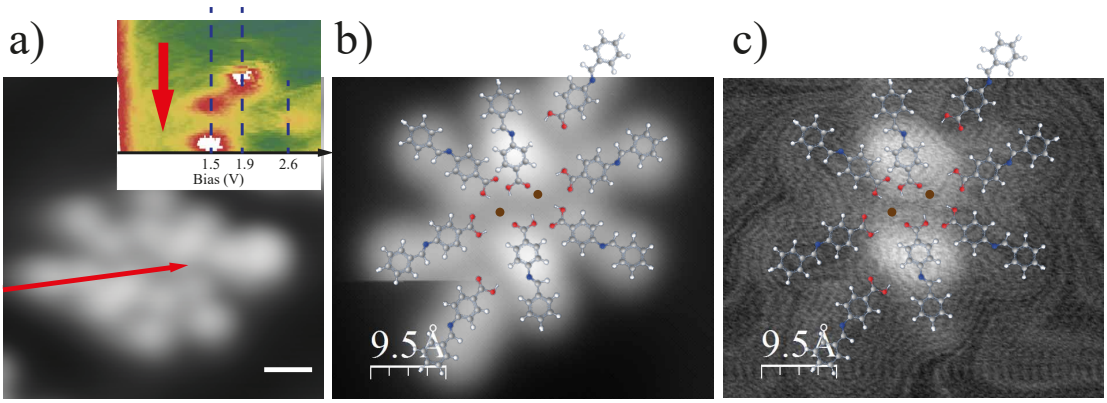

Figure 5.8: Line spectra on metal-organic coordination structure and $\mathrm{d}I/\mathrm{d}V$ map under the LUMO bias. **a)** Line spectra along the long axis of metal-organic coordination structure. Measuring direction has been marked with red arrow in the colour contour. The scale bar represents 1 nm. **b)** STM topography of metal-organic coordination structure. ($V = 1.5$ V, $I = 50$ pA). **c)** $\mathrm{d}I/\mathrm{d}V$ map of metal-organic coordination structure.

Therefore, according to the coordination principle of carobxylic groups with dinuclear metal centers, as well as our measurement results. We superimpose the model of CBA molecules on the STM image and dI/dV map, respectively, as shown in Figure 5.8 b) and c). Two CBA molecules in the center of the cluster coordinate with two Co atoms in the bridging bidentate configuration. Another two CBA molecules along the long axis of the cluster coordinate in the chelating bidentate configuration. Between these two groups of bidentate molecules, two CBA molecules bond to the central Co atoms in the monodentate conguration. The rest two CBA molecules, without directly coordinating with the dinuclear center, tend to form the hydrogen bonds with the neighbouring molecules due to the limitation space in the cluster. It can also be deduced that, in the coordination competition between lone pair electrons of N atom in the imine group and carboxylic group of CBA molecules, COOH is more favorable to coordinate with Co atoms on Au(111) after thermal treatment.

5.4 Conclusions

In this chapter, self-assembly of CBA molecules and the coordination between CBA molecules and Co atoms have been studied on Au(111). CBA molecules self-assemble into dimer rows on Au(111) through hydrogen bonds. The interaction between CBA molecules and gold substrate is rather weak, STS measurements with higher than moderate bias could induce the unstability of CBA on the surface.

The coordination of CBA carboxylic groups with Co atoms not only causes the different adsorption behaviour on Au(111), but also changes the electronic structure. Through thermal treatment with 370 K upon the CBA+Co sample, molecular clusters with eight CBA molecules can be observed separately on the gold surface. Furthermore, it is hardly seen the *cis* configuration of CBA molecules on the surface. Therefore, the coordination with Co atoms stabilized the CBA planar structure on the surface.

The coordination of CBA molecules with Co atoms also causes the downshift of the LUMO with respect to uncoordinated CBA molecules. This indicates that the orbital energy re-aligned by metal-ligand hybridization. These results depict that the co-evaporation of CBA molecules and Co atoms on Au(111) not only can influence the adsorption behaviours and formation, but also could mediate the electronic state due to the metal-organic hybridization. In the coordination race between N atom in the imine group and O atom in the carboxylic group, COOH site turns to be more favorable to coordinate with Co atoms on Au(111) after thermal treatment.

6 Summary

In this thesis, we investigated the precursor molecules (DBBA and FcAd) of fabricating graphene nanoribbons and triangular shape of graphene, including their structural and electrical properties on the metal substrates varying from Au(111), Ag(111) to Cu(111). Heating influence on these molecular building blocks have also been studied. Additionally, metal-organic coordination between CBA molecules and Co atoms has been analyzed by utilizing low temperature STM.

After the deposition on Au(111), DBBA molecules self-assembled into ordered molecular islands. Instead of covalently bonding to the gold substrate, DBBA molecules interact with each other through hydrogen bonding and $\pi\cdots\pi$ bonding inside the molecular row. The halogen bonding between the molecular row lead to the DBBA molecular island. Lateral manipulation is capable of taking single DBBA molecule out of the molecular island without destruction. The HOMO-LUMO gap narrowed down to the 2.5 eV of single DBBA molecule from 2.7 eV of DBBA in the molecular island. The slight downshift can be ascribed to a larger interaction between the single DBBA molecule and the gold substrate due to the flattening of the single DBBA molecule.

Annealing the DBBA/Au(111) sample up to 100 °C, the self-assembly DBBA molecular island could not be observed on the gold surface, however, two new phases with different configurations can be obtained. Phase1 contains six DBBA molecules packing in a clockwise direction through the halogen bonds in the hexamer center. Phase2 consists of three DBBA molecules, and the trimers are also stabilized by halogen bonds and $CH\cdots\pi$ interaction inside the trimer. The fact that the number of the Phase2 is larger than that of Phase1 indicates that the former one lowers the total energy and becomes more favourable configuration on the surface.

When annealing the DBBA/Au(111) sample up to 200 °C, the polymer chains can be obtained. The formation of the polymer chains is due to the occurrence of the dehalogenation process in the heating process. After the detachment of Br atoms from the anthracene units, the Ullmann reaction makes the radicals covalently bond together. Lateral manipulation upon the polymers cannot pull the chains apart, suggesting the formation of covalent bonds. However, because of the steric repulsion caused by the hydrogen atoms of the anthracene units, the polymer chain still keeps a 3D configuration on the gold surface.

Respectively annealing the DBBA/Au(111) under two different temperatures, 250 °C and 330 °C, can open two channels of cyclodehydrogenation process. In the case of 250 °C annealing temperature, the polymer chains start the cyclodehydrogenation process from the single terminal of the polymer chain and in a zigzag manner. However, like a failure of Domino effect, the cyclodehydrogenation process stops in the middle part of the chain. We ascribed this to the lack of enough energy to overcome the increasing energy barriers in the cyclodehydrogenation process. On the contrary, under the circumstance of 330 °C annealing temperature, the polymer chains undergo a different cyclodehydrogenation process. In detail, one side of upper part of anthrecene unit has finished its cyclodehydrogenation process on the gold surface, but the other side keeps their polymer appearance. This phenomenon clearly confirms that there are two cyclodehydrogenation process channels are opened under two annealing temperatures. The energy barriers to overcome in these two processes need to be further supported with DFT calculation.

7-AGNR can be obtained when the DBBA/Au(111) sample is annealed to 400 °C. The HOMO-LUMO gap is 2.8 eV which is in a good agreement with other published reports [138]. The LUMO is delocalized along the armchair edges of the ribbon. Moreover, the Tamm state locating at 0.03 eV is observed in the STS measurement result. It is only located in the zigzag edges of the ribbon termini.

Laser illumination upon DBBA/Au(111) could lead to some molecular islands with ordered structures. In detail, the islands consist of molecular rows with the same appearance. The size of the single rod-like structure is nearly 2.0 nm length and 1.5 Åwidth. These values coincide very well with the size of single tetradecane molecule. Therefore, we ascribed to the emergence of the tetradecane molecules to the effect of laser illumination. The energy provided by laser cleave the anthracene units into carbon chains, and the radicals re-bond locally to each other, leading to the formation of the tetradecane molecules. The laser experiment inspires us that there is more possiblity to fabricate alkane chains on the metal surfaces.

Another precursor molecule (FcAd) of fabricating triangular graphene patches on Cu(111) has been investigated on Ag(111) and Cu(111), respectively. On the Ag(111), FcAd molecules self-assembled into molecular island with two adsorption configurations, vertically and horizontally, respectively. The vertical FcAd molecules on Ag(111) formed molecular dimers through the hydrogen bonds of the upper Cp rings, and are likely collectively stabilized by the lower COOH groups interacting with the neighbouring hydrogen atoms inside the dimers. Besides, the horizontal FcAd molecules on Ag(111) play a role as a bridge vising the vertical FcAd molecules, further supporting the growth of the FcAd molecular island the silver substrate. On the Cu(111), FcAd molecules also self-assembled into the ordered molecular island. However, only the horizontal adsorption behaviour can be confirmed on the copper surface. In detail, FcAd molecular island is stabilized through T-shape CH$\cdots\pi$ interaction. Bias voltage pulses could slightly change the local adsorption site of the horizontal FcAd molecule and its neighbouring molecules inside the molecular island. Thermal treatment on the FcAd/Cu(111) sample could obtain the small size of triangular graphene patches. The obstacles to gain larger scale of graphene island is likely due to the large number of the thermal induced derivatives distributing on the surface, which hinder the growth of triangular graphene island.

We also attempted to fabricate graphene on Au(111) by sputtering the ethylene gas. The obtained organic structures did not exhibit the typical honeycomb structure of graphene sheet. STS measurements also did not detect the Dirac cone in the spectra. However, the apparent height and the smooth feature of the organic islands indicate that these islands might be consisted of carbon atoms with disordered arrangement. The hexagonal carbon structures of grpahene are likely replaced by other polygons consisted of carbon atoms. We also rule out the possibility of forming carbon-Au alloy since the herringbone reconstruction surface of Au(111) is intact.

Self-assembly of CBA molecules and the coordination between CBA molecules and Co atoms have also been studied on Au(111). CBA molecules self-assembled into dimer rows on Au(111) through hydrogen bonding. Switching behaviours of CBA molecules on Au(111) has been published by our group colleague [285]. Therefore, we investigate the co-deposition of CBA molecules and Co atoms on Au(111) in order to detect whether the Co atoms could anchor the imine group of CBA molecules onto the surface. The coordination of CBA carboxylic groups with Co atoms not only causes the different molecular

adsorption behaviours on Au(111), but also changes the electronic structure. Through thermal treatment with 370 K to the CBA+Co/Au(111) sample, the molecular clusters consisting of eight CBA molecules can be observed on Au(111). Furthermore, it is hardly seen the *cis* configuration of CBA molecules on the surface. Therefore, the coordination with Co atoms stabilized the CBA planar structure on the surface through bonding to the COOH group of CBA molecules. However, the Co atoms did not coordinate with the N atom of the imine group of CBA molecules as we expected in the beginning. The interaction between Co atoms with COOH groups seems more preferential under the annealing condition.

The coordination of CBA molecules with Co atoms causes the downshift of the LUMO with respect to uncoordinated CBA molecules. This indicates that the orbital energy realigned by metal-ligand hybridization. These results depict that the co-evaporation of CBA molecules and Co atoms on Au(111) not only can influence the adsorption behaviours and formation, but also could mediate the electronic state due to the metal-organic hybridization.

The above studies not only exhibit investigation result related to the structural and electrical properties of the precursor molecules of fabricating graphene on different metal surfaces, but also reveal that studies on the molecular building blocks are quite valuable for the supramolecular architectures, and very important for the fabrication of electric devices in the future. Systematically investigating the precursor molecules could develop more possibilities for fabricating devices in the application field.

List of Abbreviations

(LT-)STM: (low temperature) scanning tunneling microscopy

STS: scanning tunneling spectroscopy

DOS: density of state

Differential conductance: dI/dV

IETS: inelastic electron tunneling spectroscopy

DBBA: 10,10'-dibromo-9,9'-bianthryl

FcAd: 1,1-ferrocenedicarboxylic acid

CBA: 4-carboxy benzylideneaniline

vdW: van der Waals

CPD: contact potential difference

UHV: ultra high vacuum

hcp: hexagonal close packed

fcc: face centered cubic

RT: room temperature

CFT: crystal field theory

LFT: ligand field theory

$\boldsymbol{E_F}$: Fermi energy

ZBP: zero bias peak

$\boldsymbol{T_K}$: Kondo temperature

FWHM: full width at half maximum

COOH: carboxylic group

DFT: density functional theory

LDOS: local density of states

HOMO: highest occupied molecular orbital

LUMO: lowest unoccupied molecular orbital

Bibliography

[1] R. Martel, T. Schmidt, H. R. Shea, T. Hertel, and Ph. Avouris. Single- and multi-wall carbon nanotube field-effect transistors. *Applied Physics Letters*, 73(17):2447–2449, 1998.

[2] Z. J. Donhauser, B. A. Mantooth, K. F. Kelly, L. A. Bumm, J. D. Monnell, J. J. Stapleton, D. W. Price, A. M. Rawlett, D. L. Allara, J. M. Tour, and P. S. Weiss. Conductance switching in single molecules through conformational changes. *Science*, 292(5525):2303, 2001.

[3] Thomas Rueckes, Kyoungha Kim, Ernesto Joselevich, Greg Y. Tseng, Chin-Li Cheung, and Charles M. Lieber. Carbon nanotube-based nonvolatile random access memory for molecular computing. *Science*, 289(5476):94, 2000.

[4] C. Rogero, J. I. Pascual, J. Gómez-Herrero, and A. M. Baró. Resolution of site-specific bonding properties of C60 adsorbed on Au(111). *The Journal of Chemical Physics*, 116(2):832–836, 2001.

[5] James A. Theobald, Neil S. Oxtoby, Michael A. Phillips, Neil R. Champness, and Peter H. Beton. Controlling molecular deposition and layer structure with supramolecular surface assemblies. *Nature*, 424:1029–1031, 2003.

[6] Leonhard Grill, Matthew Dyer, Leif Lafferentz, Mats Persson, Maike V. Peters, and Stefan Hecht. Nano-architectures by covalent assembly of molecular building blocks. *Nat Nano*, 2(11):687–691, 2007.

[7] Nikolas A. A. Zwaneveld, Rémy Pawlak, Mathieu Abel, Daniel Catalin, Didier Gigmes, Denis Bertin, and Louis Porte. Organized formation of 2D extended covalent organic frameworks at surfaces. *Journal of the American Chemical Society*, 130(21):6678–6679, 2008.

[8] Inanc Meric, Melinda Y. Han, Andrea F. Young, Barbaros Ozyilmaz, Philip Kim, and Kenneth L. Shepard. Current saturation in zero-bandgap, top-gated graphene field-effect transistors. *Nat Nano*, 3(11):654–659, 2008.

[9] Yu-Ming Lin, Keith A. Jenkins, Alberto Valdes-Garcia, Joshua P. Small, Damon B. Farmer, and Phaedon Avouris. Operation of graphene transistors at gigahertz frequencies. *Nano Letters*, 9(1):422–426, 2009.

[10] Fengnian Xia, Damon B. Farmer, Yu-ming Lin, and Phaedon Avouris. Graphene field-effect transistors with high on/off current ratio and large transport band gap at room temperature. *Nano Letters*, 10(2):715–718, 2010.

[11] Melinda Y. Han, Barbaros Özyilmaz, Yuanbo Zhang, and Philip Kim. Energy band-gap engineering of graphene nanoribbons. *Physical Review Letters*, 98(20):206805, 2007.

[12] Kyoko Nakada, Mitsutaka Fujita, Gene Dresselhaus, and Mildred S. Dresselhaus. Edge state in graphene ribbons: Nanometer size effect and edge shape dependence. *Physical Review B*, 54(24):17954–17961, 1996.

[13] Xinran Wang and Hongjie Dai. Etching and narrowing of graphene from the edges. *Nature Chemistry*, 2(8):661–665, 2010.

[14] Jinming Cai, Pascal Ruffieux, Rached Jaafar, Marco Bieri, Thomas Braun, Stephan Blankenburg, Matthias Muoth, Ari P. Seitsonen, Moussa Saleh, Xinliang Feng, Klaus Müllen, and Roman Fasel. Atomically precise bottom-up fabrication of graphene nanoribbons. *Nature*, 466(7305):470–473, 2010.

[15] Xiu Chen, Shuyi Liu, Lacheng Liu, Xiaoqing Liu, Xiaoming Liu, and Li Wang. Growth of triangle-shape graphene on Cu(111) surface. *Applied Physics Letters*, 100(16), 2012.

[16] Weihua Wang, Xingqiang Shi, Chensheng Lin, Rui Qin Zhang, Christian Minot, Michel A. Van Hove, Yuning Hong, Ben Zhong Tang, and Nian Lin. Manipulating localized molecular orbitals by single-atom contacts. *Physical Review Letters*, 105:126801, 2010.

[17] Russell Young, John Ward, and Fred Scire. Observation of metal-vacuum-metal tunneling, field emission, and the transition region. *Physical Review Letters*, 27(14):922–924, 1971.

[18] Russell Young, John Ward, and Fredric Scire. The topografiner: An instrument for measuring surface microtopography. *Review of Scientific Instruments*, 43(7):999–1011, 1972.

[19] Tobias R. Umbach. Magnetic and electronic properties of supramolecular architectures on metal surfaces. *PhD thesis*, 2013.

[20] G. Binnig, H. Rohrer, Ch. Gerber, and E. Weibel. 7×7 reconstruction on Si(111) resolved in real space. *Physical Review Letters*, 50(2):120–123, 1983.

[21] G. Binnig, H. Rohrer, Ch. Gerber, and E. Weibel. Tunneling through a controllable vacuum gap. *Applied Physics Letters*, 40(2):178–180, 1982.

[22] G. Binnig, H. Rohrer, Ch. Gerber, and E. Weibel. Surface studies by scanning tunneling microscopy. *Physical Review Letters*, 49:57–61, 1982.

[23] G. Binnig, C. F. Quate, and Ch. Gerber. Atomic force microscope. *Physical Review Letters*, 56:930–933, 1986.

[24] J. Tersoff and D. R. Hamann. Theory of the scanning tunneling microscope. *Physical Review B*, 31:805–813, 1985.

[25] J. Tersoff and D. R. Hamann. Theory and application for the scanning tunneling microscope. *Physical Review Letters*, 50:1998–2001, 1983.

[26] J. Bardeen. Tunnelling from a many-particle point of view. *Physical Review Letters*, 6:57–59, 1961.

[27] A. Selloni, P. Carnevali, E. Tosatti, and C. D. Chen. Voltage-dependent scanning-tunneling microscopy of a crystal surface: Graphite. *Physical Review B*, 31:2602–2605, 1985.

[28] Gerhard Meyer, Ludwig Bartels, and Karl-Heinz Rieder. Atom manipulation with the stm: nanostructuring, tip functionalization, and femtochemistry. *Computational Materials Science*, 20(3):443–450, 2001.

[29] Georgy Kichin, Christian Weiss, Christian Wagner, F. Stefan Tautz, and Ruslan Temirov. Single molecule and single atom sensors for atomic resolution imaging of chemically complex surfaces. *Journal of the American Chemical Society*, 133(42):16847–16851, 2011.

[30] W. Ho. Single-molecule chemistry. *The Journal of Chemical Physics*, 117(24):11033–11061, 2002.

[31] Joseph A. Stroscio, R. M. Feenstra, and A. P. Fein. Electronic structure of the Si(111)2 $\times$ 1 surface by scanning-tunneling microscopy. *Physical Review Letters*, 57:2579–2582, 1986.

[32] N. D. Lang. Spectroscopy of single atoms in the scanning tunneling microscope. *Physical Review B*, 34:5947–5950, 1986.

[33] C. Wagner, R. Franke, and T. Fritz. Evaluation of I(V) curves in scanning tunneling spectroscopy of organic nanolayers. *Physical Review B*, 75:235432, 2007.

[34] Harold J.W. Zandvliet and Arie van Houselt. Scanning tunneling spectroscopy. *Annual Review of Analytical Chemistry*, 2(1):37–55, 2009.

[35] Roland Wiesendanger. *Scanning Probe Microscopy and Spectroscopy: Methods and Applications*. Cambridge University Press, Cambridge, 1994.

[36] R.M. Feenstra, Joseph A. Stroscio, and A.P. Fein. Tunneling spectroscopy of the Si(111)2 $\times$ 1 surface. *Surface Science*, 181:295–306, 1987.

[37] R. M. Feenstra. Tunneling spectroscopy of the (110) surface of direct-gap iii-v semiconductors. *Physical Review B*, 50(7):4561–4570, 1994.

[38] M. Ziegler, N. Néel, A. Sperl, J. Kroger, and R. Berndt. Local density of states from constant-current tunneling spectra. *Physical Review B*, 80(12):125402, 2009.

[39] Lucas Braun. Fingerprints of a magnetic molecule on a superconductor: Fe(iii)-octaethylporphyrin-cl on Pb(111). *PhD thesis*, 2011.

[40] I. Horcas, R. Fernández, J. M. Gómez-Rodríguez, J. Colchero, J. Gómez-Herrero, and A. M. Baro. Wsxm: A software for scanning probe microscopy and a tool for nanotechnology. *Review of Scientific Instruments*, 78(1):013705, 2007.

[41] Robin Ohmann, Giacomo Levita, Lucia Vitali, Alessandro De Vita, and Klaus Kern. Influence of subsurface layers on the adsorption of large organic molecules on close-packed metal surfaces. *ACS Nano*, 5(2):1360–1365, 2011.

[42] W. Chen, V. Madhavan, T. Jamneala, and M. F. Crommie. Scanning tunneling microscopy observation of an electronic superlattice at the surface of clean gold. *Physical Review Letters*, 80(7):1469–1472, 1998.

[43] M. F. Crommie, C. P. Lutz, and D. M. Eigler. Confinement of electrons to quantum corrals on a metal surface. *Science*, 262(5131):218–220, 1993.

[44] Jiutao Li, Wolf-Dieter Schneider, and Richard Berndt. Local density of states from spectroscopic scanning-tunneling-microscope images: Ag(111). *Physical Review B*, 56:7656–7659, 1997.

[45] Y. Pennec, W. Auwärter, A. Schiffrin, A. Weber-Bargioni, A. Riemann, and J. V. Barth. Supramolecular gratings for tuneable confinement of electrons on metal surfaces. *Nature Nanotechnology*, 2:99–103, 2007.

[46] J. V. Barth, H. Brune, G. Ertl, and R. J. Behm. Scanning tunneling microscopy observations on the reconstructed Au(111) surface: Atomic structure, long-range superstructure, rotational domains, and surface defects. *Physical Review B*, 42:9307–9318, 1990.

[47] D. D. Chambliss, R. J. Wilson, and S. Chiang. Nucleation of ordered ni island arrays on Au(111) by surface-lattice dislocations. *Physical Review Letters*, 66(13):1721–1724, 1991.

[48] Matthias Böhringer, Karina Morgenstern, Wolf-Dieter Schneider, Richard Berndt, Francesco Mauri, Alessandro De Vita, and Roberto Car. Two-dimensional self-assembly of supramolecular clusters and chains. *Physical Review Letters*, 83(2):324–327, 1999.

[49] P. Heimann, H. Neddermeyer, and H. F. Roloff. Ultraviolet photoemission for intrinsic surface states of the noble metals. *Journal of Physics C: Solid State Physics*, 10(1):L17, 1977.

[50] F. Reinert, G. Nicolay, S. Schmidt, D. Ehm, and S. Hüfner. Direct measurements of the L -gap surface states on the (111) face of noble metals by photoelectron spectroscopy. *Physical Review B*, 63(11):115415, 2001.

[51] M. F. Crommie, C. P. Lutz, and D. M. Eigler. Imaging standing waves in a two-dimensional electron gas. *Nature*, 363:524–527, 1993.

[52] Yuanbo Zhang, Yan-Wen Tan, Horst L. Stormer, and Philip Kim. Experimental observation of the quantum hall effect and berry's phase in graphene. *Nature*, 438(7065):201–204, 2005.

[53] K. S. Novoselov, A. K. Geim, S. V. Morozov, D. Jiang, Y. Zhang, S. V. Dubonos, I. V. Grigorieva, and A. A. Firsov. Electric field effect in atomically thin carbon films. *Science*, 306(5696):666–669, 2004.

[54] R. R. Nair, P. Blake, A. N. Grigorenko, K. S. Novoselov, T. J. Booth, T. Stauber, N. M. R. Peres, and A. K. Geim. Fine structure constant defines visual transparency of graphene. *Science*, 320(5881):1308–1308, 2008.

[55] Changgu Lee, Xiaoding Wei, Jeffrey W. Kysar, and James Hone. Measurement of the elastic properties and intrinsic strength of monolayer graphene. *Science*, 321(5887):385–388, 2008.

[56] Marco Bieri, Matthias Treier, Jinming Cai, Kamel Ait-Mansour, Pascal Ruffieux, Oliver Groning, Pierangelo Groning, Marcel Kastler, Ralph Rieger, Xinliang Feng, Klaus Müllen, and Roman Fasel. Porous graphenes: two-dimensional polymer synthesis with atomic precision. *Chemical Communications*, (45):6919–6921, 2009.

[57] Klaus Müllen. Evolution of graphene molecules: Structural and functional complexity as driving forces behind nanoscience. *ACS Nano*, 8(7):6531–6541, 2014.

[58] Matthias Koch, Francisco Ample, Christian Joachim, and Leonhard Grill. Voltage-dependent conductance of a single graphene nanoribbon. *Nat Nano*, 7(11):713–717, 2012.

[59] Sampsa K. Hämäläinen, Zhixiang Sun, Mark P. Boneschanscher, Andreas Uppstu, Mari Ijäs, Ari Harju, Daniël Vanmaekelbergh, and Peter Liljeroth. Quantum-confined electronic states in atomically well-defined graphene nanostructures. *Physical Review Letters*, 107(23):236803, 2011.

[60] R. F. Dou K. Wedeking G. Erker L. F. Chi D. Y. Zhong, W. C. Wang and H. Fuchs. Oligoethylene-bridged diferrocene on Ag(110): Monolayer structures and adsorbate-induced faceting. *Physical Review B*, 76(20):205428, 2007.

[61] Joost Jvan der Lit, Mark P. Boneschanscher, Daniël Vanmaekelbergh, Mari ljäs, Andreas Uppstu, Mikko Ervasti, Ari Harju, Peter Liljeroth, and Ingmar Swart. Suppression of electron-vibron coupling in graphene nanoribbons contacted via a single atom. *Nature Communications*, 4:2023, 2013.

[62] M. Ijäs, M. Ervasti, A. Uppstu, P. Liljeroth, J. van der Lit, I. Swart, and A. Harju. Electronic states in finite graphene nanoribbons: Effect of charging and defects. *Physical Review B*, 88(7):075429, 2013.

[63] John W. Colson, Arthur R. Woll, Arnab Mukherjee, Mark P. Levendorf, Eric L. Spitler, Virgil B. Shields, Michael G. Spencer, Jiwoong Park, and William R. Dichtel. Oriented 2d covalent organic framework thin films on single-layer graphene. *Science*, 332(6026):228–231, 2011.

[64] Leopold Talirz, Hajo Sode, Jinming Cai, Pascal Ruffieux, Stephan Blankenburg, Rached Jafaar, Reinhard Berger, Xinliang Feng, Klaus Müllen, Daniele Passerone, Roman Fasel, and Carlo A. Pignedoli. Termini of bottom-up fabricated graphene nanoribbons. *Journal of the American Chemical Society*, 135(6):2060–2063, 2013.

[65] Alexander Riss, Sebastian Wickenburg, Liang Z. Tan, Hsin-Zon Tsai, Youngkyou Kim, Jiong Lu, Aaron J. Bradley, Miguel M. Ugeda, Kacey L. Meaker, Kenji Watanabe, Takashi Taniguchi, Alex Zettl, Felix R. Fischer, Steven G. Louie, and Michael F. Crommie. Imaging and tuning molecular levels at the surface of a gated graphene device. *ACS Nano*, 8(6):5395–5401, 2014.

[66] Young-Woo Son, Marvin L. Cohen, and Steven G. Louie. Half-metallic graphene nanoribbons. *Nature*, 444(7117):347–349, 2006.

[67] Jonas Björk, Sven Stafström, and Felix Hanke. Zipping up: Cooperativity drives the synthesis of graphene nanoribbons. *Journal of the American Chemical Society*, 133(38):14884–14887, 2011.

[68] Woo Youn Kim and Kwang S. Kim. Prediction of very large values of magnetoresistance in a graphene nanoribbon device. *Nat Nano*, 3(7):408–412, 2008.

[69] Young-Kwan Kim and Dal-Hee Min. Durable large-area thin films of graphene/carbon nanotube double layers as a transparent electrode. *Langmuir*, 25(19):11302–11306, 2009.

[70] X. Hong, A. Posadas, K. Zou, C. H. Ahn, and J. Zhu. High-mobility few-layer graphene field effect transistors fabricated on epitaxial ferroelectric gate oxides. *Physical Review Letters*, 102(13):136808, 2009.

[71] Andrea Candini, Svetlana Klyatskaya, Mario Ruben, Wolfgang Wernsdorfer, and Marco Affronte. Graphene spintronic devices with molecular nanomagnets. *Nano Letters*, 11(7):2634–2639, 2011.

[72] Paolo Michetti and Patrik Recher. Spintronics devices from bilayer graphene in contact to ferromagnetic insulators. *Physical Review B*, 84(12):125438, 2011.

[73] David S. Hecht, Liangbing Hu, and Glen Irvin. Emerging transparent electrodes based on thin films of carbon nanotubes, graphene, and metallic nanostructures. *Advanced Materials*, 23(13):1482–1513, 2011.

[74] Rui Cheng, Jingwei Bai, Lei Liao, Hailong Zhou, Yu Chen, Lixin Liu, Yung-Chen Lin, Shan Jiang, Yu Huang, and Xiangfeng Duan. High-frequency self-aligned graphene transistors with transferred gate stacks. *Proceedings of the National Academy of Sciences*, 109(29):11588–11592, 2012.

[75] Frank Schwierz. Graphene transistors. *Nat Nano*, 5(7):487–496, 2010.

[76] Li Yang, Cheol-Hwan Park, Young-Woo Son, Marvin L. Cohen, and Steven G. Louie. Quasiparticle energies and band gaps in graphene nanoribbons. *Physical Review Letters*, 99(18):186801, 2007.

[77] Xiaoting Jia, Jessica Campos-Delgado, Mauricio Terrones, Vincent Meunier, and Mildred S. Dresselhaus. Graphene edges: a review of their fabrication and characterization. *Nanoscale*, 3(1):86–95, 2011.

[78] Vera Barone, Oded Hod, and Gustavo E. Scuseria. Electronic structure and stability of semiconducting graphene nanoribbons. *Nano Letters*, 6(12):2748–2754, 2006.

[79] Liying Jiao, Liming Xie, and Hongjie Dai. Densely aligned graphene nanoribbons at 35 nm pitch. *Nano Research*, 5(4):292–296, 2012.

[80] Sarah E. Bryan, Yinxiao Yang, and Raghunath Murali. Conductance of epitaxial graphene nanoribbons: Influence of size effects and substrate morphology. *Journal of Physical Chemistry C*, 115(20):10230–10235, 2011.

[81] Wan Sik Hwang, Pei Zhao, Kristof Tahy, Luke O. Nyakiti, Virginia D. Wheeler, Rachael L. Myers-Ward, Charles R. Eddy, D. Kurt Gaskill, Joshua A. Robinson, Wilfried Haensch, Huili (Grace) Xing, Alan Seabaugh, and Debdeep Jena. Graphene nanoribbon field-effect transistors on wafer-scale epitaxial graphene on sic substrates. *APL Materials*, 3(1):011101, 2015.

[82] Timothy H. Vo, Mikhail Shekhirev, Donna A. Kunkel, Martha D. Morton, Eric Berglund, Lingmei Kong, Peter M. Wilson, Peter A. Dowben, Axel Enders, and Alexander Sinitskii. Large-scale solution synthesis of narrow graphene nanoribbons. 5:3189, 2014.

[83] Zhong-Shuai Wu, Wencai Ren, Libo Gao, Bilu Liu, Jinping Zhao, and Hui-Ming Cheng. Efficient synthesis of graphene nanoribbons sonochemically cut from graphene sheets. *Nano Research*, 3(1):16–22, 2010.

[84] Dmitry V. Kosynkin, Amanda L. Higginbotham, Alexander Sinitskii, Jay R. Lomeda, Ayrat Dimiev, B. Katherine Price, and James M. Tour. Longitudinal unzipping of carbon nanotubes to form graphene nanoribbons. *Nature*, 458(7240):872–876, 2009.

[85] Chenggang Tao, Liying Jiao, Oleg V. Yazyev, Yen-Chia Chen, Juanjuan Feng, Xiaowei Zhang, Rodrigo B. Capaz, James M. Tour, Alex Zettl, Steven G. Louie, Hongjie Dai, and Michael F. Crommie. Spatially resolving edge states of chiral graphene nanoribbons. *Nature Physics*, 7(8):616–620, 2011.

[86] Abdirisak A. Isse, Armando Gennaro, Ching Yeh Lin, Jennifer L. Hodgson, Michelle L. Coote, and Tamaz Guliashvili. Mechanism of carbon-halogen bond reductive cleavage in activated alkyl halide initiators relevant to living radical polymerization: Theoretical and experimental study. *Journal of the American Chemical Society*, 133(16):6254–6264, 2011.

[87] Brian E. Bent, Ralph G. Nuzzo, Bernard R. Zegarski, and Lawrence H. Dubois. Thermal decomposition of alkyl halides on aluminum. 1. carbon-halogen bond cleavage and surface .beta.-hydride elimination reactions. *Journal of the American Chemical Society*, 113(4):1137–1142, 1991.

[88] Leif Lafferentz, Francisco Ample, Hao Yu, Stefan Hecht, Christian Joachim, and Leonhard Grill. Conductance of a single conjugated polymer as a continuous function of its length. *Science*, 323(5918):1193–1197, 2009.

[89] Christian Bombis, Francisco Ample, Leif Lafferentz, Hao Yu, Stefan Hecht, Christian Joachim, and Leonhard Grill. Single molecular wires connecting metallic and insulating surface areas. *Angewandte Chemie International Edition*, 48(52):9966–9970, 2009.

[90] James Briggs Hendrickson, Donald J. Cram, and George S. Hammond. *Organic chemistry*. McGraw-Hill, New York, 1970.

[91] Saw-Wai Hla, Ludwig Bartels, Gerhard Meyer, and Karl-Heinz Rieder. Inducing all steps of a chemical reaction with the scanning tunneling microscope tip: Towards single molecule engineering. *Physical Review Letters*, 85:2777–2780, 2000.

[92] LafferentzL., EberhardtV., DriC., AfrichC., ComelliG., EschF., HechtS., and GrillL. Controlling on-surface polymerization by hierarchical and substrate-directed growth. *Nature Chemistry*, 4(3):215–220, 2012.

[93] Marco Bieri, Manh-Thuong Nguyen, Oliver Gröning, Jinming Cai, Matthias Treier, Kamel Aït-Mansour, Pascal Ruffieux, Carlo A. Pignedoli, Daniele Passerone, Marcel Kastler, Klaus Müllen, and Roman Fasel. Two-dimensional polymer formation on surfaces: Insight into the roles of precursor mobility and reactivity. *Journal of the American Chemical Society*, 132(46):16669–16676, 2010.

[94] Serpil Boz, Meike Stöhr, Umut Soydaner, and Marcel Mayor. Protecting-group-controlled surface chemistry-organization and heat-induced coupling of 4,4;–di(tert-butoxycarbonylamino)biphenyl on metal surfaces. *Angewandte Chemie International Edition*, 48(17):3179–3183, 2009.

[95] Rico Gutzler, Hermann Walch, Georg Eder, Stephan Kloft, Wolfgang M. Heckl, and Markus Lackinger. Surface mediated synthesis of 2d covalent organic frameworks: 1,3,5-tris(4-bromophenyl)benzene on graphite(001), Cu(111), and Ag(110). *Chemical Communications*, (29):4456–4458, 2009.

[96] Mendel In't Veld, Patrizia Iavicoli, Sam Haq, David B. Amabilino, and Rasmita Raval. Unique intermolecular reaction of simple porphyrins at a metal surface gives covalent nanostructures. *Chemical Communications*, (13):1536–1538, 2008.

[97] Matthias Treier, Neville V. Richardson, and Roman Fasel. Fabrication of surface-supported low-dimensional polyimide networks. *Journal of the American Chemical Society*, 130(43):14054–14055, 2008.

[98] Masaki Hasegawa. Photopolymerization of diolefin crystals. *Chemical Reviews*, 83(5):507–518, 1983.

[99] Akikazu Matsumoto, Toru Odani, Kazuki Sada, Mikiji Miyata, and Kohji Tashiro. Intercalation of alkylamines into an organic polymer crystal. *Nature*, 405(6784):328–330, 2000.

[100] Yunfeng Lu, Yi Yang, Alan Sellinger, Mengcheng Lu, Jinman Huang, Hongyou Fan, Raid Haddad, Gabriel Lopez, Alan R. Burns, Darryl Y. Sasaki, John Shelnutt, and C. Jeffrey Brinker. Self-assembly of mesoscopically ordered chromatic polydiacetylene/silica nanocomposites. *Nature*, 410(6831):913–917, 2001.

[101] Shinji Nomura, Takahito Itoh, Hirofumi Nakasho, Takahiro Uno, Masataka Kubo, Kazuki Sada, Katsunari Inoue, and Mikiji Miyata. Crystal structures and topochemical polymerizations of 7,7,8,8-tetrakis(alkoxycarbonyl)quinodimethanes. *Journal of the American Chemical Society*, 126(7):2035–2041, 2004.

[102] Aiwu Sun, Joseph W. Lauher, and Nancy S. Goroff. Preparation of poly(diiododiacetylene), an ordered conjugated polymer of carbon and iodine. *Science*, 312(5776):1030, 2006.

[103] Joseph W. Lauher, Frank W. Fowler, and Nancy S. Goroff. Single-crystal-to-single-crystal topochemical polymerizations by design. *Accounts of Chemical Research*, 41(9):1215–1229, 2008.

[104] Priscilla Johnston, Carl Braybrook, and Kei Saito. Topochemical photo-reversible polymerization of a bioinspired monomer and its recovery and repolymerization after photo-depolymerization. *Chemical Science*, 3(7):2301–2306, 2012.

[105] Kumar Biradha and Ramkinkar Santra. Crystal engineering of topochemical solid state reactions. *Chemical Society Reviews*, 42(3):950–967, 2013.

[106] Letian Dou, Yonghao Zheng, Xiaoqin Shen, Guang Wu, Kirk Fields, Wan-Ching Hsu, Huanping Zhou, Yang Yang, and Fred Wudl. Single-crystal linear polymers through visible light-triggered topochemical quantitative polymerization. *Science*, 343(6168):272, 2014.

[107] X.-L. Zhou, X.-Y. Zhu, and J.M. White. Photochemistry at adsorbate/metal interfaces. *Surface Science Reports*, 13(3):73–220, 1991.

[108] X Zhu. Surface photochemistry. *Annual Review of Physical Chemistry*, 45(1):113–144, 1994.

[109] W Ho. Surface photochemistry. *Surface Science*, 299:996–1007, 1994.

[110] X.L. Zhou and J. M. White. Photon- and electron-induced chemistry of chlorobenzene on Ag(111). *The Journal of Chemical Physics*, 92(9):5612–5621, 1990.

[111] G.J. Szulczewski and J.M. White. Thermal and photon-stimulated reactions of iodobenzene on Ag(111). *Surface Science*, 399(2):305–315, 1998.

[112] M. J. Frisch et al. Gaussian 09 revision d.01. gaussian inc. wallingford ct. 2009.

[113] Moloy Sarkar and Anunay Samanta. 10,10′-Dibromo-9,9′-bianthryl. *Acta Crystallographica Section E*, 59(11):o1764–o1765, 2003.

[114] Christian Lotze and Nils Krane. Stm and afm measurements of DBBA on Au(111) in 2014 and 2015 in machine Aneto.

[115] Arijit Mukherjee, Srinu Tothadi, and Gautam R. Desiraju. Halogen bonds in crystal engineering: Like hydrogen bonds yet different. *Accounts of Chemical Research*, 47(8):2514–2524, 2014.

[116] ThaiThanhThu Bui, Slimane Dahaoui, Claude Lecomte, GautamR. Desiraju, and Enrique Espinosa. The nature of halogenhalogen interactions: A model derived from experimental charge-density analysis. *Angewandte Chemie International Edition*, 48(21):3838–3841, 2009.

[117] Peter Politzer, Jane S. Murray, and Timothy Clark. Halogen bonding: an electrostatically-driven highly directional noncovalent interaction. *Physical Chemistry Chemical Physics*, 12(28):7748–7757, 2010.

[118] Lydia C. Gilday, Sean W. Robinson, Timothy A. Barendt, Matthew J. Langton, Benjamin R. Mullaney, and Paul D. Beer. Halogen bonding in supramolecular chemistry. *Chemical Reviews*, 115(15):7118–7195, 2015.

[119] Han Huang, Zhiyu Tan, Yanwei He, Jian Liu, Jiatao Sun, Kang Zhao, Zhenhong Zhou, Guo Tian, Swee Liang Wong, and Andrew Thye Shen Wee. Competition between hexagonal and tetragonal hexabromobenzene packing on Au(111). *ACS Nano*, 10(3):3198–3205, 2016.

[120] F. Reinert, G. Nicolay, S. Schmidt, D. Ehm, and S. H"ufner. Direct measurements of the L-gap surface states on the (111) face of noble metals by photoelectron spectroscopy. *Physical Review B*, 63(11):115415, 2001.

[121] Ji-Yong Park, U. D. Ham, S.-J. Kahng, Y. Kuk, K. Miyake, K. Hata, and H. Shigekawa. Modification of surface-state dispersion upon xe adsorption: A scanning tunneling microscope study. *Physical Review B*, 62(24):R16341–R16344, 2000.

[122] Nicoleta Nicoara, Elisa Román, Josë M. Gómez-Rodrïguez, Josë A. Martïn-Gago, and Javier Mëndez. Scanning tunneling and photoemission spectroscopies at the ptcda/Au(111) interface. *Organic Electronics*, 7(5):287–294, 2006.

[123] F. Forster, G. Nicolay, F. Reinert, D. Ehm, S. Schmidt, and S. Hüfner. Surface and interface states on adsorbate covered noble metal surfaces. *Surface Science*, 532–535:160–165, 2003.

[124] Thomas Andreev, Ingo Barke, and Heinz Hövel. Adsorbed rare-gas layers on Au(111): Shift of the shockley surface state studied with ultraviolet photoelectron spectroscopy and scanning tunneling spectroscopy. *Physical Review B*, 70(20):205426, 2004.

[125] Jascha Repp, Gerhard Meyer, and Karl-Heinz Rieder. Snells law for surface electrons: Refraction of an electron gas imaged in real space. *Physical Review Letters*, 92:036803, 2004.

[126] A. Hotzel, G. Moos, K. Ishioka, M. Wolf, and G. Ertl. Femtosecond electron dynamics at adsorbate-metal interfaces and the dielectric continuum model. *Applied Physics B*, 68(3):615–622, 1999.

[127] N. V. Smith. Phase analysis of image states and surface states associated with nearly-free-electron band gaps. *Physical Review B*, 32(6):3549–3555, 1985.

[128] Karina Morgenstern, Kai-Felix Braun, and Karl-Heinz Rieder. Surface-state depopulation on small Ag(111) terraces. *Physical Review Letters*, 89(22):226801, 2002.

[129] Konstantin A. Simonov, Nikolay A. Vinogradov, Alexander S. Vinogradov, Alexander V. Generalov, Elena M. Zagrebina, Nils Mårtensson, Attilio A. Cafolla, Tomas Carpy, John P. Cunniffe, and Alexei B. Preobrajenski. Effect of substrate chemistry on the bottom-up fabrication of graphene nanoribbons: Combined core-level spectroscopy and stm study. *Journal of Physical Chemistry C*, 118(23):12532–12540, 2014.

[130] Arunabh Batra, Dean Cvetko, Gregor Kladnik, Olgun Adak, Claudia Cardoso, Andrea Ferretti, Deborah Prezzi, Elisa Molinari, Alberto Morgante, and Latha Venkataraman. Probing the mechanism for graphene nanoribbon formation on gold surfaces through X-ray spectroscopy. *Chemical Science*, 5(11):4419–4423, 2014.

[131] Xiaohui Li, Bin Li, Yongfei Ji, Jing Zhang, Aidi Zhao, and Bing Wang. Adsorption and self-assembly of the 2,3,5,6-tetra(2'-pyridyl)pyrazine nonplanar molecule on a Au(111) surface. *Journal of Physical Chemistry C*, 120(11):6039–6049, 2016.

[132] Konstantin A. Simonov, Nikolay A. Vinogradov, Alexander S. Vinogradov, Alexander V. Generalov, Elena M. Zagrebina, Nils Martensson, Attilio A. Cafolla, Thomas Carpy, John P. Cunniffe, and Alexei B. Preobrajenski. Comment on bottom-up graphene-nanoribbon fabrication reveals chiral edges and enantioselectivity. *ACS Nano*, 9(4):3399–3403, 2015.

[133] Marco Smerieri, Igor Pis, Lara Ferrighi, Silvia Nappini, Angelique Lusuan, Cristiana Di Valentin, Luca Vaghi, Antonio Papagni, Mattia Cattelan, Stefano Agnoli, Elena Magnano, Federica Bondino, and Letizia Savio. Synthesis of graphene nanoribbons with a defined mixed edge-site sequence by surface assisted polymerization of (1,6)-dibromopyrene on Ag(110). *Nanoscale*, 8(41):17843–17853, 2016.

[134] Michael Klues, Klaus Hermann, and Gregor Witte. Analysis of the near-edge X-ray-absorption fine-structure of anthracene: A combined theoretical and experimental study. *The Journal of Chemical Physics*, 140(1), 2014.

[135] Stephan Blankenburg, Jinming Cai, Pascal Ruffieux, Rached Jaafar, Daniele Passerone, Xinliang Feng, Klaus Müllen, Roman Fasel, and Carlo A. Pignedoli. Intraribbon heterojunction formation in ultranarrow graphene nanoribbons. *ACS Nano*, 6(3):2020–2025, 2012.

[136] Han Huang, Dacheng Wei, Jiatao Sun, Swee Liang Wong, Yuan Ping Feng, A. H. Castro Neto, and Andrew Thye Shen Wee. Spatially resolved electronic structures of atomically precise armchair graphene nanoribbons. *Scientific Reports*, 2:983, 2012.

[137] We-Hyo Soe, Hon Seng Wong, Carlos Manzano, Maricarmen Grisolia, Mohamed Hliwa, Xinliang Feng, Klaus Müllen, and Christian Joachim. Mapping the excited states of single hexa-peri-benzocoronene oligomers. *ACS Nano*, 6(4):3230–3235, 2012.

[138] S. Linden, D. Zhong, A. Timmer, N. Aghdassi, J. H. Franke, H. Zhang, X. Feng, K. M'ullen, H. Fuchs, L. Chi, and H. Zacharias. Electronic structure of spatially aligned graphene nanoribbons on Au(788). *Physical Review Letters*, 108(21):216801, 2012.

[139] Christopher Bronner. Photoinduced and thermal reactions of functional molecules at surfaces. *PhD thesis*, 2014.

[140] Jacques Cousty and Alexandr Marchenko. Substrate-induced freezing of alkane monolayers adsorbed on Au(1 1 1) dependant on the alkane/gold misfit. *Surface Science*, 520(3):128–136, 2002.

[141] Bas Hulsken, Johannes A A W Elemans, Jan W Gerritsen, Tony Khoury, Maxwell J Crossley, Alan E Rowan, Roeland J M Nolte, and Sylvia Speller. STM studies of the self-assembly of manganese porphyrin catalysts at the Au(111)-n-tetradecane interface. *New Journal of Physics*, 11(8):083011, 2009.

[142] O. Marchenko and J. Cousty. Molecule length-induced reentrant self-organization of alkanes in monolayers adsorbed on Au(111). *Physical Review Letters*, 84(23):5363–5366, 2000.

[143] R. Yamada and K. Uosaki. Two-dimensional crystals of alkanes formed on Au(111) surface in neat liquid: Structural investigation by scanning tunneling microscopy. *Journal of Physical Chemistry B*, 104(25):6021–6027, 2000.

[144] Christopher L. Claypool, Francesco Faglioni, William A. Goddard, Harry B. Gray, Nathan S. Lewis, and R. A. Marcus. Source of image contrast in stm images of functionalized alkanes on graphite: a systematic functional group approach. *Journal of Physical Chemistry B*, 101(31):5978–5995, 1997.

[145] Bin Wu, Dechao Geng, Yunlong Guo, Liping Huang, Yunzhou Xue, Jian Zheng, Jianyi Chen, Gui Yu, Yunqi Liu, Lang Jiang, and Wenping Hu. Equiangular hexagon-shape-controlled synthesis of graphene on copper surface. *Advanced Materials*, 23(31):3522–3525, 2011.

[146] Tomoki Uehara, Rodion V. Belosludov, Amir A. Farajian, Hiroshi Mizuseki, and Yoshiyuki Kawazoe. Electronic and transport properties of ferrocene: Theoretical study. *Japanese Journal of Applied Physics*, 45(4S):3768, 2006.

[147] Yachao Zhang and Mingsen Deng. Electrical control of spin states of ferrocene on Cu(111). *Journal of Physical Chemistry C*, 119(37):21681–21687, 2015.

[148] Duval Mbongo Djimbi, Sëbastien Le Roux, Carlo Massobrio, and Mauro Boero. Metalorganic moleculemetal nano-junctions: a close contact between first-principles simulations and experiments. *Journal of Physics: Condensed Matter*, 26(10):104206, 2014.

[149] Islamshah Amlani, Alexei O. Orlov, Geza Toth, Gary H. Bernstein, Craig S. Lent, and Gregory L. Snider. Digital logic gate using quantum-dot cellular automata. *Science*, 284(5412):289, 1999.

[150] Yuhui Lu and Craig S Lent. A metric for characterizing the bistability of molecular quantum-dot cellular automata. *Nanotechnology*, 19(15):155703, 2008.

[151] A. O. Orlov, I. Amlani, G. H. Bernstein, C. S. Lent, and G. L. Snider. Realization of a functional cell for quantum-dot cellular automata. *Science*, 277(5328):928, 1997.

[152] Maider Ormaza, Paula Abufager, Nicolas Bachellier, Roberto Robles, Martin Verot, Tangui Le Bahers, Marie-Laure Bocquet, Nicolas Lorente, and Laurent Limot. Assembly of ferrocene molecules on metal surfaces revisited. *Journal of Physical Chemistry Letters*, 6(3):395–400, 2015.

[153] K.-F. Braun, V. Iancu, N. Pertaya, K.-H. Rieder, and S.-W. Hla. Decompositional incommensurate growth of ferrocene molecules on a Au(111) surface. *Physical Review Letters*, 96(24):246102, 2006.

[154] C. Waldfried, D. Welipitiya, C. W. Hutchings, H. S. V. de Silva, G. A. Gallup, P. A. Dowben, W. W. Pai, Jiandi Zhang, J. F. Wendelken, and N. M. Boag. Preferential bonding orientations of ferrocene on surfaces. *Journal of Physical Chemistry B*, 101(47):9782–9789, 1997.

[155] Dulip Welipitiya, P.A. Dowben, Jiandi Zhang, W.W. Pai, and J.F. Wendelken. The adsorption and desorption of ferrocene on Ag(100). *Surface Science*, 367(1):20–32, 1996.

[156] C. M. Woodbridge, D. L. Pugmire, R. C. Johnson, N. M. Boag, and M. A. Langell. Hreels and xps studies of ferrocene on Ag(100). *Journal of Physical Chemistry B*, 104(14):3085–3093, 2000.

[157] P.J. Durston and R.E. Palmer. Adsorption and decomposition of ferrocene on graphite studied by hreels and stm. *Surface Science*, 400(1):277–280, 1998.

[158] Johannes V. Barth, Giovanni Costantini, and Klaus Kern. Engineering atomic and molecular nanostructures at surfaces. *Nature*, 437(7059):671–679, 2005.

[159] Pietro Gambardella, Sebastian Stepanow, Alexandre Dmitriev, Jan Honolka, Frank M. F. de Groot, Magali Lingenfelder, Subhra Sen Gupta, D. D. Sarma, Peter Bencok, Stefan Stanescu, Sylvain Clair, Stephane Pons, Nian Lin, Ari P. Seitsonen, Harald Brune, Johannes V. Barth, and Klaus Kern. Supramolecular control of the magnetic anisotropy in two-dimensional high-spin fe arrays at a metal interface. *Nat Mater*, 8(3):189–193, 2009.

[160] Ludwig Bartels. Tailoring molecular layers at metal surfaces. *Nature Chemistry*, 2(2):87–95, 2010.

[161] Prithwidip Saha, Khushboo Yadav, Shibin Chacko, Anijamol T. Philip, Ramesh Ramapanicker, and Thiruvancheril G. Gopakumar. Controlling growth to one dimension in nanoislands of ferrocene-sugar derivatives. *Journal of Physical Chemistry C*, 120(17):9223–9228, 2016.

[162] Sebastian Stepanow, Magali Lingenfelder, Alexandre Dmitriev, Hannes Spillmann, Erik Delvigne, Nian Lin, Xiaobin Deng, Chengzhi Cai, Johannes V. Barth, and Klaus Kern. Steering molecular organization and host-guest interactions using two-dimensional nanoporous coordination systems. *Nat Mater*, 3(4):229–233, 2004.

[163] Hee K. Chae, Diana Y. Siberio-Perez, Jaheon Kim, YongBok Go, Mohamed Eddaoudi, Adam J. Matzger, Michael O'Keeffe, and Omar M. Yaghi. A route to high surface area, porosity and inclusion of large molecules in crystals. *Nature*, 427(6974):523–527, 2004.

[164] Natalie A. Wasio, Rebecca C. Quardokus, Ryan P. Forrest, Craig S. Lent, Steven A. Corcelli, John A. Christie, Kenneth W. Henderson, and S. Alex Kandel. Self-assembly of hydrogen-bonded two-dimensional quasicrystals. *Nature*, 507(7490):86–89, 2014.

[165] Narges Mohammadi, Aravindhan Ganesan, Christopher T. Chantler, and Feng Wang. Differentiation of ferrocene d5d and d5h conformers using ir spectroscopy. *Journal of Organometallic Chemistry*, 713:51–59, 2012.

[166] Arne Haaland and Jan-Erik Nilsson. The determination of the barrier to internal rotation in ferrocene and ruthenocene by means of electron diffraction. *Chemical Communications (London)*, (2):88–89, 1968.

[167] Sonia Coriani, Arne Haaland, Trygve Helgaker, and Poul Jørgensen. The equilibrium structure of ferrocene. *ChemPhysChem*, 7(1):245–249, 2006.

[168] J. D. Dunitz, L. E. Orgel, and A. Rich. The crystal structure of ferrocene. *Acta Crystallographica*, 9(4):373–375, 1956.

[169] Gus J. Palenik. Crystal and molecular structure of ferrocenedicarboxylic acid. *Inorganic Chemistry*, 8(12):2744–2749, 1969.

[170] F. Takusagawa and T. F. Koetzle. The crystal and molecular structure of 1,1'-ferrocenedicarboxylic acid (triclinic modification): neutron and X-ray diffraction studies at 78 K and 298 K. *Acta Crystallographica Section B*, 35(12):2888–2896, 1979.

[171] Dario Braga, Marco Polito, Daniela D'Addario, and Fabrizia Grepioni. Polymorphism of molecular organometallic crystals. a third form of the supramolecular hydrogen-bonded dimer [FeII(5-C5H4COOH)2]2. *Crystal Growth & Design*, 4(6):1109–1112, 2004.

[172] Zhen-Feng Xu, Yaoming Xie, Wen-Lin Feng, and Henry F. Schaefer. Systematic investigation of electronic and molecular structures for the first transition metal series metallocenes m(c5h5)2 (m = v, cr, mn, fe, co, and ni). *The Journal of Physical Chemistry A*, 107(15):2716–2729, 2003.

[173] Marcel Swart. Metal-ligand bonding in metallocenes: Differentiation between spin state, electrostatic and covalent bonding. *Inorganica Chimica Acta*, 360(1):179–189, 2007.

[174] B. W. Heinrich, L. Limot, M. V. Rastei, C. Iacovita, J. P. Bucher, Duval Mbongo Djimbi, Carlo Massobrio, and Mauro Boero. Dispersion and localization of electronic states at a ferrocene/Cu(111) interface. *Physical Review Letters*, 107(21):216801, 2011.

[175] J. Berger, K. Košmider, O. Stetsovych, M. Vondráček, P. Hapala, E. J. Spadafora, M. Švec, and P. Jelínek. Study of ferrocene dicarboxylic acid on substrates of varying chemical activity. *Journal of Physical Chemistry C*, pages –, 2016.

[176] N. Bachellier, M. Ormaza, M. Faraggi, B. Verlhac, M. Vérot, T. Le Bahers, M.-L. Bocquet, and L. Limot. Unveiling nickelocene bonding to a noble metal surface. *Physical Review B*, 93(19):195403, 2016.

[177] Maider Ormaza, Roberto Robles, Nicolas Bachellier, Paula Abufager, Nicolás Lorente, and Laurent Limot. On-surface engineering of a magnetic organometallic nanowire. *Nano Letters*, 16(1):588–593, 2016.

[178] M. E. Cañas-Ventura, F. Klappenberger, S. Clair, S. Pons, K. Kern, H. Brune, T. Strunskus, Ch. Wöll, R. Fasel, and J. V. Barth. Coexistence of one- and two-dimensional supramolecular assemblies of terephthalic acid on Pd(111) due to self-limiting deprotonation. *The Journal of Chemical Physics*, 125(18), 2006.

[179] M. N. Faraggi, C. Rogero, A. Arnau, M. Trelka, D. Écija, C. Isvoranu, J. Schnadt, C. Marti-Gastaldo, E. Coronado, J. M. Gallego, R. Otero, and R. Miranda. Role of deprotonation and cu adatom migration in determining the reaction pathways of oxalic acid adsorption on Cu(111). *Journal of Physical Chemistry C*, 115(43):21177–21182, 2011.

[180] L. Kanninen, N. Jokinen, H. Ali-Löytty, P. Jussila, K. Lahtonen, M. Hirsimäki, M. Valden, M. Kuzmin, R. Pärna, and E. Nõmmiste. Adsorption structure and bonding of trimesic acid on Cu(100). *Surface Science*, 605(23–24):1968–1978, 2011.

[181] Nian Lin, Alexandre Dmitriev, Jens Weckesser, Johannes V. Barth, and Klaus Kern. Real-time single-molecule imaging of the formation and dynamics of coordination compounds. *Angewandte Chemie International Edition*, 41(24):4779–4783, 2002.

[182] Manfred Matena, Meike Stöhr, Till Riehm, Jonas Björk, Susanne Martens, Matthew S. Dyer, Mats Persson, Jorge Lobo-Checa, Kathrin Müller, Mihaela Enache, Hubert Wadepohl, Jörg Zegenhagen, Thomas A. Jung, and Lutz H. Gade. Aggregation and contingent metal/surface reactivity of 1,3,8,10-tetraazaperopyrene (tapp) on Cu(111). *Chemistry A European Journal*, 16(7):2079–2091, 2010.

[183] Tugce Eralp, Andrey Shavorskiy, Zhasmina V. Zheleva, Georg Held, Nataliya Kalashnyk, Yanxiao Ning, and Trolle R. Linderoth. Global and local expression of chirality in serine on the cu110 surface. *Langmuir*, 26(24):18841–18851, 2010.

[184] Vincent Humblot, Christophe Méthivier, Rasmita Raval, and Claire-Marie Pradier. Amino acid and peptides on Cu(110) surfaces: Chemical and structural analyses of l-lysine. *Surface Science*, 601(18):4189–4194, 2007.

[185] Fabian Bebensee, Katrine Svane, Christian Bombis, Federico Masini, Svetlana Klyatskaya, Flemming Besenbacher, Mario Ruben, Bjork Hammer, and Trolle Linderoth. Adsorption and dehydrogenation of tetrahydroxybenzene on Cu(111). *Chemical Communications*, 49(81):9308–9310, 2013.

[186] Johannes A. A. W. Elemans, Shengbin Lei, and Steven De Feyter. Molecular and supramolecular networks on surfaces: From two-dimensional crystal engineering to reactivity. *Angewandte Chemie International Edition*, 48(40):7298–7332, 2009.

[187] Mario Ruben, Dietmar Payer, Aitor Landa, Alessio Comisso, Chiara Gattinoni, Nian Lin, Jean-Paul Collin, Jean-Pierre Sauvage, Alessandro De Vita, and Klaus Kern. 2d supramolecular assemblies of benzene-1,3,5-triyl-tribenzoic acid: temperature-induced phase transformations and hierarchical organization with macrocyclic molecules. *Journal of the American Chemical Society*, 128(49):15644–15651, 2006.

[188] S. Stepanow, T. Strunskus, M. Lingenfelder, A. Dmitriev, H. Spillmann, N. Lin, J. V. Barth, Ch. Wöll, and K. Kern. Deprotonation-driven phase transformations in terephthalic acid self-assembly on Cu(100). *Journal of Physical Chemistry B*, 108(50):19392–19397, 2004.

[189] Dingyong Zhong, Katrin Wedeking, Tobias Blömker, Gerhard Erker, Harald Fuchs, and Lifeng Chi. Multilevel supramolecular architectures self-assembled on metal surfaces. *ACS Nano*, 4(4):1997–2002, 2010.

[190] Jiutao Li, Wolf-Dieter Schneider, Richard Berndt, O. R. Bryant, and S. Crampin. Surface-state lifetime measured by scanning tunneling spectroscopy. *Physical Review Letters*, 81(20):4464–4467, 1998.

[191] O. Jeandupeux, L. B´urgi, A. Hirstein, H. Brune, and K. Kern. Thermal damping of quantum interference patterns of surface-state electrons. *Physical Review B*, 59(24):15926–15934, 1999.

[192] J. Kliewer, R. Berndt, E. V. Chulkov, V. M. Silkin, P. M. Echenique, and S. Crampin. Dimensionality effects in the lifetime of surface states. *Science*, 288(5470):1399, 2000.

[193] Nicoleta Nicoara, Elisa Román, José M. Gómez-Rodríguez, José A. Martín-Gago, and Javier Méndez. Scanning tunneling and photoemission spectroscopies at the ptcda/Au(111) interface. *Organic Electronics*, 7(5):287–294, 2006.

[194] D. B. Dougherty, P. Maksymovych, J. Lee, and J. T. Yates. Local spectroscopy of image-potential-derived states: From single molecules to monolayers of benzene on Cu(111). *Physical Review Letters*, 97(23):236806, 2006.

[195] A. Scheybal, K. M´uller, R. Bertschinger, M. Wahl, A. Bendounan, P. Aebi, and T. A. Jung. Modification of the cu(110) shockley surface state by an adsorbed pentacene monolayer. *Physical Review B*, 79(11):115406, 2009.

[196] Geoffrey Rojas, Scott Simpson, Xumin Chen, Donna A. Kunkel, Justin Nitz, Jie Xiao, Peter A. Dowben, Eva Zurek, and Axel Enders. Surface state engineering of molecule-molecule interactions. *Physical Chemistry Chemical Physics*, 14(14):4971–4976, 2012.

[197] Anna G. Slater (nee Phillips), Peter H. Beton, and Neil R. Champness. Two-dimensional supramolecular chemistry on surfaces. *Chemical Science*, 2(8):1440–1448, 2011.

[198] Johannes V. Barth. Molecular architectonic on metal surfaces. *Annual Review of Physical Chemistry*, 58(1):375–407, 2007.

[199] Krishna G. Nath, Oleksandr Ivasenko, Jennifer M. MacLeod, Jill A. Miwa, James D. Wuest, Antonio Nanci, Dmitrii F. Perepichka, and Federico Rosei. Crystal engineering in two dimensions: An approach to molecular nanopatterning. *Journal of Physical Chemistry C*, 111(45):16996–17007, 2007.

[200] Markus Lackinger. Self-healing in two-dimensional supramolecular structures. In *Self-Healing at the Nanoscale*, pages 91–116–. CRC Press, December 2011.

[201] Takayuki Suzuki, Theresa Lutz, Dietmar Payer, Nian Lin, Steven L. Tait, Giovanni Costantini, and Klaus Kern. Substrate effect on supramolecular self-assembly: from semiconductors to metals. *Physical Chemistry Chemical Physics*, 11(30):6498–6504, 2009.

[202] Matthew O. Blunt, James C. Russell, María del Carmen Giménez-López, Juan P. Garrahan, Xiang Lin, Martin Schróder, Neil R. Champness, and Peter H. Beton. Random tiling and topological defects in a two-dimensional molecular network. *Science*, 322(5904):1077, 2008.

[203] Jennifer M. MacLeod, Zied Ben Chaouch, Dmitrii F. Perepichka, and Federico Rosei. Two-dimensional self-assembly of a symmetry-reduced tricarboxylic acid. *Langmuir*, 29(24):7318–7324, 2013.

[204] D. S. Martin, R. J. Cole, and S. Haq. Creating a functionalized surface: The adsorption of terephthalic acid onto Cu(110). *Physical Review B*, 66(15):155427, 2002.

[205] A. Dmitriev, N. Lin, J. Weckesser, J. V. Barth, and K. Kern. Supramolecular assemblies of trimesic acid on a Cu(100) surface. *Journal of Physical Chemistry B*, 106(27):6907–6912, 2002.

[206] B.G. Frederick, Q. Chen, F.M. Leibsle, M.B. Lee, K.J. Kitching, and N.V. Richardson. Long-range periodicity in c(8×2) benzoate/Cu(110): a combined stm, leed and hreels study. *Surface Science*, 394(1):1–25, 1997.

[207] Q. Chen, C.C. Perry, B.G. Frederick, P.W. Murray, S. Haq, and N.V. Richardson. Structural aspects of the low-temperature deprotonation of benzoic acid on Cu(110) surfaces. *Surface Science*, 446:63–75, 2000.

[208] Dietmar Payer, Alessio Comisso, Alexandre Dmitriev, Thomas Strunskus, Christof Barth, Johannes Wóll, Alessandro DeVita, Johannes V.V. Barth, and Klaus Kern. Ionic hydrogen bonds controlling two-dimensional supramolecular systems at a metal surface. *Chemistry A European Journal*, 13(14):3900–3906, 2007.

[209] Steven L. Tait, Hyuna Lim, Arjun Theertham, and Peter Seidel. First layer compression and transition to standing second layer of terephthalic acid on Cu(100). *Physical Chemistry Chemical Physics*, 14(22):8217–8223, 2012.

[210] Yan Ge, Hilmar Adler, Arjun Theertham, Larry L. Kesmodel, and Steven L. Tait. Adsorption and bonding of first layer and bilayer terephthalic acid on the Cu(100) surface by high-resolution electron energy loss spectroscopy. *Langmuir*, 26(21):16325–16329, 2010.

[211] C.C. Perry, S. Haq, B.G. Frederick, and N.V. Richardson. Face specificity and the role of metal adatoms in molecular reorientation at surfaces. *Surface Science*, 409(3):512–520, 1998.

[212] D.P. Woodruff, C.F. McConville, A.L.D. Kilcoyne, Th. Lindner, J. Somers, M. Surman, G. Paolucci, and A.M. Bradshaw. The structure of the formate species on copper surfaces: new photoelectron diffraction results and sexafs data reassessed. *Surface Science*, 201(1):228–244, 1988.

[213] T. S. Jones, M. R. Ashton, and N. V. Richardson. An electron energy loss study of the surface formate species chemisorbed on Ni(110): Dipole, impact, and resonance scattering for adsorbate covered surfaces. *The Journal of Chemical Physics*, 90(12):7564–7576, 1989.

[214] K.-U. Weiss, R. Dippel, K.-M. Schindler, P. Gardner, V. Fritzsche, A. M. Bradshaw, A. L. D. Kilcoyne, and D. P. Woodruff. Chemical shift photoelectron diffraction from molecular adsorbates. *Physical Review Letters*, 69(22):3196–3199, 1992.

[215] A. Sotiropoulos, P.K. Milligan, B.C.C. Cowie, and M. Kadodwala. A structural study of formate on Cu(111). *Surface Science*, 444:52–60, 2000.

[216] Izabela Cebula, Hao Lu, Michael Zharnikov, and Manfred Buck. Monolayers of trimesic and isophthalic acid on cu and ag: the influence of coordination strength on adsorption geometry. *Chemical Science*, 4(12):4455–4464, 2013.

[217] Hannah Aitchison, Hao Lu, Michael Zharnikov, and Manfred Buck. Monolayers of biphenyl-3,4',5-tricarboxylic acid formed on cu and ag from solution. *Journal of Physical Chemistry C*, 119(25):14114–14125, 2015.

[218] Thomas Classen, Magalí Lingenfelder, Yeliang Wang, Rishav Chopra, Chariya Virojanadara, Ulrich Starke, Giovanni Costantini, Guido Fratesi, Stefano Fabris, Stefano de Gironcoli, Stefano Baroni, Sam Haq, Rasmita Raval, and Klaus Kern. Hydrogen and coordination bonding supramolecular structures of trimesic acid on Cu(110). *The Journal of Physical Chemistry A*, 111(49):12589–12603, 2007.

[219] Lawrence H. Dubois, Bernard R. Zegarski, and Ralph G. Nuzzo. Spontaneous organization of carboxylic acid monolayer films in ultrahigh vacuum. kinetic constraints to assembly via gas-phase adsorption. *Langmuir*, 2(4):412–417, 1986.

[220] Paolo Messina, Alexandre Dmitriev, Nian Lin, Hannes Spillmann, Mathieu Abel, Johannes V. Barth, and Klaus Kern. Direct observation of chiral metal-organic complexes assembled on a Cu(100) surface. *Journal of the American Chemical Society*, 124(47):14000–14001, 2002.

[221] Dario Braga, Lucia Maini, Fabrizia Grepioni, Christoph Elschenbroich, Francesca Paganelli, and Olav Schiemann. Novel Organometallic Building Blocks for Crystal Engineering. Synthesis and Structural Characterization of the Dicarboxylic Acid $[Cr^0(\eta^6\text{-}C_6H_5COOH)_2]$, of Two Polymorphs of Its Oxidation Derivative $[Cr^I(\eta^6\text{-}C_6H_5COOH)_2]^+[PF_6]^-$, and of the Zwitterionic Form $[Cr^I(\eta^6\text{-}C_6H_5COOH)(\eta^6\text{-}C_6H_5COO)]$. *Organometallics*, 20(9):1875–1881, 2001.

[222] M. Wuhn, J. Weckesser, and Ch. Woll. Bonding and orientational ordering of long-chain carboxylic acids on Cu(111): Investigations using X-ray absorption spectroscopy. *Langmuir*, 17(24):7605–7612, 2001.

[223] Mahdi Sadeghzadeh Baviloliaei and Lars Diekhoner. Molecular self-assembly at nanometer scale modulated surfaces: trimesic acid on Ag(111), Cu(111) and Ag/Cu(111). *Physical Chemistry Chemical Physics*, 16(23):11265–11269, 2014.

[224] B.G. Frederick, M.R. Ashton, N.V. Richardson, and T.S. Jones. Orientation and bonding of benzoic acid, phthalic anhydride and pyromellitic dianhydride on Cu(110). *Surface Science*, 292(1):33–46, 1993.

[225] Lawrence H. Dubois, Bernard R. Zegarski, and Ralph G. Nuzzo. Spontaneous organization of carboxylic acid monolayer films in ultrahigh vacuum. kinetic constraints to assembly via gas-phase adsorption. *Langmuir*, 2(4):412–417, 1986.

[226] Noel T. Southall, Ken A. Dill, and A. D. J. Haymet. A view of the hydrophobic effect. *Journal of Physical Chemistry B*, 106(3):521–533, 2002.

[227] Emmanuel A. Meyer, Ronald K. Castellano, and François Diederich. Interactions with aromatic rings in chemical and biological recognition. *Angewandte Chemie International Edition*, 42(11):1210–1250, 2003.

[228] Dieter Schollmeyer, Oleg V. Shishkin, Thomas Ruhl, and Myroslav O. Vysotsky. Oh-[small pi] and halogen-[small pi] interactions as driving forces in the crystal organisations of tri-bromo and tri-iodo trityl alcohols. *CrystEngComm*, 10(6):715–723, 2008.

[229] Michel Mons, Evan G. Robertson, and John P. Simons. Intra- and intermolecular π-type hydrogen bonding in aryl alcohols: Uv and ir-uv ion dip spectroscopy. *The Journal of Physical Chemistry A*, 104(7):1430–1437, 2000.

[230] Seiji Tsuzuki, Kazumasa Honda, Tadafumi Uchimaru, Masuhiro Mikami, and Kazutoshi Tanabe. Origin of the attraction and directionality of the nh/π interaction: Comparison with oh/π and ch/π interactions. *Journal of the American Chemical Society*, 122(46):11450–11458, 2000.

[231] K. Le Barbu, F. Lahmani, M. Mons, M. Broquier, and A. Zehnacker. Ir-uv investigation of the structure of the 1-phenylethanol chromophore and its hydrated complexes. *Physical Chemistry Chemical Physics*, 3(21):4684–4688, 2001.

[232] Benjamin J. Miller, Henrik G. Kjaergaard, Kaori Hattori, Shun-ichi Ishiuchi, and Masaaki Fujii. The most stable conformer of benzyl alcohol. *Chemical Physics Letters*, 466:21–26, 2008.

[233] Xun-Wang Yan, Zhong-Bing Huang, Guo-Hua Zhong, and Hai-Qing Lin. Pressure-induced ferromagnetic half-metallicity in cobaltocene. *EPL (Europhysics Letters)*, 113(2):27005, 2016.

[234] Jose A. M. Dinglasan, Michael Bailey, Jong B. Park, and Al-Amin Dhirani. Differential conductance switching of planar tunnel junctions mediated by oxidation/reduction of functionally protected ferrocene. *Journal of the American Chemical Society*, 126(20):6491–6497, 2004.

[235] Micol Alemani, Sofia Selvanathan, Francisco Ample, Maike V. Peters, Karl-Heinz Rieder, Francesca Moresco, Christian Joachim, Stefan Hecht, and Leonhard Grill. Adsorption and switching properties of azobenzene derivatives on different noble metal surfaces: Au(111), Cu(111), and Au(100). *Journal of Physical Chemistry C*, 112(28):10509–10514, 2008.

[236] Philipp Rahe, Ryan P. Steele, and Clayton C. Williams. Consecutive charging of a molecule-on-insulator ensemble using single electron tunnelling methods. *Nano Letters*, 16(2):911–916, 2016.

[237] N. Néel, L. Limot, J. Kröger, and R. Berndt. Rotation of C60 in a single-molecule contact. *Physical Review B*, 77:125431, 2008.

[238] Karl-Heinz Ernst. Molecular motors: A turn in the right direction. *Nat Nano*, 8(1):7–8, 2013.

[239] A. Charrier, A. Coati, T. Argunova, F. Thibaudau, Y. Garreau, R. Pinchaux, I. Forbeaux, J.-M. Debever, M. Sauvage-Simkin, and J.-M. Themlin. Solid-state decomposition of silicon carbide for growing ultra-thin heteroepitaxial graphite films. *Journal of Applied Physics*, 92(5):2479–2484, 2002.

[240] S. Marchini, S. Gunther, and J. Wintterlin. Scanning tunneling microscopy of graphene on Ru(0001). *Physical Review B*, 76(7):075429, 2007.

[241] Jiong Lu, Pei Shan Emmeline Yeo, Chee Kwan Gan, Ping Wu, and Kian Ping Loh. Transforming C60 molecules into graphene quantum dots. *Nat Nano*, 6(4):247–252, 2011.

[242] Luís M.A. Perdigão, Syarifah N. Sabki, Jason M. Garfitt, Pierre Capiod, and Peter H. Beton. Graphene formation by decomposition of C60. *Journal of Physical Chemistry C*, 115(15):7472–7476, 2011.

[243] Pablo Merino, Martin Švec, Anna L. Pinardi, Gonzalo Otero, and José A. Martín-Gago. Strain-driven moiré superstructures of epitaxial graphene on transition metal surfaces. *ACS Nano*, 5(7):5627–5634, 2011.

[244] L. Zhao, K.T. Rim, H. Zhou, R. He, T.F. Heinz, A. Pinczuk, G.W. Flynn, and A.N. Pasupathy. Influence of copper crystal surface on the cvd growth of large area monolayer graphene. *Solid State Communications*, 151(7):509–513, 2011.

[245] Cristina Gómez-Navarro, R. Thomas Weitz, Alexander M. Bittner, Matteo Scolari, Alf Mews, Marko Burghard, and Klaus Kern. Electronic transport properties of individual chemically reduced graphene oxide sheets. *Nano Letters*, 7(11):3499–3503, 2007.

[246] Claire Berger, Zhimin Song, Tianbo Li, Xuebin Li, Asmerom Y. Ogbazghi, Rui Feng, Zhenting Dai, Alexei N. Marchenkov, Edward H. Conrad, Phillip N. First, and Walt A. de Heer. Ultrathin epitaxial graphite: 2d electron gas properties and a route toward graphene-based nanoelectronics. *Journal of Physical Chemistry B*, 108(52):19912–19916, 2004.

[247] I. Brihuega, P. Mallet, C. Bena, S. Bose, C. Michaelis, L. Vitali, F. Varchon, L. Magaud, K. Kern, and J. Y. Veuillen. Quasiparticle chirality in epitaxial graphene probed at the nanometer scale. *Physical Review Letters*, 101(20):206802, 2008.

[248] Nan Liu, Lei Fu, Boya Dai, Kai Yan, Xun Liu, Ruiqi Zhao, Yanfeng Zhang, and Zhongfan Liu. Universal segregation growth approach to wafer-size graphene from non-noble metals. *Nano Letters*, 11(1):297–303, 2011.

[249] Shaahin Amini, Javier Garay, Guanxiong Liu, Alexander A. Balandin, and Reza Abbaschian. Growth of large-area graphene films from metal-carbon melts. *Journal of Applied Physics*, 108(9):094321, 2010.

[250] J. Wintterlin and M.-L. Bocquet. Graphene on metal surfaces. *Surface Science*, 603(10):1841–1852, 2009.

[251] Johann Coraux, Alpha T. N'Diaye, Carsten Busse, and Thomas Michely. Structural coherency of graphene on Ir(111). *Nano Letters*, 8(2):565–570, 2008.

[252] Li Gao, Jeffrey R. Guest, and Nathan P. Guisinger. Epitaxial graphene on Cu(111). *Nano Letters*, 10(9):3512–3516, 2010.

[253] Xuesong Li, Weiwei Cai, Jinho An, Seyoung Kim, Junghyo Nah, Dongxing Yang, Richard Piner, Aruna Velamakanni, Inhwa Jung, Emanuel Tutuc, Sanjay K. Banerjee, Luigi Colombo, and Rodney S. Ruoff. Large-area synthesis of high-quality and uniform graphene films on copper foils. *Science*, 324(5932):1312, 2009.

[254] Antonio J. Martínez-Galera, Iván Brihuega, and José. Gómez-Rodríguez. Ethylene irradiation: A new route to grow graphene on low reactivity metals. *Nano Letters*, 11(9):3576–3580, 2011.

[255] Cechan Tian and C.R Vidal. Cross sections of electron impact ionization of ethylene. *Chemical Physics Letters*, 288:499–503, 1998.

[256] R Komanduri and Z.B Hou. A review of the experimental techniques for the measurement of heat and temperatures generated in some manufacturing processes and tribology. *Tribology International*, 34(10):653–682, 2001.

[257] Philipp Leicht, Lukas Zielke, Samuel Bouvron, Riko Moroni, Elena Voloshina, Lukas Hammerschmidt, Yuriy S. Dedkov, and Mikhail Fonin. In situ fabrication of quasi-free-standing epitaxial graphene nanoflakes on gold. *ACS Nano*, 8(4):3735–3742, 2014.

[258] P. A. Khomyakov, G. Giovannetti, P. C. Rusu, G. Brocks, J. van den Brink, and P. J. Kelly. First-principles study of the interaction and charge transfer between graphene and metals. *Physical Review B*, 79(19):195425, 2009.

[259] J. Sławińska, P. Dabrowski, and I. Zasada. Doping of graphene by a Au(111) substrate: Calculation strategy within the local density approximation and a semiempirical van der waals approach. *Physical Review B*, 83(24):245429, 2011.

[260] Peter W. Sutter, Jan-Ingo Flege, and Eli A. Sutter. Epitaxial graphene on ruthenium. *Nature Materials*, 7(5):406–411, 2008.

[261] D. Subramaniam, F. Libisch, Y. Li, C. Pauly, V. Geringer, R. Reiter, T. Mashoff, M. Liebmann, J. Burgd ́orfer, C. Busse, T. Michely, R. Mazzarello, M. Pratzer, and M. Morgenstern. Wave-function mapping of graphene quantum dots with soft confinement. *Physical Review Letters*, 108(4):046801, 2012.

[262] Paolo Lacovig, Monica Pozzo, Dario Alfè, Paolo Vilmercati, Alessandro Baraldi, and Silvano Lizzit. Growth of dome-shaped carbon nanoislands on Ir(111): The intermediate between carbidic clusters and quasi-free-standing graphene. *Physical Review Letters*, 103(16):166101, 2009.

[263] Brian Kiraly, Erin V. Iski, Andrew J. Mannix, Brandon L. Fisher, Mark C. Hersam, and Nathan P. Guisinger. Solid-source growth and atomic-scale characterization of graphene on Ag(111). *Nature Communications*, 4:2804, 2013.

[264] Jiaming Song, Matthias Bernien, Chii-Bin Wu, and Wolfgang Kuch. Tuning the electronic properties of rotated graphene on Ni(111) by nickel carbide intercalation. *Journal of Physical Chemistry C*, 120(3):1546–1555, 2016.

[265] Hyo Won Kim, Wonhee Ko, JiYeon Ku, Insu Jeon, Donggyu Kim, Hyeokshin Kwon, Youngtek Oh, Seunghwa Ryu, Young Kuk, Sung Woo Hwang, and Hwansoo Suh. Nanoscale control of phonon excitations in graphene. 6:7528, 2015.

[266] J. L. Atwood and J.-M. Lehn. *Comprehensive supramolecular chemistry*. Pergamon, New York, 1996.

[267] Stefan Leininger, Bogdan Olenyuk, and Peter J. Stang. Self-assembly of discrete cyclic nanostructures mediated by transition metals. *Chemical Reviews*, 100(3):853–908, 2000.

[268] Sebastian Stepanow, Nian Lin, Dietmar Payer, Uta Schlickum, Florian Klappenberger, Giorgio Zoppellaro, Mario Ruben, Harald Brune, Johannes V. Barth, and Klaus Kern. Surface-assisted assembly of 2D metalorganic networks that exhibit unusual threefold coordination symmetry. *Angewandte Chemie International Edition*, 46(5):710–713, 2007.

[269] Omar M. Yaghi, Michael O'Keeffe, Nathan W. Ockwig, Hee K. Chae, Mohamed Eddaoudi, and Jaheon Kim. Reticular synthesis and the design of new materials. *Nature*, 423(6941):705–714, 2003.

[270] C. N. R. Rao, Srinivasan Natarajan, and R. Vaidhyanathan. Metal carboxylates with open architectures. *Angewandte Chemie International Edition*, 43(12):1466–1496, 2004.

[271] Susumu Kitagawa, Ryo Kitaura, and Shin-ichiro Noro. Functional porous coordination polymers. *Angewandte Chemie International Edition*, 43(18):2334–2375, 2004.

[272] J.V. Barth, J. Weckesser, N. Lin, A. Dmitriev, and K. Kern. Supramolecular architectures and nanostructures at metal surfaces. *Applied Physics A*, 76(5):645–652, 2003.

[273] Alexandre Dmitriev, Hannes Spillmann, Nian Lin, Johannes V. Barth, and Klaus Kern. Modular assembly of two-dimensional metal-organic coordination networks at a metal surface. *Angewandte Chemie International Edition*, 42(23):2670–2673, 2003.

[274] Hannes Spillmann, Alexandre Dmitriev, Nian Lin, Paolo Messina, Johannes V. Barth, and Klaus Kern. Hierarchical assembly of two-dimensional homochiral nanocavity arrays. *Journal of the American Chemical Society*, 125(35):10725–10728, 2003.

[275] Alexandre Dmitriev, Hannes Spillmann, Magali Lingenfelder, Nian Lin, Johannes V. Barth, and Klaus Kern. Design of extended surface-supported chiral metal-organic arrays comprising mononuclear iron centers. *Langmuir*, 20(12):4799–4801, 2004.

[276] Thomas Classen, Guido Fratesi, Giovanni Costantini, Stefano Fabris, Frank Louis Stadler, Cheolkyu Kim, Stefano de Gironcoli, Stefano Baroni, and Klaus Kern. Templated growth of metal-organic coordination chains at surfaces. *Angewandte Chemie*, 117(38):6298–6301, 2005.

[277] T. Tsuji, H. Takashima, H. Takeuchi, T. Egawa, and S. Konaka. Molecular structure of trans-azoxybenzene determined by gas electron diffraction combined with ab initio calculations. *Journal of Molecular Structure*, 554(2000):203–210, 2000.

[278] Takemasa Tsuji, Hiroyuki Takashima, Hiroshi Takeuchi, Toru Egawa, and Shigehiro Konaka. Molecular structure and torsional potential of trans-azobenzene. a gas electron diffraction study. *The Journal of Physical Chemistry A*, 105(41):9347–9353, 2001.

[279] J. Wachtveitl, S. Spörlein, H. Satzger, B. Fonrobert, C. Renner, R. Behrendt, D. Oesterhelt, L. Moroder, and W Zinth. Ultrafast conformational dynamics in cyclic azobenzene peptides of increased flexibility. *Biophysical Journal*, 86(4):2350–2362, 2004.

[280] Gernot Füchsel, Tillmann Klamroth, Jadranka Dokić, and Peter Saalfrank. On the electronic structure of neutral and ionic azobenzenes and their possible role as surface mounted molecular switches. *Journal of Physical Chemistry B*, 110(33):16337–16345, 2006.

[281] N. Henningsen, K. J. Franke, I. F. Torrente, G. Schulze, B. Priewisch, K. Rück-Braun, J. Dokić, T. Klamroth, P. Saalfrank, and J. I. Pascual. Inducing the rotation of a single phenyl ring with tunneling electrons. *Journal of Physical Chemistry C*, 111(40):14843–14848, 2007.

[282] G. V. Nazin, X. H. Qiu, and W. Ho. Visualization and spectroscopy of a metal-molecule-metal bridge. *Science*, 302(5642):77–81, 2003.

[283] N. Henningsen, R. Rurali, C. Limbach, R. Drost, J. I. Pascual, and K. J. Franke. Site-dependent coordination bonding in self-assembled metal-organic networks. *The Journal of Physical Chemistry Letters*, 2(2):55–61, 2011.

[284] N. Henningsen, R. Rurali, K. J. Franke, I. Fernández-Torrente, and J. I. Pascual. Trans to cis isomerization of an azobenzene derivative on a Cu(100) surface. *Applied Physics A*, 93(2):241, 2008.

[285] M. Corso K. J. Franke R. Haag Ch. Lotze, Y. Luo and J. I. Pascual. Reversible electron-induced cistrans isomerization mediated by intermolecular interactions. *Journal of Physics: Condensed Matter*, 24:394016, 2012.

[286] Paul S. Bagus, Klaus Hermann, and Charles W. Bauschlicher. On the nature of the bonding of lone pair ligands to a transition metal. *The Journal of Chemical Physics*, 81(4):1966–1974, 1984.

[287] Yongwei Wu, Lin Hu, Zhe Li, and Li Deng. Catalytic asymmetric umpolung reactions of imines. *Nature*, 523(7561):445–450, 2015.

[288] Sebastian Stepanow, Nian Lin, and Johannes V Barth. Modular assembly of low-dimensional coordination architectures on metal surfaces. *Journal of Physics: Condensed Matter*, 20(18):184002, 2008.

[289] Johannes V. Barth. Fresh perspectives for surface coordination chemistry. *Surface Science*, 603(1012):1533–1541, 2009. Special Issue of Surface Science dedicated to Prof. Dr. Dr. h.c. mult. Gerhard Ertl, Nobel-Laureate in Chemistry 2007.

[290] U. Schlickum, R. Decker, F. Klappenberger, G. Zoppellaro, S. Klyatskaya, M. Ruben, I. Silanes, A. Arnau, K. Kern, H. Brune, and J. V. Barth. Metal-organic honeycomb nanomeshes with tunable cavity size. *Nano Letters*, 7(12):3813–3817, 2007.

[291] Alexander Langner, Steven L. Tait, Nian Lin, Rajadurai Chandrasekar, Mario Ruben, and Klaus Kern. Ordering and stabilization of metal-organic coordination chains by hierarchical assembly through hydrogen bonding at a surface. *Angewandte Chemie International Edition*, 47(46):8835–8838, 2008.

[292] J.A. Meyer, I.D. Baikie, E. Kopatzki, and R.J. Behm. Preferential island nucleation at the elbows of the Au(111) herringbone reconstruction through place exchange. *Surface Science*, 365(1):L647–L651, 1996.

[293] Bert Voigtländer, Gerhard Meyer, and Nabil M. Amer. Epitaxial growth of thin magnetic cobalt films on Au(111) studied by scanning tunneling microscopy. *Physical Review B*, 44(18):10354–10357, 1991.

[294] Koen Schouteden, Aurélie Lando, Ewald Janssens, Chris Van Haesendonck, and Peter Lievens. Morphology and electron confinement properties of Co clusters deposited on Au(111). *New Journal of Physics*, 10(8):083005, 2008.

[295] Hervé Bulou and Jean-Pierre Bucher. Long range substrate mediated mass transport on metal surfaces induced by adatom clusters. *Physical Review Letters*, 96(7):076102, 2006.

[296] I. Chado, C. Goyhenex, H. Bulou, and J. P. Bucher. Cluster critical size effect during growth on a heterogeneous surface. *Physical Review B*, 69(8):085413, 2004.

[297] M. V. Rastei, J. P. Bucher, P. A. Ignatiev, V. S. Stepanyuk, and P. Bruno. Surface electronic states in Co nanoclusters on Au(111): Scanning tunneling spectroscopy measurements and *ab initio* calculations. *Physical Review B*, 75(4):045436, 2007.

[298] A. G. Trant, T. E. Jones, and C. J. Baddeley. Thermal treatment of glutamic acid-modified nickel nanoclusters on Au111 leads to the formation of one-dimensional metalorganic coordination networks. *Journal of Physical Chemistry C*, 111(28):10534–10540, 2007.

[299] Sylvain Clair, Stéphane Pons, Harald Brune, Klaus Kern, and Johannes V. Barth. Mesoscopic metallosupramolecular texturing by hierarchic assembly. *Angewandte Chemie International Edition*, 44(44):7294–7297, 2005.

[300] J. Kröger, H. Jensen, R. Berndt, R. Rurali, and N. Lorente. Molecular orbital shift of perylenetetracarboxylic-dianhydride on gold. *Chemical Physics Letters*, 438(4):249–253, 2007.

[301] Nora Gonzalez-Lakunza, Marta E. Cañas Ventura, Pascal Ruffieux, Ralph Rieger, Klaus Müllen, Roman Fasel, and Andrés Arnau. Hydrogen-bonding fingerprints in electronic states of two-dimensional supramolecular assemblies. *ChemPhysChem*, 10(17):2943–2946, 2009.

[302] Sebastian Stepanow, Nian Lin, Johannes V. Barth, and Klaus Kern. Surface-template assembly of two-dimensional metal-organic coordination networks. *Journal of Physical Chemistry B*, 110(46):23472–23477, 2006.

[303] U. Schlickum, F. Klappenberger, R. Decker, G. Zoppellaro, S. Klyatskaya, M. Ruben, K. Kern, H. Brune, and J. V. Barth. Surface-confined metal-organic nanostructures from Co-directed assembly of linear terphenyl-dicarbonitrile linkers on Ag(111). *Journal of Physical Chemistry C*, 114(37):15602–15606, 2010.

[304] Christopher S. Kley, Jan Čechal, Takashi Kumagai, Frank Schramm, Mario Ruben, Sebastian Stepanow, and Klaus Kern. Highly adaptable two-dimensional metal-organic coordination networks on metal surfaces. *Journal of the American Chemical Society*, 134(14):6072–6075, 2012.

[305] Satu T. Korhonen, Monica Calatayud, and A. Outi I. Krause. Structure and stability of formates and carbonates on monoclinic zirconia: A combined study by density functional theory and infrared spectroscopy. *Journal of Physical Chemistry C*, 112(41):16096–16102, 2008.

[306] Kwang-Deog Jung and Alexis T. Bell. Role of hydrogen spillover in methanol synthesis over Cu/ZrO2. *Journal of Catalysis*, 193(2):207–223, 2000.

[307] Daniel Bianchi, Tarik Chafik, Mohamed Khalfallah, and Stanislas Jean Teichner. Intermediate species on zirconia supported methanol aerogel catalysts. *Applied Catalysis A: General*, 105(2):223–249, 1993.

[308] Konstantin Pokrovski, Kyeong Taek Jung, and Alexis T. Bell. Investigation of CO and CO2 adsorption on tetragonal and monoclinic zirconia. *Langmuir*, 17(14):4297–4303, 2001.

[309] Yan-Feng Zhang, Na Zhu, and T. Komeda. Mn-coordinated stillbenedicarboxylic ligand supramolecule regulated by the herringbone reconstruction of Au(111). *Journal of Physical Chemistry C*, 111(45):16946–16950, 2007.

[310] Magalí A. Lingenfelder, Hannes Spillmann, Alexandre Dmitriev, Sebastian Stepanow, Nian Lin, Johannes V. Barth, and Klaus Kern. Towards surface-supported supramolecular architectures: Tailored coordination assembly of 1,4-benzenedicarboxylate and fe on Cu(100). *Chemistry A European Journal*, 10(8):1913–1919, 2004.

[311] F. Albert Cotton, Chun Lin, and Carlos A. Murillo. Supramolecular arrays based on dimetal building units. *Accounts of Chemical Research*, 34(10):759–771, 2001.

[312] Alexander Langner, Steven L. Tait, Nian Lin, Rajadurai Chandrasekar, Velimir Meded, Karin Fink, Mario Ruben, and Klaus Kern. Selective coordination bonding in metallo-supramolecular systems on surfaces. *Angewandte Chemie International Edition*, 51(18):4327–4331, 2012.

[313] Xiaoju Li, Tena Guan, Xiaofang Guo, Xinxiong Li, and Zhenjiang Yu. Construction of metal–organic frameworks consisting of dinuclear metal units based on 5-hydroxyisophthalate and flexible dipyridyl ligands. *European Journal of Inorganic Chemistry*, 2014(13):2307–2316, 2014.

[314] Chunhua Gong, Junyong Zhang, Xianghua Zeng, and Jingli Xie. Highly effective synthesis of a cobalt(ii) metal-organic coordination polymer by using continuous flow chemistry. *Dalton Transactions*, 2017.

[315] Yu-Ling Wang, Na Zhang, Qing-Yan Liu, Xin Yang, Hong Bai, Lin-Yan Duan, and Hong-Yu Liu. Ionothermal syntheses and crystal structures of two cobalt(ii)-carboxylate compounds with different topology. *Inorganic Chemistry Communications*, 14(2):380–383, 2011.

Acknowledgments

When I begin to write this part, all sorts of feelings come to my mind. Thinking of so many people I would like to show my gratitude, I have no clue whom to start with.

First of all, I would like to express my appreciation to my supervisor Prof. Dr. Katharina J. Franke. As an old saying in China, "Those who wanted to learn would seek out a teacher, one who could propagate the doctrine, impart professional knowledge and resolve doubts". She sets a good example for me to understand this sentence. Frankly speaking, I am not an intelligent researcher. Fortunately, I have her supervising my PhD studies. She tolerates all my faults and problems with great patience and responsibility. The attitude she guides me to solve the academic problems will be my lifelong benefits.

I also would like to thank Prof. Dr. Petra Tegeder for supervising this thesis as my second referee.

I want to thank Dr. Benjamin W. Heinrich, Dr. Nino Hatter, Dr. Christian Lotze and Dr. Zechao Yang who helped to correct many chapters of my thesis by using their personal time. More thanks to Dr. Christian Lotze for helping to translate the abstract into German.

I am thankful to Dr. Michael Ruby who designed the SpectraFox software to make me analyze data more efficiently.

I feel very grateful to Daniela Rolf and Dr. Nino Hatter for sharing the office as well as the happiness with me for a long time.

I want to say thank you to Dr. Tobias Umbach, Paul Stoll and Dr. Isabel Fernandez-Torrente who patiently guided me when I was a beginner in the STM field.

A lot of thanks to Gelavizh Ahmadi who gave me spiritual encouragement and support same as a foreigner in a foreign country.

I want to thank my Chinese colleagues Dr. Zechao Yang and Dr. Xianwen Chen who I had a great time with in the daily life.

I also want to thank all other present and former members of AG Franke, with whom I worked with during my studies in this group: Wibke Bronsch, Laetitia Farinacci, Marc Font Gual, Dr. Janina Ladenthin, Julia Läger, Eva Liebhaber, Philip Loche, Christian Lotze, Nils Krane, Olof Peters, Dr. Gael Reecht, Andreas Riemann, Sonja Schubert, Rika Simon, Sergey Trishin, and Dr. Jingcheng Li.

Last but not least, I want to express all my gratitude to my parents in-law, my brother and my parents for their financial and spiritual supporting even with a separation of thousands of kilometers.

Special thanks to my wife Wenjia Cai, who spent her best youth in accompanying with me in a foreign country. May time slowly go by, with her hands in mine.

The financial support from the Chinese Scholarship Council (CSC) is gratefully acknowledged.

Contributions to Conferences

2014 Oral Contribution:
Workshop of the SFB 658-Integrated Research Training Group, Lübbenau, Germany 09.10 - 10.10.2014
Investigation of ferrocene-based molecules as precursors for graphene growth on metal substrates

Selbständigkeitserklärung

Ich erkläre, dass ich die vorliegende Arbeit selbständig und nur unter Verwendung der angegebenen Literatur und Hilfsmittel angefertigt habe. Diese Arbeit ist nicht schon einmal in einem früheren promotionsverfahren angenommen oder als ungenügend beurteilt worden.

Own Work Declaration

Hereby I declare to have made this thesis on my own only by use of the denoted literature and resources. Contents taken over from external sources, directly or indirectly, are denoted as such. This dissertation has not been accepted or rejected as insufficient within the context of previous doctoral studies.

Berlin, 30. August 2017